CYPRUS UNIVERSITY OF TECHNOLOGY

FACULTY OF ENGINEERING AND TECHNOLOGY

Master of Science

SURFACE PROCESSING OF SILICON-BASED MATERIALS: SILICON, SILICON OXIDE AND PDMS

Sergey Pozov

Lemesos 2016

SURFACE PROCESSING OF SILICON-BASED MATERIALS: SILICON, SILICON OXIDE, AND PDMS

Presented by

Sergey Pozov

B.Sc., Cyprus University of Technology (2014)

Submitted to the Department of Mechanical Engineering and Materials Science and Engineering in partial fulfillment of the requirements for the degree

Master of Science

at the

CYPRUS UNIVERSITY OF TECHNOLOGY

Supervisor _____

Georgios Constantinides, Assistant Professor

Committee Member _____

Anastasis V. Georgiades, Associate Professor

Committee Member _____

Panagiotis E. Keivanidis, Assistant Professor

Lemesos 2016

Πνευματικά Δικαιώματα

Η έγκριση της μεταπτυχιακής διατριβής από το Τμήμα Μηχανολόγων Μηχανικών και Επιστήμης και Μηχανικής Υλικών του Τεχνολογικού Πανεπιστημίου Κύπρου δεν υποδηλώνει απαραιτήτως και αποδοχή των απόψεων του συγγραφέα εκ μέρους του Τμήματος.

Intellectual Rights

The acceptance of the thesis by the Department of Mechanical Engineering and Materials Science and Engineering of Cyprus University of Technology does not necessarily constitute acceptance of the authors' opinions by the Department.

To my grandfather Sergey Theofanovic Pozov

You will always be in my heart!

Acknowledgements

The completion of this thesis would not have been possible without the help and influence of people around me, to whom I would like to express my sincere gratitude.

First and foremost, I would like to express my deep and sincere gratitude to my supervisor Assistant Professor Georgios Constantinides for his invaluable support, guidance, advices and counselling during my Masters candidature. Moreover I would like the thank him for giving me the opportunity to be a part of the Research Unit for Nanostructured Materials Systems experience which revealed a dream for becoming one of the best researchers.

Furthermore I would like to express my respect to Dr. Loukas Koutsokeras for introducing me to materials science knowledge and research ideas. Many thanks also to PhD candidates Petros Nikolaou for introducing me to characterization techniques (XRR, XRD, UV/VIS) and synthesis (HDS), Marios Constantinou for invaluable knowledge of topographical characterization (AFM) and Demetris Photiou for data analysis techniques. Generally the collaboration with the abovementioned researchers was always useful, and I would like to thank them for making it a pleasure to come into the office and lab each morning. The Research Unit for Nanostructured Materials Systems coordinated by Professor Pantelis Kelires, is also acknowledged.

With deep emotions I would like to thank my family for their patience and understanding. Special thanks and love I express to my parents Elektra V Tchahova and Manolis S Pozov who believed in me from the first time, providing me with financial and spiritual support and making my dreams true. I also want to thank my grandfather Sergey T Pozov for his advices, help and motivation.

Last but not least, I would like to thank Cyprus University of Technology and the Department of Mechanical Engineering and Materials Science and Engineering for the two given scholarships which provided me with financial support during my studies.

ABSTRACT

Recent advances in nanotechnology have generated new forefronts in materials science and engineering. Surface modification at micro- and nano-scale leads to a wide range of surface characteristics such as roughness, hydrophobicity/hydrophilicity, surface charge/energy, biocompatibility and reactivity. Motivated by the wide range of applications, this work investigates two of the main processes for nanoscale surface modification: *Thermal Oxidation* and *Non-Reactive Plasma Processing*. An experimental approach is employed in this thesis where systematic synthesis/processing–structure–properties–performance is undertaken in a controlled manner until structure–property relations are established that will form the scientific basis for surface optimization for specific applications: *surface tailoring*.

In Part A of the thesis, thermal growth of SiO_2 thin films is investigated in order to understand the physics of thermal oxidation of Silicon and the characteristics of the resulting products. SiO_2 thin films were thermally grown and tested for their resulting thicknesses (WLRS), densities (XRR), topography (AFM), and reflectivity (UV/VIS Spectroscopy). It is shown that amorphous-SiO_2 thin films with oxidation rates of ~40 nm/hour are produced. The experimentally obtained thicknesses showed excellent correlation with theoretical predictions calculated by the Deal–Grove model. The color of the grown surfaces depends on the thickness of the layer, which through a color map gives quick optical access to film thickness.

In Part B of the thesis, the effects of a non-reactive inductively coupled plasma (ICP) processing (Argon Ion Bombardment) on Si, SiO_2 and PDMS are studied. The physical, topographical, optical and wetting characteristics of the processed surfaces revealed that in the case of hard materials, uniform and high quality etching rates of 0.1–1.5 nm/min were achieved. On the contrary, PDMS plasma exposure led to impressive surface wrinkles that can be attributed to a stiff layer generation that tends to buckle with specific wavelengths that strongly depend on ion energy and specific amplitudes that depend on both ion energy and fluence. Additionally, wetting characteristics of plasma exposed PDMS surfaces showed a significant reduction in CA linked to the removal of methyl groups from the exposed surface and increase of polar functionalities. However, the hydrophobic nature was recovered in time, due to the migration of low molecular weight polar groups from the surface to the bulk of the material. The transmittance spectra of the PDMS surfaces remained almost unchanged whereas there was a reduction on normal reflectance attributed to an increase in diffusive scattering caused by surface patterning.

ΠΕΡΙΛΗΨΗ

Οι πρόσφατες εξελίξεις στον τομέα της νανοτεχνολογίας διανοίγουν νέους ορίζοντες στην επιστήμη και μηχανική των υλικών. Η επεξεργασία επιφανειών στη μίκρο- και νάνο-κλίμακα οδηγεί σε ένα ευρύ φάσμα επιφανειακών χαρακτηριστικών όπως υδροφοβικότητα/ υδροφιλικότητα, επιφανειακό φορτίο, επιφανειακή ενέργεια και βιοσυμβατότητα. Η παρούσα εργασία, εξετάζει δυο από τις κύριες διεργασίες τροποποίησης επιφανειών στη νανοκλίμακα: *Θερμική Οξείδωση* και *Επεξεργασία Πλάσματος*. Η μεθοδολογία που ακολουθείται είναι πρωτίστως πειραματική όπου διενεργείται συστηματική μελέτη της επεξεργασίας–δομής–ιδιοτήτων–απόδοσης για κατανόηση των μεταξύ τους σχέσεων οι οποίες αποτελούν την επιστημονική βάση για βελτιστοποίηση των επιφανειακών χαρακτηριστικών των υλικών, αναλόγως εφαρμογών.

Στο Μέρος Α της διατριβής, λεπτά υμένια SiO_2 αναπτύχθηκαν μέσω θερμικής επεξεργασίας και μελετήθηκαν προκειμένου να κατανοηθεί η φυσική της θερμικής οξείδωσης του Si και τα χαρακτηριστικά των προκύπτουσων προϊόντων. Συγκεκριμένα μελετήθηκαν τα χαρακτηριστικά πάχους (WLRS), πυκνότητας (XRR), τοπογραφίας (AFM), και ανακλαστικότητας (UV/VIS Spectroscopy) των προαναφερόμενων υμενίων. Προκύπτει ότι, κατά τη θερμική οξείδωση παράγονται άμορφα υμένια SiO_2 με ρυθμούς ανάπτυξης ~40nm/hr. Τα πειραματικά πάχη δεικνύουν πολύ καλή συσχέτιση με τις θεωρητικές προβλέψεις του μοντέλου Deal–Grove. Τα επιφανειακά χρώματα παρουσιάζουν άμεση συσχέτιση με το πάχος των υμενίων και η προτεινόμενη χαρτογράφηση μπορεί να χρησιμοποιηθεί ως μια ταχεία μέθοδος οπτικής εκτίμησης του εύρους της οξείδωσης.

Στο Μέρος Β της διατριβής, μελετήθηκαν οι επιπτώσεις ενός επαγωγικά συζευγμένου πλάσματος που αποσκοπεί στο βομβαρδισμό των επιφανειών Si, SiO_2 και PDMS με ιόντα αργού. Τα φυσικά, τοπογραφικά, οπτικά και υδροφοβικά χαρακτηριστικά των επεξεργασμένων επιφανειών καταδεικνύουν ότι στην περίπτωση των σκληρών υλικών επιτυγχάνεται μια ομοιόμορφη και υψηλής ποιότητας εγχάραξη με ρυθμό 0.1–1.5 nm/min. Αντιθέτως, η έκθεση ενός μαλακού υλικού (PDMS) σε πλάσμα οδηγεί στη δημιουργία επιφανειακών μοτίβων με πτυχώσεις («ζαρώματα») που αποδίδεται στη δημιουργία ενός δύσκαμπτου στρώματος το οποίο τείνει να λυγίσει την επιφάνεια με συγκεκριμένα μήκη και πλάτη κύματος που εξαρτώνται από την κινητική ενέργεια και τη ροή των ιόντων. Τα χαρακτηριστικά διαβροχής των επιφανειών παρουσιάζουν σημαντική μείωση λόγω της απομάκρυνσης των ομάδων μεθυλίου από την εκτεθειμένη επιφάνεια. Ωστόσο, η υδρόφοβη φύση ανακτάται στο χρόνο λόγω της σταδιακής διάχυσης των πολικών ομάδων χαμηλού μοριακού βάρους από την επιφάνεια προς το εσωτερικό. Η οπτική διαπερατότητα των επιφανειών παραμένει σχεδόν αμετάβλητη, ενώ προκύπτει μείωση στην ανακλαστικότητα των υμενίων λόγω της αύξησης της διάχυτής σκέδασης που προκαλείται από την τραχιά επιφάνεια.

CONTENTS

LIST OF TABLES

LIST OF FIGURES

ABBREVIATIONS

PART A

AFM	Atomic Force Microscopy
Ar	Argon gas
a-SiO_2	Amorphous Silicon Dioxide, Fused Silica
B	Parabolic rate constant
B/A	Linear Rate constant
CA	Contact Angle
CH_4	Methane gas
C_i	Concentration of the oxygen at i stage
c-SiO_2	Crystal Silicon Dioxide, Quartz
CUT	Cyprus University of Technology
CVD	Chemical Vapor Deposition
D-G	Deal – Grove
D_i	Diffusivity of the oxygen at i stage
eV	Electron Volts, Energy Units
H	Henry's constant
H_2O	Water chemical compound
I_d	Dark light intensity, room light sources
I_r	Reflectance intensity
I_s	Light source intensity
J_i	Flux of the oxygen at i stage
k	Boltzmann constant
k_s	Rate constant of reaction

MEMS	Micro – Electro – Mechanical – Systems
n	Refractive index
N_1	Number of molecules of oxygen per unit volume
N_2	Nitrogen gas
P_g	Partial pressure
R	Reflectivity
RUNMS	Research Unit for Nanostructured Materials Systems
sccm	Standard cubic centimeters per minute
Si	Silicon
SiO_2	Silicon Dioxide, Silica
T	Temperature
t	Time
TCVD	Thermal Chemical Vapor Deposition
TG	Thermal Growth
x_o or x_i	Initial oxide thickness
x_{ox}	Grown oxide thickness
UV/VIS	Ultraviolet – Visible
XRR	X-ray Reflectivity
τ	Time correction parameter, arise from D-G model

Greek Symbols

Δ_i	Optical path difference
θ_i	Light incident angle
φ	Phase shift
λ	Light Wavelength
π	Pi

PART B

A	Wrinkles' Amplitude
AIB	Argon Ion Bombardment
C	Carbon
DC	Direct Current
E_f	Elastic Modulus of stiff film
E_s	Elastic Modulus of substrate
FFT	Fast Fourier Transformation
HDS	Hybrid Deposition System
h_f	Stiff film's thickness
ICP	Inductively coupled plasma
PDMS	Poly-dimethyl-siloxane
RF	Radio Frequency
RIE	Reactive Ion Etching
rms	Root mean square (roughness)
T	Transmittance
TIS	Total Integrated Scatter
XPS	X-ray Photoelectron Spectroscopy

Greek symbols

λ	Wrinkles' wavelength
ε	Applied strain
ε_c	Critical strain

CHAPTER 1 INTRODUCTORY REMARKS

1.1 Research Motivation

In recent years nanotechnology has developed into one of the most prominent and exciting forefront fields in Physics, Chemistry, Engineering and Biology. Nanoparticles and nanostructures fabricated with the use of nanotechnology present new properties and characteristics that can be utilized in a wide variety of applications. Moreover, the development of nanotechnology introduced new scientific disciplines such as Nanomechanics, Nanofabrication, Nanoengineering, Nanofluidics, Nanoscale Surface Modification and many more.

Motivated by the wide range of applications and the recent establishment of the Research Unit for Nanostructured Materials Systems at Cyprus University of Technology, this work investigates two of the main processes of nanoscale surface modification. The thin film synthesis and characterization of silicon dioxide through *Thermal Oxidation*, and surface processing of hard and soft silicon based materials through *Non-Reactive Plasma Processing.*

1.2 Research Objectives

The objectives of this research are:

- Study the kinetics of thermal oxidation on silicon and subsequent effects on its surface characteristics
- Study the effect of plasma processing on Silicon, Silicon Dioxide and PDMS surface and its subsequent effect on their characteristics

While the two processes might appear to be disparate, they form an integral part of the synthesis and processing activities of the Research Unit for Nanostructured Materials Systems that has been established in 2010 and equipped with a series of cutting-edge synthesis and characterization tools in 2015. The intention of this thesis is, therefore, to calibrate, benchmark and exploit two of the main synthesis/processing equipment that have been recently installed at the Unit and exploit them towards the development of functional surfaces and thin films.

1.3 Research Methodology

An experimental approach is employed in this thesis where systematic synthesis/processing–structure–properties–performance is undertaken in a controlled manner until structure–property relations are established that will form the scientific basis for material and surface optimization for a variety of applications. To this end the Flemings tetrahedron (see Figure 1-1) will form the backbone on our research planning and implementation.

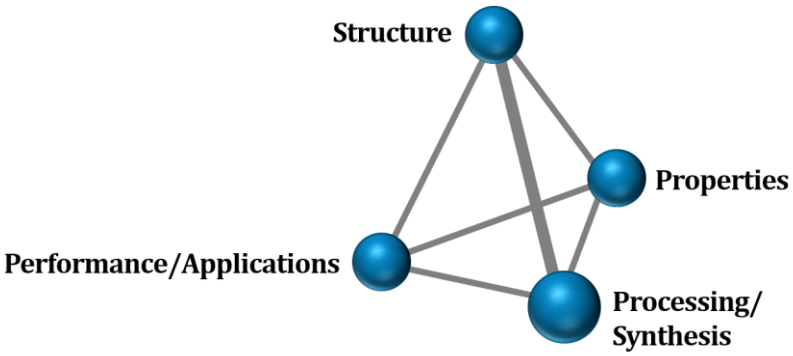

Figure 1-1: Fleming's tetrahedron

1.4 Thesis Outline

This thesis is organized in 2 parts and 9 chapters. The scope, methodology and originality of this study are presented in Chapter 1. Part A is devoted to the surface treatment of silicon and production of thin film silicon dioxide through thermal oxidation. Chapter 2 reviews the general characteristics of silicon and silicon oxides as well as their importance in various applications. In order to introduce the reader to the basic physical mechanisms that take place during thermal oxidation, the theoretical foundations of this process are presented in Chapter 3. Chapter 4 describes the experimental methodology employed in this study, ranging from material processing/synthesis to characterization techniques. Finally Chapter 5 discusses the results on the synthesis and characterization of thermal silicon oxides in relation to theory and already existing data. Part B is devoted to the plasma processing of hard and soft surfaces. Chapter 6 introduces the new components added in this part of the thesis, which are the polydimethylsiloxane material and the plasma processing methodology. The exact material, processing and characterization tools used in this particular experimental study are outlined in Chapter 7, whereas the results and discussion are presented in Chapter 8. A summary of the main findings as well as ideas for future work and perspectives are the content of the final chapter of this thesis, Chapter 9.

PART A: SURFACE OXIDATION OF SILICON

CHAPTER 2 SILICON AND SILICON DIOXIDE

2.1 Chapter Outline

This chapter provides an introduction to the material system under investigation in this part of the thesis: silicon and silicon oxides. The major physical, chemical, structural, thermal, optical and mechanical characteristics of silicon and silicon dioxides are presented together with their methods of synthesis and most notable industrial applications.

2.2 Characteristics

Silicon (Si) is a metalloid with atomic number 14, discovered by Berzelius in 1823 and thereby established as the second most abundant element in the Earth's crust after oxygen (Kilby 1976). Si is solid at room temperature and in its crystalline form has a gray color and a metallic luster as shown in Figure 2-1. It has a relatively high melting and boiling point of 1,414^{o}C and 3,265^{o}C respectively, (Haynes 2014). Moreover, Si has a relatively high thermal conductivity of 149 W/m-K (Slack et al. 1961).

Figure 2-1: Silicon in its crystalline form with different crystal orientations, image adopted from (Wikipedia 2016b).

Owing to its diamond cubic structure (see Figure 2-2), Si is a strong and very brittle material with Young's Modulus of 130–188 GPa and Poisson's ratio of 0.064 – 0.28 (Hopcroft et al. 2010). In its purest form, silicon is a semiconductor material demonstrating a band gap of 1.12eV (Streetman 2000), property which led to a wide variety of important microelectronic applications that will be discussed later in this chapter.

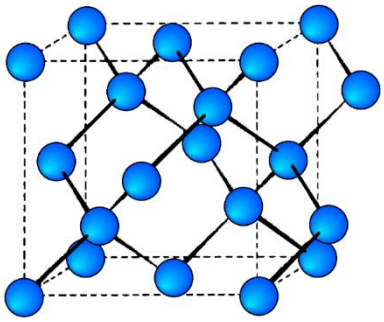

Figure 2-2: Diamond cubic crystal structure of silicon, image adopted from (Archive.cnx.org 2016).

The supplement of 14 electrons in electronic shells has as a result 4 electrons available for bonding with other elements. Thus one of the most known compounds of silicon and oxygen is Silicon Dioxide (SiO_2). Silicon dioxide or silica is one of the most complex families of materials, since it can be presented with up to 16 different crystal structures, or in amorphous form or as silica gel and aerogel, showing different properties in each case. The most famous forms of silica is quartz as crystalline and fused silica as amorphous structures (see Figure 2-3). Since this work deals with thermally grown silicon oxides which according to *Campbell's book* have amorphous structure, only the properties of amorphous silicon dioxide (α-SiO_2) will be presented in this section.

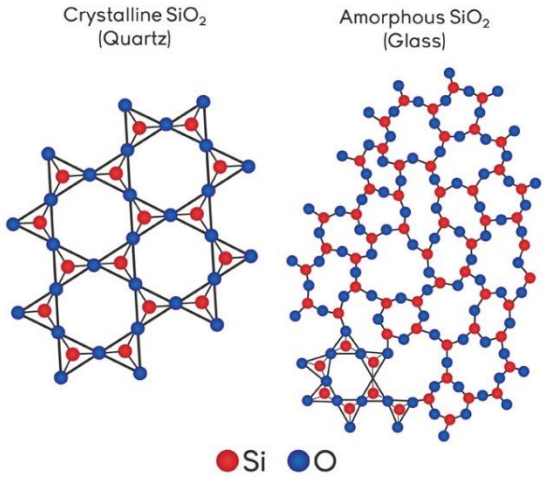

Figure 2-3: Quartz (c-SiO2) and fused silica (α-SiO2) structures. Images adopted from (Learner.org 2016).

α-SiO_2 is solid at room temperature with transparent optical properties that give a refractive index of 1.457 at 632.8nm (Filmetrics 2015). The melting and boiling temperature of fused silica are 1,713^{o}C and 2,950^{o}C respectively, and the thermal conductivity is only 1.4 W/m-K (Haynes 2014). The density of fused silica is 2.20 g/cm^3 (Accuratus.com 2016) and due to its

amorphous structure (see Figure 2-3) it has a Young's Modulus of 73 GPa and a Poisson's ratio of 0.17. Additionally, fused silica has a high electrical resistivity of 10^{14} Ω-m and high band gap energy, that varies from 8–11 eV (Vella et al. 2011). These properties establish fused silica as a very good electrical insulator and lead to important applications especially in electronics. Table 2-1 summarizes and compares the most important properties of Si and thermally grown α-SiO_2.

Table 2-1: Major properties of silicon and amorphous silicon dioxide.

Characteristics	Property	Silicon (Si)	Thermally Grown Amorphous Silicon Dioxide (α-SiO_2)
General	Atomic/Molar weight [g/mol]	28.085	60.08
	Density [g/cm^3]	2.33	2.20
	Crystal structure	diamond cubic	amorphous
Thermal	Melting/Boiling point [^oC]	1,411/2,877	1,713/2,950
	Thermal Conductivity [W/m-K]	149	1.4
Mechanical	Young's Modulus [GPa]	130–188	73
	Poisson ratio	0.064–0.28	0.17
Electrical	Band gap [eV]	1.12 (at 300K)	8–11
	Electrical resistivity [Ω-m]	$2.3x10^3$	1014
Optical	Appearance	gray+metallic luster	transparent
	Refractive index	--------	1.457 (at 632.8nm)

2.3 Production

2.3.1 Silicon Production Techniques

Si rarely occurs in nature in its pure form and thus different methods have been developed to produce pure Si. Some of the most known techniques are discussed in this section.

1. Metallurgical grade method

Metallurgically grade silicon is commercially prepared by reaction of high purity silica with wood, charcoal and coal in an electronic arc furnace as shown in Figure 2-4a. At temperatures over 1,900^{o}C carbon in the aforementioned materials and the silicon undergo the following chemical reaction (Xakalashe & Tangstad 2011):

$$S_iO_2 + 2C \rightarrow Si + 2CO$$

Liquid silicon collects in the bottom of the furnace where it is drained, cooled and then grinded and collected. Silicon produced by this process is called metallurgical grade silicon (Figure 2-4b) and is at least 98% pure. Due to its poor purity, metallurgical grade silicon must be purified with other methods in order to become suitable for high technology applications.

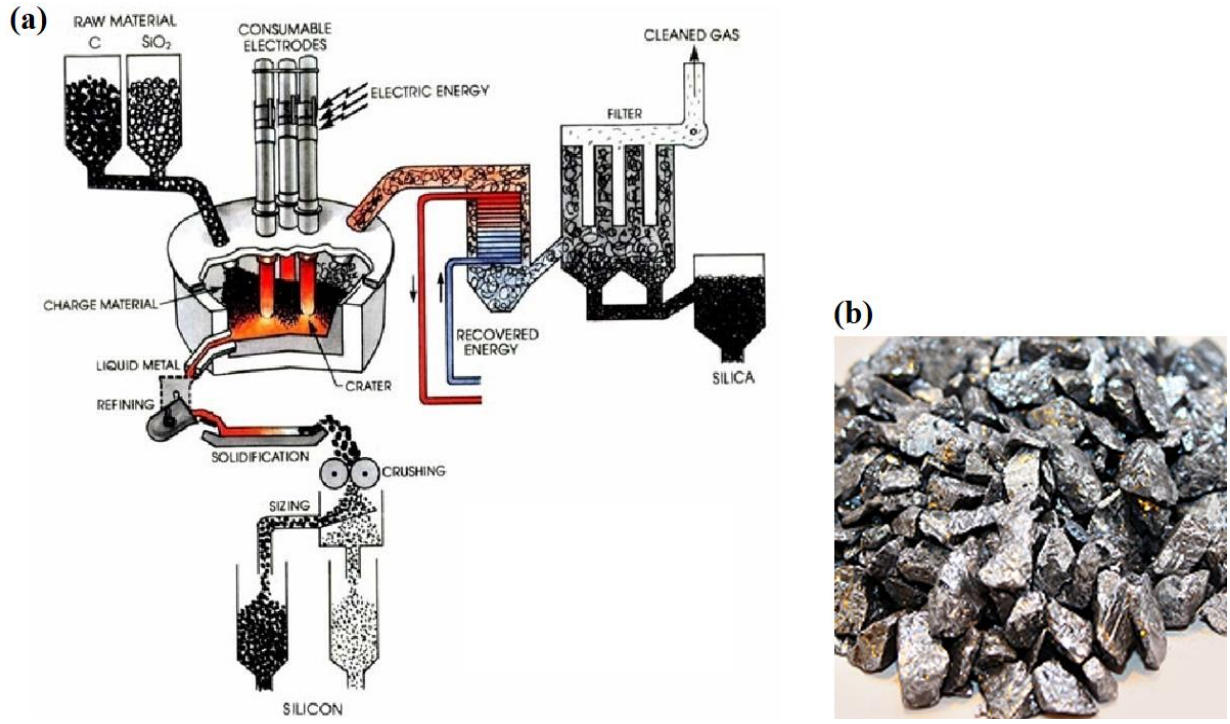

Figure 2-4 : (a) Schematic diagram of metallurgical grade silicon production, (b) metallurgical grade silicon, images adopted from (Xakalashe & Tangstad 2011).

2. Siemens method

Siemens technique grows high purity silicon crystallites directly on the surface of the pre-existing pure silicon rods. The growth of silicon is achieved by chemical decomposition when trichlorosilane gas ($HSiCl_3$) flow over the heated (at 1,150^oC) silicon rods, as shown in Figure 2-5a. The product of this process is polycrystalline silicon (Figure 2-5b) with purity of 9 – 11N, where N='nines' (Braga et al. 2008). Due to its high purity, polycrystalline silicon produced by Siemens method can directly be used by the semiconductor and photovoltaic industries.

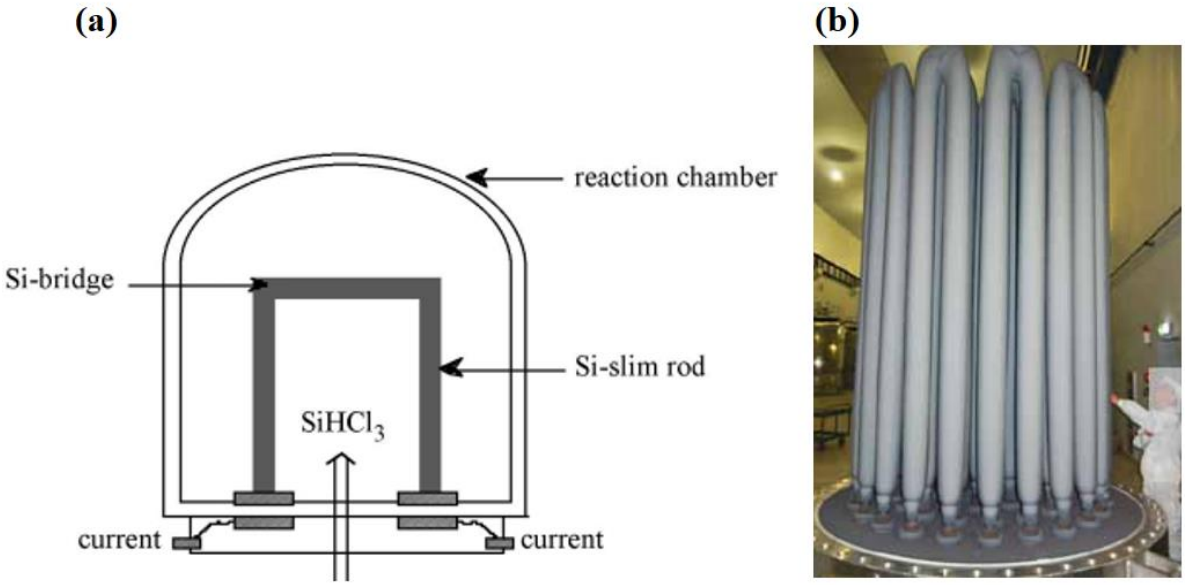

Figure 2-5: (a) Schematic diagram of the Siemens process, (b) Photograph of real silicon rods fabricated by the Siemens process, images adopted from (www.creativeedge.co.uk 2016).

3. Czochralski method

Polish scientist Jan Czochralski in 1916 invented a method of crystal growth used to obtain single crystals of silicon, germanium, gallium and other chemical elements (Saga 2010). Since then, the Czochralski (CZ) technique is considered as the most appropriate methodology for single crystal growth. The technique is schematically presented in Figure 2-6a, where a high–purity silicon is melted in crucible at a specific temperature (around 1,425^oC). Afterwards, a precisely oriented rod (seed crystal) is dipped into the molted silicon and starts to rotate and pull off at specified rates. By precise control of rotation, pull, melting and cooling temperature, single crystal cylindrical ingots (Figure 2-6b) can be produced. Finally, the single crystal silicon ingots are cut into silicon wafers (Figure 2-6c) in order to use in other techniques which will finally lead to specific applications.

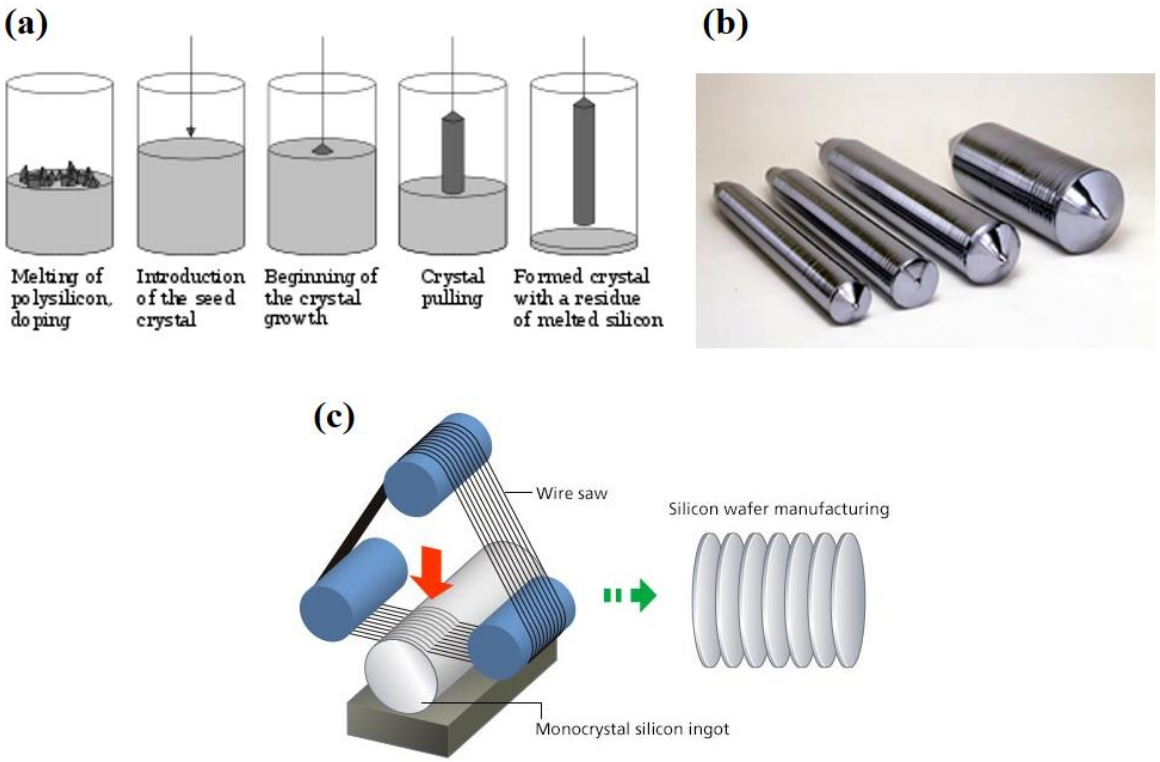

Figure 2-6: (a) Schematic diagram of CZ process, (b) produced silicon ingots, (c) cutting of ingot to obtain silicon wafers, images adopted from (Nikon.com 2016; Wikipedia 2016a).

In this work commercial Si wafers purchased from *Microchemicals* are used for both thermal oxidation and plasma etching processing. These wafers are produced by CZ technique, with thicknesses of 525 ± 25 µm, crystal orientation (100), flat orientation {110} and doping of Phosphorous n-type.

2.3.2 Silicon Dioxide Production Methods

Since this work deals with the production and characterization of silicon dioxide thin films, the general available techniques used to produce this material are presented:

- Pulsed Laser Deposition (PLD)
- Atomic Layer Deposition (ALD)
- Physical Vapor Deposition (PVD)
- Plasma Oxidation (PO)
- Wet Anodization (WA)

- Thermal Growth (TG)
- Chemical Vapor Deposition (CVD)

According to (Campbell 2008) TG and CVD are the most popular growth techniques due to their effectiveness and quality of oxides and are therefore elaborated below.

Chemical Vapor Deposition (CVD)

Generally CVD is a synthesis technique used to produce high–quality, high–performance solid materials. In a typical CVD setup, the substrate is exposed to one or more volatile (tended to vaporize) precursors which react and decompose on the substrate surface producing the desired film. CVD technique is used in a variety of forms classified by operating pressure, physical characteristics of vapor, plasma methods and substrate temperature. The two most known forms are Plasma Enhanced CVD (PE-CVD) and Thermal CVD (T-CVD) systems (see Figure 2-7).

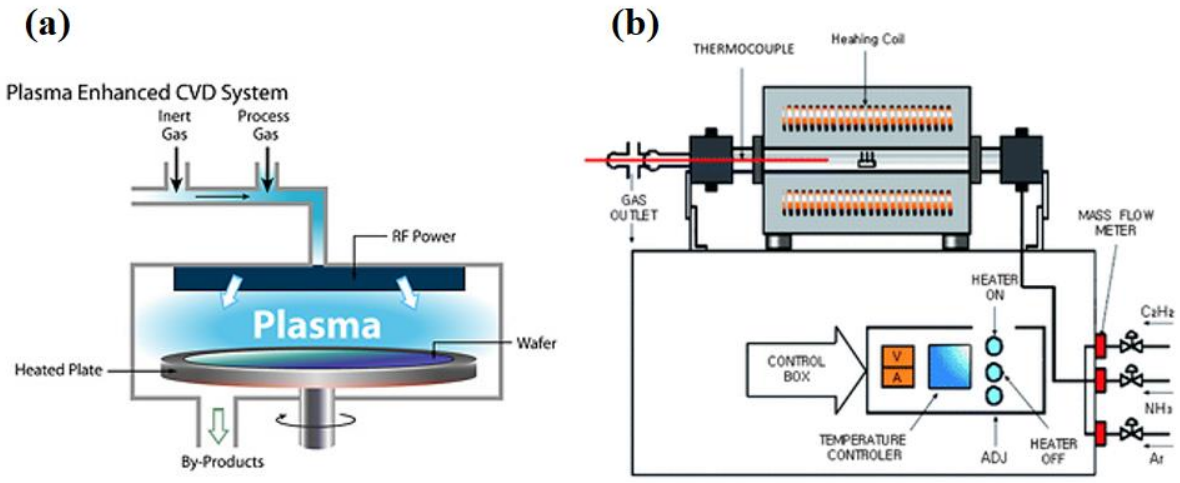

Figure 2-7: (a) Typical Plasma Enhanced CVD system. Image taken from (Dowcorning.com 2016). (b) Typical Thermal CVD system, images adopted from (Nessim 2010).

Microfabrication processes widely use CVD to produce thin films in various forms, including monocrystalline, polycrystalline, amorphous and epitaxial. Therefore, SiO_2 thin films can be produced using specific parameters. John Foggiato in 2012 reported two techniques for SiO_2 thin film production: (a) atmospheric pressure reactors (APCVD) and (b) low pressure and high temperature CVD (T-CVD). In APCVD, silane (SiH_4) and oxygen gas are used under strictly safe conditions. The two gases are injected separately and react spontaneously even at atmospheric conditions. By heating the wafer substrate at 400^{o}C one can achieve a relatively

high deposition rate from 200–300 nm/min (Foggiato 2012). In the second technique, high temperature and a different gas is used. TEOS gas is decomposed due to high temperature, and in the presence of oxygen, high quality SiO_2 films are deposited. In this particular method, growth rates of 100 nm/min can be achieved.

Thermal Growth (TG)

Thermal oxide growth (TG), is one of the most popular technique that has been investigated in depth and can be precisely described by various models. The most well-known model for thermal oxidation is the *Deal–Grove* which describes how exactly the oxide is formed and which parameters must be taken into account in order to achieve the required thickness, (Deal & Grove 1965). TG technique (Figure 2-8) can be divided into dry oxidation, where oxygen gas flows over a silicon wafer under high temperatures, and wet oxidation, where water steam flows over the silicon wafer. Both processes are mainly controlled by the diffusion of oxygen from the gas phase and movement towards the silicon interface in order to react and form new oxides (Campbell 2008). The main difference between dry and wet oxidation is the growth rate which is much higher in the case of wet oxidation. According to *Campbell* this is due to the higher diffusivity and much larger solubility (Henry's constant) for H_2O molecules compared to O_2 molecules.

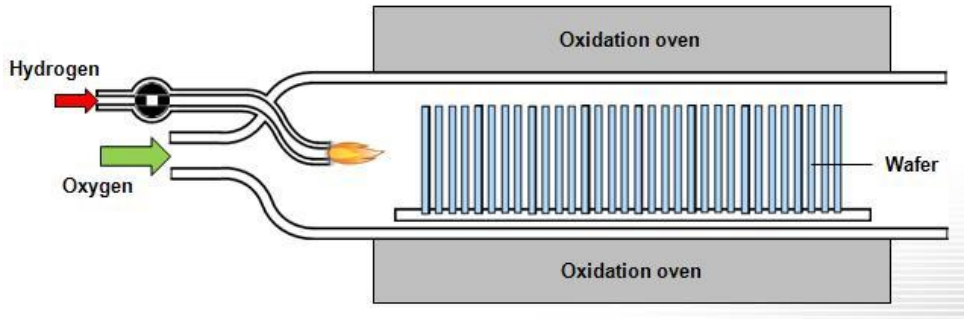

Figure 2-8: Thermal Oxidation: Dry, when only oxygen gas flows, and wet, when both oxygen and hydrogen flows, images adopted from (Powerguru.org 2016).

2.4 Applications

2.4.1 Silicon Applications

Due to its metalloid nature Si has mixed properties of metals and nonmetals, thus it can be used in various applications. For instance Si is the principal component of glass, cement ceramics, the majority of semiconductor devices, and a class of polymeric materials. Figure 2-9 shows four of the most popular applications of silicon. Due to its high Young's Modulus (see Table 2-1), Si can be used as an alloying element in steel industry with the main purpose of increasing the hardness of these materials. Additionally, Si can be used as wafers upon which integrated circuits (transistors, resistors, capacitors and insulators) can be built through doping processes. Moreover, Si represents the main element of siloxanes which lead to polymeric materials. Finally, due to its relatively low band gap (see Table 2-1) Si serves as the major constituent of photovoltaic cells.

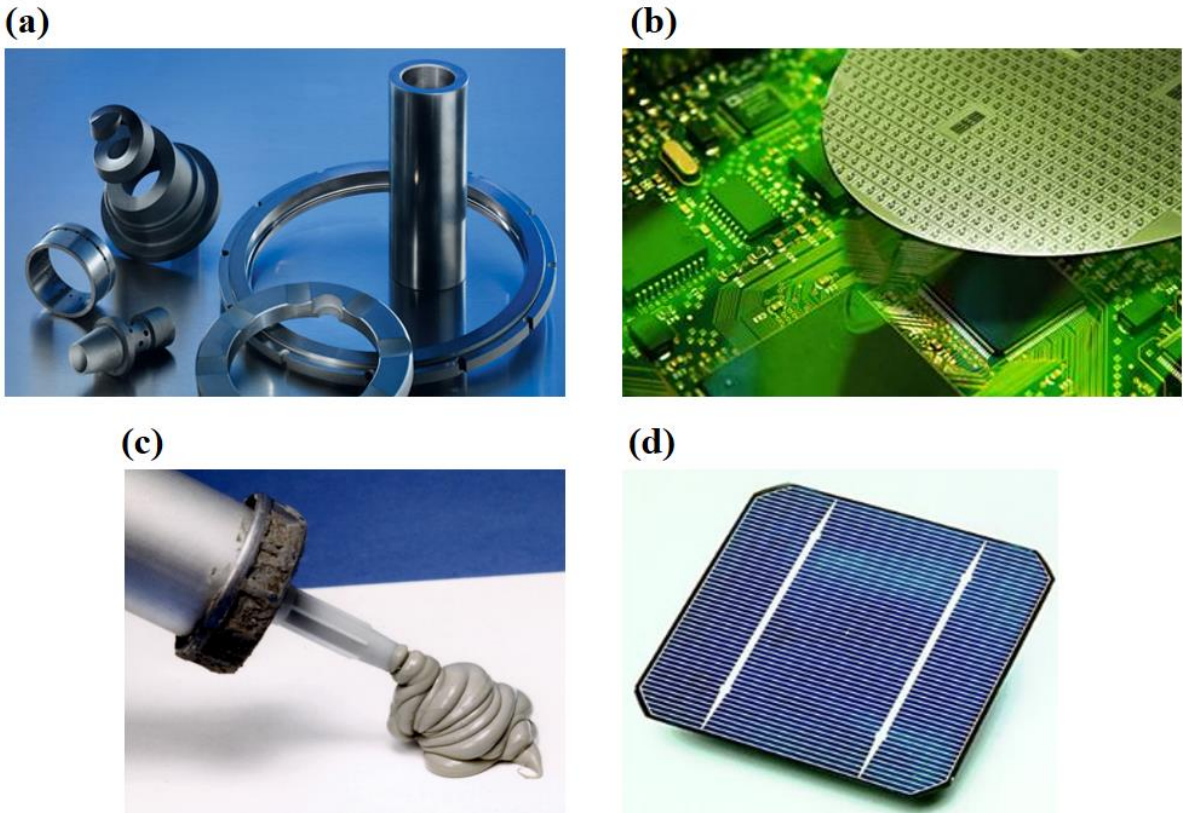

Figure 2-9: Silicon's most popular applications (images adopted from (Google.com.cy 2016)): (a) Si as a combination element in steel industry, (b) Si wafers in Integrated Circuits production, (c) Si principal element of siloxanes that produce silicone and (d) Si as essential material in photovoltaic cells.

2.4.2 Silicon Dioxide (Thin Films) Applications

Silicon dioxide thin films are mostly used in microfabrication processes (Ray et al. 1996). Owing to its inert chemical structure, silicon dioxide thin films can be used as passivation layers, as oxidation barriers/masks and as etching masks in surface modification and micro device production industry (Cadarso et al. 2008). Additionally, due to its high electrical resistivity and low heat conductivity (see Table 2-1), SiO_2 is an essential material in micro-electro-mechanical systems (MEMS) and semiconductor technology, since it can be used as a very good thermal and electrical insulator. Some of silicon's applications are schematically shown in Figure 2-10.

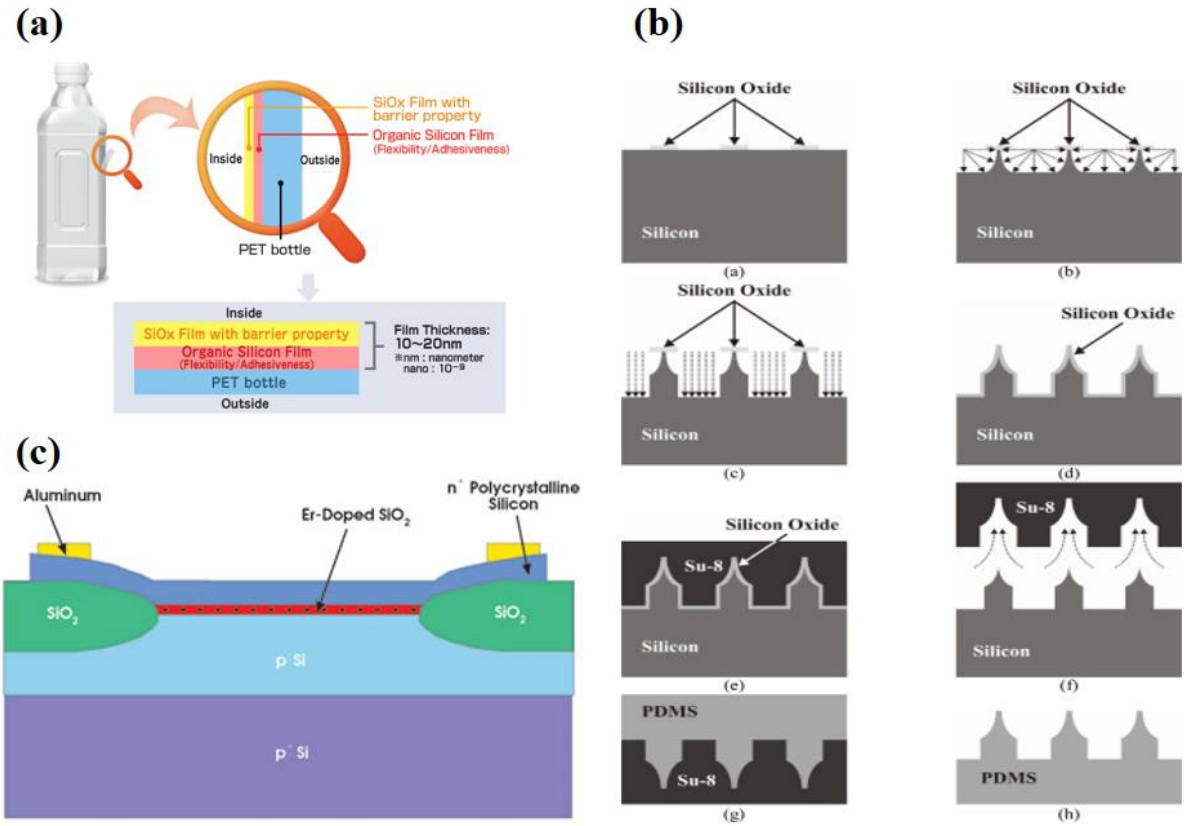

Figure 2-10: SiO_2 thin films popular applications: (a) SiO_2 used as a chemical barrier layer for plastic bottles, image adopted from (Toyo-seikan.co.jp 2016), (b) SiO_2 used as a mask in a multistep patterning process, image adopted from (Cadarso et al. 2008), (c) SiO_2 used as doping barrier and electrical insulator in a microelectronic device, image adopted from (http://www.photonics.com/ at 05.01.16).

2.5 Chapter Summary

The main characteristics of silicon and amorphous silicon dioxide, together with their most popular production methods, are presented in this Chapter. The use of these two materials in micro– and nano–scale fabrication, proved to be essential for a wide variety of applications. This chapter, therefore, lays the foundation for what will follow in the next chapters of this part of the thesis which is focused on the production and characterization of SiO_2 thin films through thermal oxidation of silicon wafers.

CHAPTER 3 THEORY OF SURFACE OXIDATION

3.1 Chapter Outline

In this chapter we introduce the theoretical background on the physical mechanisms involved during thermal oxidation of silicon. Particular emphasis is placed on the Deal-Grove model, which forms the benchmark on modeling results and exhibits excellent agreement with available experimental data.

3.2 Thermal Oxidation Modeling: Deal–Grove Model

Owing to its great importance in planar silicon device technology, the formation of silicon dioxide (SiO_2) layers by thermal oxidation has been studied extensively in the past, producing a great amount of available literature data. This data, together with preliminary modeling attempts to describe the thermal oxidation process, led researchers Bruce Deal and Andy Grove to investigate the thermal oxidation phenomenon in detail. After examining thermal oxidation kinetics and physics, Deal and Grove managed to propose a general relationship in 1965 that describes the thermal oxidation of silicon (Deal & Grove 1965), now commonly referred to as the Deal–Grove model (D–G model in short).

In general, the thermal oxidation is divided in two processes dry and wet oxidation, and both are described with high accuracy by the D–G model:

Dry $$\mathrm{Si(solid) + O_2(gas) \rightarrow SiO_2(solid)}$$

Wet $$\mathrm{Si(solid) + 2H_2O(vapor) \rightarrow SiO_2 + 2H_2(gas)}$$

In this work we will focus on the dry oxidation process.

3.2.1 Theory of Dry Oxidation: Oxide Growth

In general, high temperatures are not necessary to grow an oxide layer on silicon surface; in fact, a native oxide is always present on silicon wafers, with a thickness of approximately 1nm (Kilby 1976).On the other hand if someone wants to form accurate and thicker silicon oxide films, there are various methods available, (see Section 2.3.2). As it was mentioned in Chapter 2 the two most well-known based on their effectiveness and quality of products are the Thermal

Growth (TG) and Chemical Vapor Deposition (CVD) methods. In this work all films were thermally grown using a dry oxidation process, which according to *Campbell* is the method that produces oxides with the fewest defects, both in the bulk and at the interface. Dry thermal oxidation process is generally a simple technique which grows oxides by supplying oxygen gas, at a specific flow rate, that reacts with the silicon wafer at high temperatures. The transported oxygen (in dry oxidation case O or O_2) must go through the following stages:

1) Oxygen diffuses through the gas to the top of the wafer
2) Oxygen diffuses through the continuously growing oxide layer which is on the top of the silicon wafer, to the silicon interface
3) Oxygen reacts with silicon to form silicon oxides

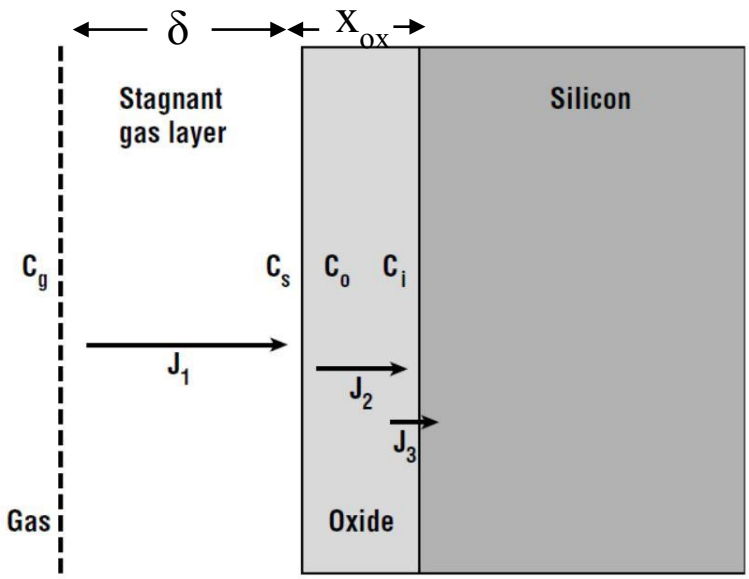

Figure 3-1: Schematic diagram of the oxygen flows during oxidation, images adopted from (Campbell 2008)

3.2.2 Deal–Grove Model

D–G model is the first and most popular model in use, even today, for oxidation process of planar substrates. The model describes precisely the oxidation process and is in very good agreement with available experimental data. The aim of the detailed investigation of the D–G model in this section is twofold:

1) To help us understand the physics of oxide growth

2) To compare and discuss the experimental data that will be acquired from the synthesis of silicon oxide layers with the D-G model.

Step 1: Oxygen diffuses through the gas to the wafer surface

Invoking Fick's first law with linear approximation, owing to the minimal change of concentration across the covered distance (dx=δ) due to its infinitesimal nature, the amount of the reactant species across a unit surface per unit time can be expressed as:

$$J_1 = D \times \frac{dC}{dx} \approx D_{O_2} \times \frac{C_g - C_s}{\delta} \tag{3-1}$$

where J_1 is the flux of the oxygen to the outer surface [moles/cm^2-s], D_{O_2} is the diffusivity of reactant O_2 in gas [cm^2/s], δ is the boundary layer thickness, the distance that reactant O_2 covers in order to diffuse to the wafer surface [μm], C_g is the concentration of oxygen in the gas stream far from the silicon surface [moles/cm^3], and C_s is the concentration of oxygen at the outer surface of the oxide [moles/cm^3].

In order to simplify Eq. (3-1), the gas–phase transport coefficient (h_g=D/δ) is used to create a compact version:

$$J_1 = J_{gas} = h_g(C_g - C_s) \tag{3-2}$$

where h_g has units of [m/s].

Step 2: Oxygen diffuses across the growing oxide layer

Using again the Fick's first law with linear approximation, the flux of oxygen across the oxide layer is expressed through:

$$J_2 = D \times \frac{dC}{dx} \approx D_{O_2} \times \frac{C_o - C_i}{x_{ox}} \tag{3-3}$$

where J_2 is the flux of oxygen through the oxide to the SiO_2–Si interface [moles/cm^2-s], x_{ox} is the grown oxide layer [μm], C_o is the concentration of the oxygen adsorbed in the oxide [moles/cm^3], C_i is the concentration of oxygen at the SiO_2–Si interface [moles/cm^3].

Step 3: Oxygen reacts with Si

Finally, the oxygen species arrive to the SiO_2–Si interface where reaction is expected to occur, creating new SiO_2 bonds in the process. Thus the rate of reaction is determined by chemical reaction kinetics, assuming first order reaction, where the reaction rate and flux of oxygen are proportional to the oxygen concentration:

$$J_3 = k_s C_i \tag{3-4}$$

where J_3 is the flux of oxygen as it reacts with Si [moles/cm^2-s], and k_s is the reaction rate constant [1/s].

Steady State hypothesis

Initially the diffusion of reactant through the gas phase to the surface and then through the oxide layer is faster than the reaction at the interface. But soon after, steady state conditions will be reached; in other words the supply of oxygen will be just enough to be consumed by the reaction. That means all the fluxes of the reactant will be equal. The validity of the steady state approximation is shown in the Appendix of (Deal & Grove 1965) published paper.

$$J_1 = J_2 = J_3 = J_{ss} \tag{3-5}$$

$$J_1 = J_2 \tag{3-6}$$

$$J_2 = J_3 \tag{3-7}$$

Eqs. (3-6) and (3-7) have 4 unknown concentrations (C_g, C_s, C_o, C_i). Hence, more equations are required to solve the problem. The first equation is produced using Henry's law, which gives us the concentration of the reactant that has been adsorbed on the surface with respect to its partial pressure:

$$C_o = HP_g \tag{3-8}$$

where P_g is the partial pressure of the oxygen at the surface [atm], H is Henry's law constant [L-atm/mole], k is the Boltzmann constant [1.38064852×10^{-23} m^2.kg.s^2.K^{-1}], and T is the

absolute temperature [K]. Moreover by introducing the ideal gas law, partial pressure can be expressed as:

$$C_s = \frac{n}{V} = \frac{P_g}{kT} \rightarrow P_g = C_s kT \tag{3-9}$$

and thus the oxygen concentration adsorbed at the surface can be calculated from:

$$C_o = HkTC_s \tag{3-10}$$

Using Eqs. (3-6), (3-7) and (3-10), and after some algebraic calculations we get:

$$J_{ss} = \frac{Hk_s P_g}{1 + \frac{k_s}{h} + \frac{k_s x_{ox}}{D}} \tag{3-11}$$

where $h=h_g/HkT$ is the effective mass transport coefficient.

To obtain the growth rate, one needs to divide the flux at the interface by the number of molecules of oxygen per unit volume N_1 [$N_1=2.2\times10^{22}$ cm^{-3}] of SiO_2 which is commonly half the number density of oxygen atoms in SiO_2.

Eventually the growth rate is expressed by the following differential equation and its initial condition, which defines the oxide thickness at time zero:

$$\frac{dx_{ox}}{dt} = \frac{J_{ss}}{N_1} = \frac{Hk_s P_g}{N_1\left(1 + \frac{k_s}{h} + \frac{k_s x_{ox}}{D}\right)} \qquad x_{ox} = x_i \quad \text{at} \quad t = 0 \tag{3-12}$$

Using straightforward integration of the differential equation, Eq. (3-12), the D–G general equation of thermal oxidation is obtained:

$$\mathbf{x_{ox}^2 + Ax_{ox} = B(t + \tau)} \tag{3-13}$$

$$A = 2D\left(\frac{1}{h} + \frac{1}{k_s}\right) \qquad [\mu m]$$

$$B = \frac{2DHP_g}{N_1} \qquad [\mu m^2/h] \qquad (3\text{-}14)$$

$$\tau = \frac{x_i^2 + Ax_i}{B} \qquad [h]$$

The physical importance of the parameters included in Eq. (3-13) follows:

- A, B: These parameters are well known for a variety of processing conditions. The more fundamental parameters such as diffusivity, reaction rate constant that go into A, B are rarely quoted. Parameters A, B can be found in oxidation tables.
- τ: This parameter arises due to the boundary condition for the differential Eq.(3-12) at zero time. That means if an oxidation begins with an initial oxide thickness t_i the τ value is necessary to be calculated in order to add it to the oxidation time (t) and obtain the total effective oxidation time ($T_{eff} = t + \tau$).

Parameters A, B and τ are very important, and will therefore be discussed in detail in the following section.

3.2.3 Remarks on the Deal–Grove Model

General equation

Solving the quadratic form of Eq. (3-13) yields the oxide thickness as a function of oxidation time:

$$x_{ox} = \frac{-A + \sqrt{A^2 + 4B(t+\tau)}}{2} \;\therefore\; \frac{x_{ox}}{A/2} = \sqrt{\left[1 + \frac{t+\tau}{A^2/4B}\right]} - 1 \qquad [\mu m] \qquad (3\text{-}15)$$

According to (Deal & Grove 1965), Eq. (3-15) has two limiting forms, at relatively large and relatively small times of oxidation. These limiting forms give the well-known *parabolic* and *linear* regimes of the D–G model.

Parabolic Regime
At relatively large oxidation times, i.e. $t \gg A^2/4B$

$$\frac{x_{ox}}{A/2} \cong \sqrt{\frac{t+\tau}{A^2/4B}} \tag{3-16}$$

Under these conditions Eq. (3-15) reduces to the following parabolic equation:

$$x_{ox}^2 \cong B(t+\tau) \qquad [\mu m] \tag{3-17}$$

where B is the parabolic rate constant [μm^2/h] and τ is a time scale constant that corresponds to a shift in the time coordinate and corrects for the presence of the initial oxide layer x_i [h].

Linear regime
At relatively small oxidation times, i.e. $t \ll A^2/4B$

$$\frac{x_{ox}}{A/2} \cong \frac{1}{2}\left(\frac{t+\tau}{A^2/4B}\right) \tag{3-18}$$

Thus Eq. (3-15) reduces to the following linear regime equation:

$$x_{ox} \cong \frac{B}{A}(t+\tau) \qquad [\mu m] \tag{3-19}$$

where B/A is the linear rate constant [μm^2/h].

Figure 3-2 shows the general equation of oxidation, the linear and parabolic approximations together with experimental data from the literature. The solid line represents the general relationship, the dotted lines related to the two limiting forms (linear and parabolic) and the experimental data is represented by points. It is obvious that all the data is in perfect agreement with the general equation of oxidation. Moreover, it can be noted that the experimental data is perfectly fitted by the linear regime for relatively small oxidation times and by the parabolic regime for relatively large times. The axes of Figure 3-2 are dimensionless quantities which are used to plot a combination of different experimental results on the same graph. In order to use the simplified parabolic or linear regime, it is necessary to select the parameters (*A*, *B*, τ and t) which will be used to fabricate the oxides, calculate the x-axis dimensionless quantity,

determine the range and decide which equation will give correct answers. On the other hand we can always use the general equation of oxidation.

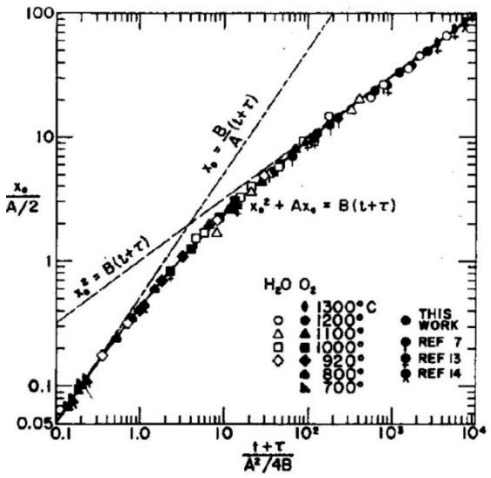

Figure 3-2: General relationship and its two limiting forms for thermal oxidation of silicon with zero initial oxide thickness, graph adopted from (Deal & Grove 1965)

Parameter τ

According to (Deal & Grove 1965), the general model fits perfectly the data for wet oxidation (see Figure 3-2), but for dry oxidation it exhibits a peculiarity. Experimental data for dry oxidation demonstrates a faster growth rate for the first 20 – 30 nm of oxide thickness (Figure 3-3a). In order to further investigate the application of their general equation for dry oxidation, Deal and Grove plotted experimental results on an oxide thickness vs. oxidation time graph, and quantified the initial thickness t_i that the experimental data extrapolated at zero time. The results suggest that the initial thickness at zero time was 23±3 nm (Figure 3-3a).

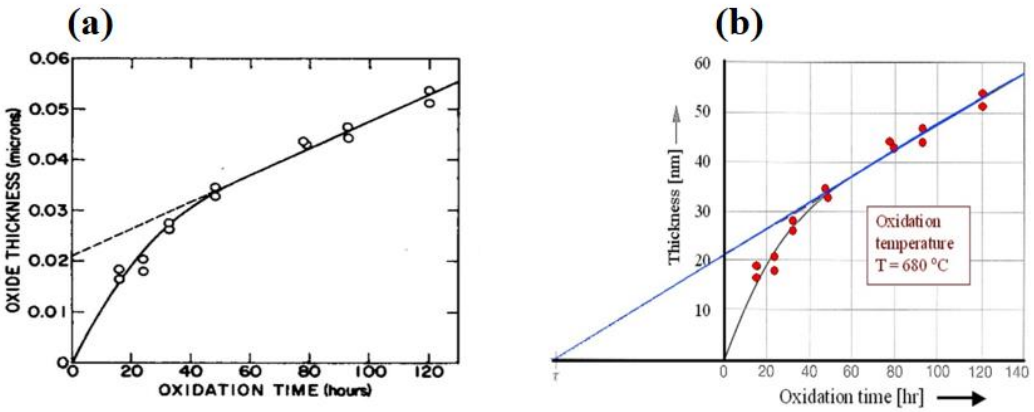

Figure 3-3: (a) Dry oxidation of silicon at 700ºC; graph taken from (Deal & Grove 1965). (b) Tau calculation plot; graph adopted from (Tf.uni-kiel.de 2016).

The explanation of this result suggests two possible mechanisms: the first one is that an oxide film of 23 nm was preexisting on the surface before the oxidation process and the second is that a different mechanism of oxidation applies at thicknesses less than 30 nm. Through an extensive experimental analysis proved that no initial oxide film of 23 nm was present on the silicon wafers (Deal & Grove 1965). Thus, Deal and Grove decided to use a parameter τ to correct the initial growth rate of the oxide. This parameter accounts for the faster initial oxidation rate, reducing the required oxidation time by assuming an initial oxide thickness which in reality is not present (Campbell 2008). The calculation of τ is accomplished by plotting the oxide thickness vs. oxidation time for different temperatures, and fitting the data linearly, an example off which is shown in Figure 3-3b. Extending this line, back through the oxide thickness of 23 nm, an intersection with x-axis appears and gives the τ values which are then summarized in oxidation tables. It is important to mention that the values of τ presented on dry oxidation tables presuppose that in reality there is no initial oxide on the wafers. On the other hand, if an initial oxide layer with specific thickness is present on the wafer, the τ value must be calculated using Eq. (3-14).

It becomes apparent, from the previous analysis of the D–G model that the most important quantities for oxide thickness or oxidation time predictions are parameters *A*, *B*, and τ. It is therefore crucial to understand their dependence with respect to experimentally controllable variables. Hence, this section is dedicated to the investigation of how these parameters are affected by temperature, pressure and crystal orientation of the wafers.

1. Temperature dependence of oxide growth

Parameter *A*

In order to investigate the temperature dependence of parameter *A*, Eq. (3-14) must be recalled. According to that equation, the 1/h quantity can be neglected, as the mass transport coefficient (h), is much higher than the rate constant of reaction, k_s.

$$A = 2D\left(\frac{1}{h} + \frac{1}{k_s}\right) \approx \frac{2D}{\mathbf{k_s}} \tag{3-20}$$

The temperature dependence of parameter *A* comes from the diffusivity (D) and the rate constant of reaction k_s. Both D and k_s dependence on temperature is described by Svante-Arrhenius equations, which show an exponential dependence. But comparing them, the most dependent on temperature parameter is k_s which can be doubled if the temperature increases

by 20°C. Therefore the parameter *A* is strongly dependent on temperature via k_s, and that means the increase of temperature will decrease the parameter *A* and vice versa.

Parabolic rate constant, Parameter *B*

Invoking the parabolic rate constant, Eq. (3-14), its temperature dependence is controlled by the diffusivity (D). That means when the ambient temperature will lead to an activation energy equal to 1.24eV the diffusion of O_2 through the SiO_2 layer will be initialized. The further increase of temperature will lead to higher diffusivity and at the same time to higher parabolic rate constant, as shown in Figure 3-4a.

Based on the same figure it could be defined that the parabolic rate constant is higher for wet oxidation process, due to the higher diffusivity of H_2O molecules than O atoms or O_2 molecules. At relatively large oxidation times when very thick oxide layer is presented, the oxidation process is based on the diffusion stage and not on the reaction stage. That is why, at relatively large oxidation times the parabolic regime prevails.

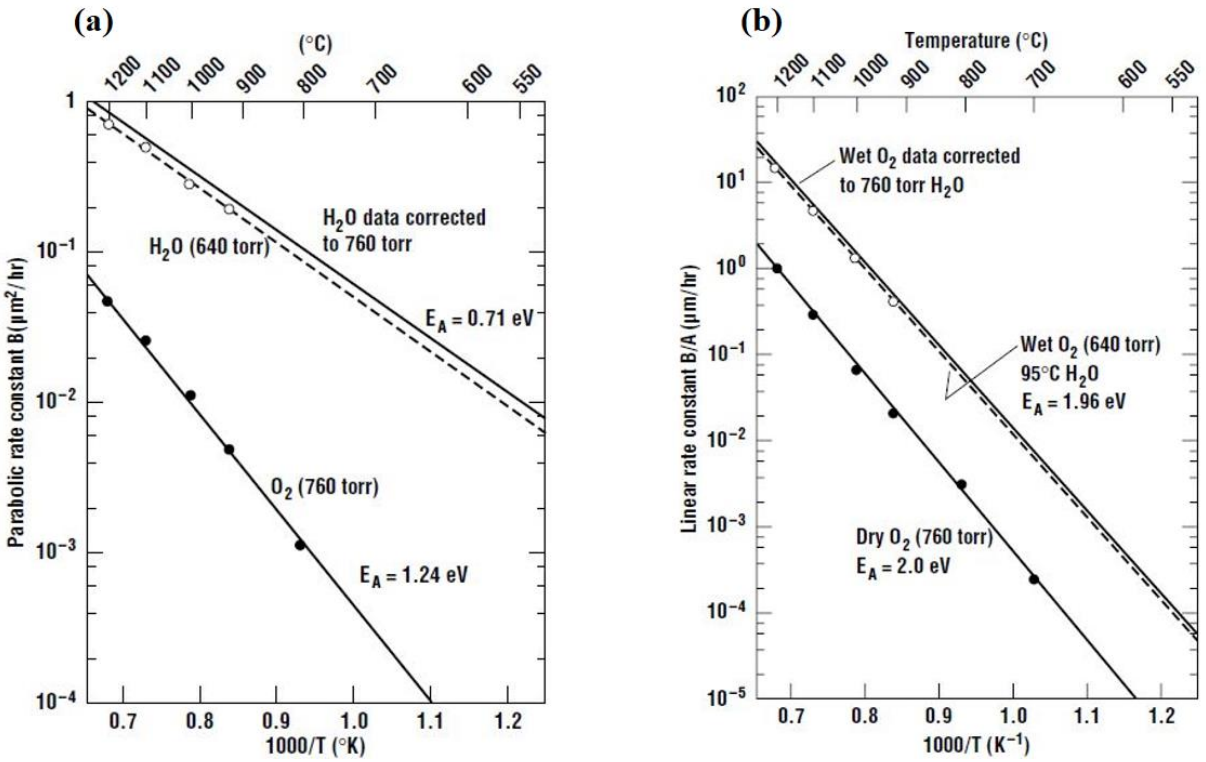

Figure 3-4: Temperature dependence of rate constants, (a) parabolic rate constant and (b) linear rate constant, graphs adopted from (Campbell 2008)

Linear rate constant, Parameter: *B/A*

Using Eq. (3-20) and the parabolic rate constant equation, their deviation will give the linear rate constant, as it shown in Eq. (3-21). According to that equation the temperature dependence of linear rate constant is appeared by the rate constant of reaction (k_s).

$$\frac{B}{A} \approx \frac{\cancel{2D}k_s HP_g}{\cancel{2D}N_1} = \frac{\mathbf{k_s} HP_g}{N_1} \tag{3-21}$$

That means when the ambient temperature will lead to an activation energy equal to 2.0eV the reaction of Si – Si bond breaking and Si – O_2 bond generation will be initialized. The further increase of temperature will lead to higher rate of reaction and at the same time to higher linear rate constant, as it is shown in Figure 3-4b.

At relatively small oxidation times when very thin oxide layer presents, the oxidation process is based on the reaction stage and not on the diffusion. That is why, at relatively small oxidation times the linear regime prevails.

Time offset parameter, τ

Eventually concerning the constant parameter *A*, Eq. (3-18), which is reducing while the temperature increases due to the division with the term k_s and the parameter *B* which is proportional to the temperature due to the diffusivity term, it is obvious that the parameter τ Eq. (3-14) will reduce with the temperature increase for both wet and dry oxidation processes.

$$\tau = \frac{x_i^2 + Ax_i}{B}$$

Tables of rate constants with respect to different temperatures

According to Deal–Grove paper plotting experimental data of oxide thickness (x_{ox}) vs. oxidation time with respect to oxide thickness [$(t+\tau)/x_{ox}$] for different temperatures, the rate constants for dry or wet oxidation can be calculated. These values are usually shown in oxidation tables like Table 3-1.

Table 3-1: Rate constants for oxidation of silicon (111), in dry oxygen. $x_o^2 + Ax_o = B(t+\tau)$, data adopted from (Deal & Grove 1965)

Oxidation Temperature [°C]	A [μm]	B [μm²/h]	B/A [μm/h]	τ [h]
1200	0.040	0.045	1.12	0.027
1100	0.090	0.027	0.30	0.076
1000	0.165	0.0117	0.071	0.37
920	0.235	0.0049	0.0208	1.40

Oxide thickness dependence on temperature

Invoking the general equation of oxidation it can be shown that the parameter A^2 and $A/2$ can be neglected. That means, the oxide thickness is proportional to parabolic rate constant which increases with temperature. Consequently, at high temperature and large oxidation times someone can get thick oxide layers.

$$x_{ox} = \frac{-A + \sqrt{A^2 + 4B(t+\tau)}}{2} \tag{3-22}$$

2. Pressure dependence of oxide growth

Parameter: *A*

According to Eq. (3-20) it is obvious that parameter *A* is independent of pressure:

$$A = 2D\left(\frac{1}{h} + \frac{1}{k_s}\right) \approx \frac{2D}{k_s} \quad \leftrightarrow \quad \mathbf{A \neq f(P_g)} \tag{3-23}$$

Parabolic rate constant *B* and linear rate constant *B/A*

The parabolic rate constant *B* and subsequently the linear rate constant *B/A* are proportional to the partial pressure of the oxygen if Henry's law is obeyed (Deal & Grove 1965):

$$\frac{B}{A} \approx \frac{\cancel{2D}k_s H P_g}{\cancel{2D}N_1} = \frac{k_s H \mathbf{P_g}}{N_1} \quad \leftrightarrow \quad \mathbf{\frac{B}{A} = f(P_g)} \tag{3-24}$$

$$B = \frac{2DH\mathbf{P_g}}{N_1} \qquad \leftrightarrow \quad \mathbf{B = f(P_g)} \tag{3-25}$$

Experimental data shows that for dry oxidation, the parabolic rate constant is proportional to the partial pressure as it shown in Eq. (3-26), but the linear rate constant shows an exponential dependence with the experimental data Eq. (3-27) which is caused by the reactant species of dry oxidation. For the case of atomic oxygen O diffusion the n value is equal to 1.0, and for

molecular oxygen O_2 diffusion the value is equal to 0.5. Thus the exponent *n* is limited between those two values. But according to Uematsu et.al (Silicon 2000), a value of *n = 0.75* can be used for dry oxidation processes:

$$B(P_g) = B_{1atm} \times P_g \tag{3-26}$$

$$\frac{B}{A}(P_g) = \frac{B}{A}(1\ \text{atm}) \times {P_g}^n \quad \therefore \quad n = 0.75 \tag{3-27}$$

Generally both wet and dry oxidation processes show an important increase of the parabolic and linear rate constants with respect to partial pressure, (see Figure 3-5).

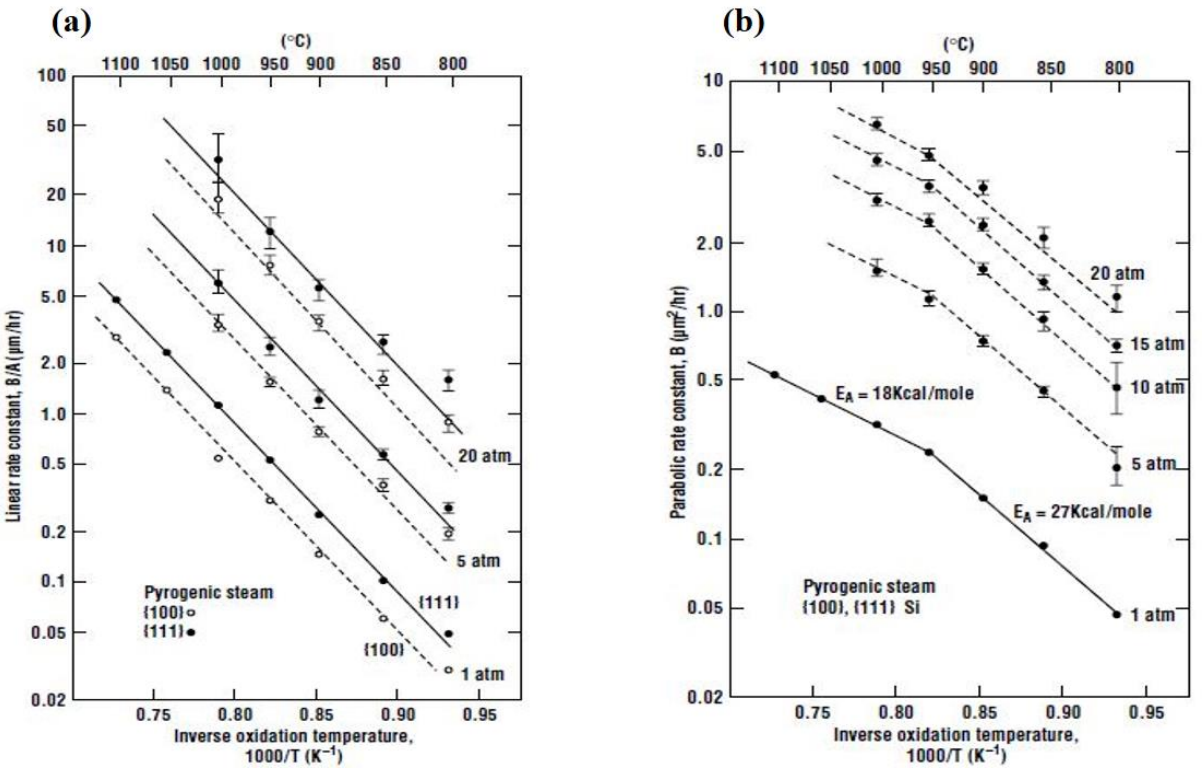

Figure 3-5: Pressure dependence of rate constants, (a) parabolic and (b) linear; graph adopted from (Campbell 2008)

Time offset parameter, τ

Eventually concerning the constant parameter *B*, Eq. (3-14) which is proportional to the partial pressure it is obvious that the parameter τ will reduce with the partial pressure increase for both wet and dry oxidation processes. That means at high pressure the τ will be zero.

$$\tau = \frac{x_i^2 + Ax_i}{\mathbf{B}}$$

3. Crystal orientation dependence of oxide growth

As the surface density of atoms is dependent on crystal orientation, oxidation rates are expected to be influenced by crystal orientation through the rate constant of reaction k_s factor, which is shown in D-G model. Based on the calculated properties of silicon crystal planes Table 3-2, silicon crystal orientation (111) must show the higher rate constants, due to more available for reaction Si – Si bonds.

Table 3-2: Calculated properties of silicon crystal planes.

Crystal Orientation	Area of unit cell [cm^2]	Si atoms in area	Si bonds in area	Bonds available	Bonds [10^{14} cm^{-2}]	Available bonds [10^{14} cm^{-2}]
(111)	$1/2\sqrt{3a^2}$	2	4	3	15.68	11.76
(100)	a^2	2	4	2	13.55	6.77

Parabolic rate constant *B*

Regarding to its equation, as it was excited by D–G analysis, the parabolic rate constant is independent to the constant rate of reaction k_s and at the same time to the crystal orientation.

$$B = \frac{2DHP_g}{N_1} \quad \leftrightarrow \quad \mathbf{B \neq f(Crystal\ orientation)} \tag{3-28}$$

Parameter *A*

Regarding to the equation of parameter *A* which contains the factor k_s it is obvious that this parameter will be orientation dependent.

$$A = 2D\left(\frac{1}{h} + \frac{1}{k_s}\right) \approx \frac{2D}{\mathbf{k_s}} \quad \leftrightarrow \quad \mathbf{A = f(Crystal\ orientation)} \leftrightarrow k_s \uparrow\uparrow \quad A \downarrow\downarrow \tag{3-29}$$

Linear rate constant *B/A*

Linear rate constant gains its proportional dependence on crystal orientation via the rate constant of reaction (k_s) which is introduced by parameter *A*:

$$\frac{B}{A} \approx \frac{k_s H P_g}{N_1} = \frac{\mathbf{k_s} H P_g}{N_1} \quad \leftrightarrow \quad \mathbf{\frac{B}{A} = f(Crystal\ Orientation)} \leftrightarrow k_s \uparrow\uparrow \ \frac{B}{A} \uparrow\uparrow \tag{3-30}$$

Experimental data for wet oxidation (Table 3-3), is used as an example to show the crystal orientation dependence of the rate constants. These table shows that the ratio of the linear rate constant for crystal orientation (111) to (100) is in average equal to 1.68. Thus this value must be applied to convert the linear rate constant of crystal orientation (100) to (111) and vice versa. Moreover, using Eq. (3-31) and the constant value of parabolic rate constant *B* which is independent of crystal orientation, it is easy to determine the parameter *A* using:

$$\frac{\left(\frac{B}{A}\right)_{111}}{\left(\frac{B}{A}\right)_{100}} = 1.68 \quad \leftrightarrow \quad \left(\frac{B}{A}\right)_{100} = \frac{\left(\frac{B}{A}\right)_{111}}{1.68} = Z \tag{3-31}$$

$$\left(\frac{B}{A}\right)_{100} = Z \quad \leftrightarrow \quad A_{100} = \frac{B}{Z} \tag{3-32}$$

Table 3-3: Rate constants for silicon oxidation in H_2O - 0.85bar, table adopted from (HongKong n.d.)

Oxidation Temperature [°C]	Orientation	B/A [µm/h]	B/A ratio (111)/(100)
900	(100)	0.150	1.68
	(111)	0.252	
1000	(100)	0.664	1.75
	(111)	1.163	
1100	(100)	2.977	1.65
	(111)	4.926	

Parameter τ

Looking at the equation of parameter τ, it found to be proportional to parameter A which is dependent on the crystal orientation. That means, the parameter τ must be converted using the correct A parameter:

$$\tau = \frac{x_i^2 + \mathbf{A}x_i}{B} \quad \leftrightarrow \quad \tau_{100} = \frac{x_i^2 + \mathbf{A_{100}}x_i}{B} \quad \leftrightarrow k_s \uparrow\uparrow \; A \downarrow\downarrow \; \tau \downarrow\downarrow \tag{3-33}$$

4. Silicon wafer doping

Another important aspect in thermal oxidation process is the doping level of Si wafers that will be used as substrates during SiO_2 growth. During thermal oxidation, thin film grows at a constant rate of 55% above and 45% below the initial interface. That means the doping impurities will redistribute at the interface until its chemical potential will be the same on each side of the interface. The ratio of the equilibrium of the impurity in Si to that in SiO_2 at the interface is called the equilibrium segregation coefficient. This coefficient is depended on diffusivity of the impurity in the oxide and the rate at which the interface moves with respect to the diffusion rate. For instance if the diffusivity of the impurity is large, it can diffuse through the oxide layer rapidly, thereby affecting the profile near the Si-SiO_2 interface.

3.3 Chapter Summary

The physical mechanisms of thermal oxidation of Silicon are presented in this Chapter. The Deal-Grove model, which is in very good agreement with experimental data on dry and wet oxidation is presented in detail and the relevant experimental variables that affect its parameters are discussed. In what follows the theoretical model will be placed under scrutiny through a series of experiments performed in the Research Unit for Nanostructured Materials Systems.

CHAPTER 4 EXPERIMENTAL INVESTIGATION OF THERMAL OXIDATION: MATERIALS AND METHODS

4.1 Chapter Outline

A good understanding of the synthesis and characterization techniques allows a correct analysis of samples and results. Therefore, this chapter describes in detail the preparation of samples and experimental techniques used to characterize them. Initially the fabrication of silicon oxide thin films via dry thermal oxidation process is described and subsequently characterization techniques such as uv-vis spectrophotometry, AFM and XRR are introduced.

4.2 Synthesis of SiO_2 Thin Films

4.2.1 Thermal Oxidation System

The SiO_2 thin films are fabricated through the dry thermal oxidation process described in Chapter 3. Dry thermal oxidation process is generally a simple technique which grows oxides by supplying oxygen through a gas source which in turn reacts with the silicon on the surface of wafers at high temperatures. A schematic of the equipment used in our study is shown in Figure 4-1. A typical dry oxidation system consists of a horizontal furnace with heating elements around a fused silica tube, gas lines, mass flow controllers, pressure control valve, and a vacuum pump.

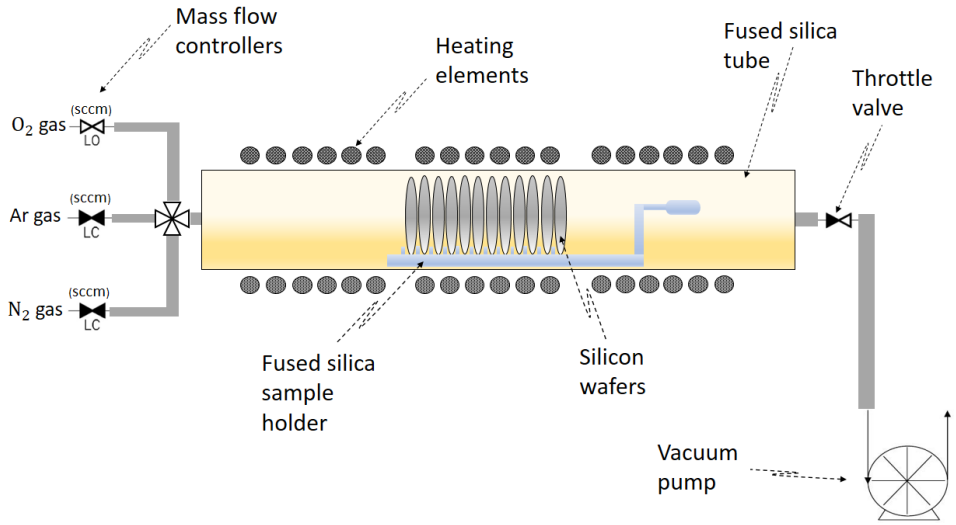

Figure 4-1: Schematic explanation of main components of a horizontal furnace which was used for dry thermal oxidation of silicon wafers.

The furnace that has been used for synthesis of SiO_2 thin films is actually a Thermal Chemical Vapor Deposition (TCVD) system that has been recently installed in the Synthesis Laboratory of the Research Unit for Nanostructured Materials Systems (RUNMS) and has been purchased from planarTECH. The main use of the TCVD system is to fabricate 2D materials like graphene or carbon nanotube, but the system can also be used for many other tasks like annealing of thin films, transformation of pre-ceramic polymers to ceramics and thermal processing of materials in controlled environments. We here exploit this system for studying the dry thermal oxidation of silicon.

The TCVD system (see Figure 4-2) consists of 3 zone high-temperature furnace, horizontal fused silica tube, LabVIEW control software, dry pump and nitrogen (N_2), argon (Ar), oxygen (O_2) and methane (CH_4) gas lines. The maximum operating temperature can reach 1200^{o}C and maximum oxygen flow rate 200 standard cubic centimeters per minute (sccm). Detailed specifications of the TCVD system can be found in page 130.

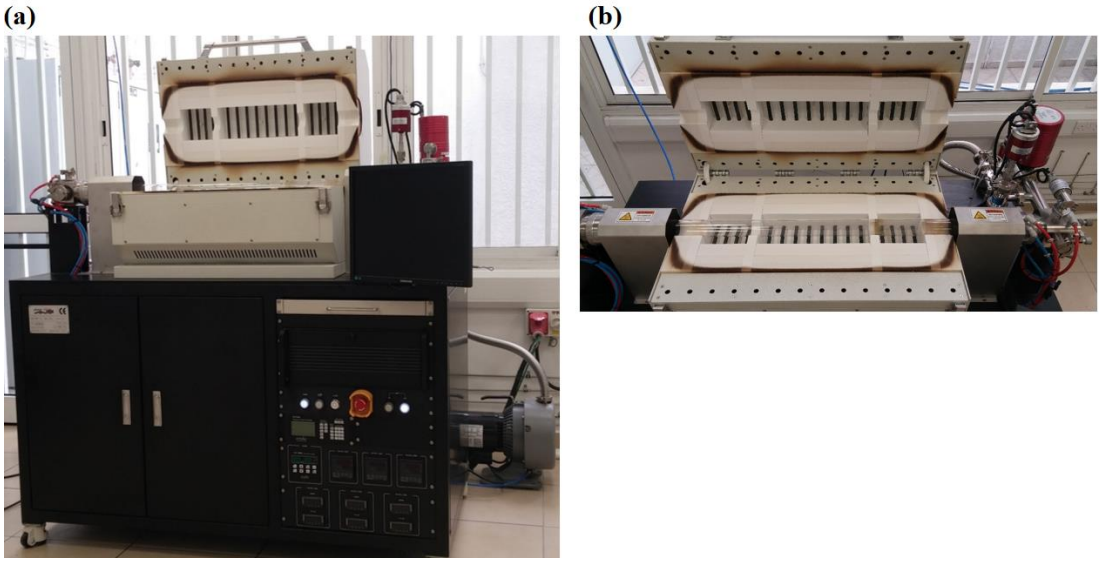

Figure 4-2: (a) TCVD system used for dry thermal oxidation process, (b) upper view of the main chamber

4.2.2 Fabrication process

Silicon wafers synthesized with Czochralski method, thickness 525±25 μm, n-typed doping (Phosphor) and flat orientation {110} are used as substrates for growth of thermal silicon oxides. In order to fit the silicon wafers into the chamber of the furnace, the original wafers were cut into smaller pieces using a cutter (Figure 4-3).

Figure 4-3: Si wafer and its pieces after been sliced using a cutter

The wafers were ultrasonically cleaned in acetone solution for 10 min and dried with high pressure nitrogen gun (see Figure 4-4b) in order to remove any organic dirt from their surface. The Ultrasonic Cleaner (DG-600, MRS laboratory products) and acetone used in this study are shown in Figure 4-4a.

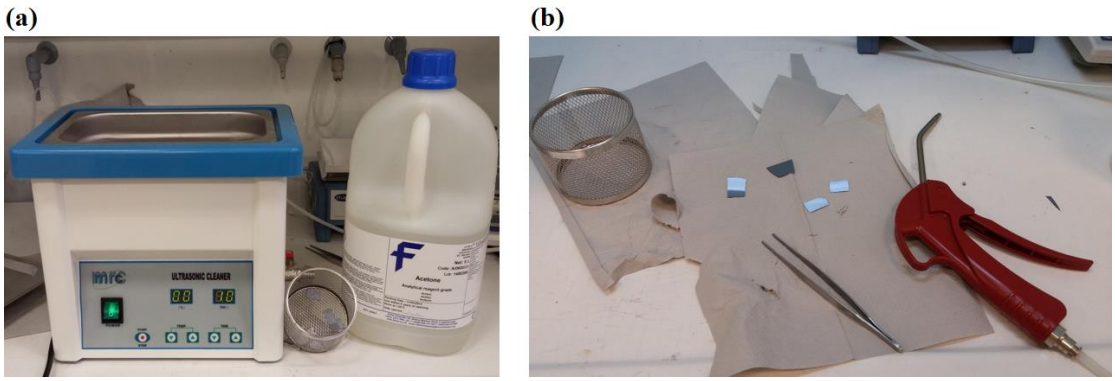

Figure 4-4: (a) Ultrasonic cleaning of silicon wafers in Acetone solution, (b) drying with compressed N_2 gun

For every oxidation experiment four samples were placed into the central zone (#2) of the TCVD furnace (Figure 4-5). All samples were in direct contact with the fused silica tube.

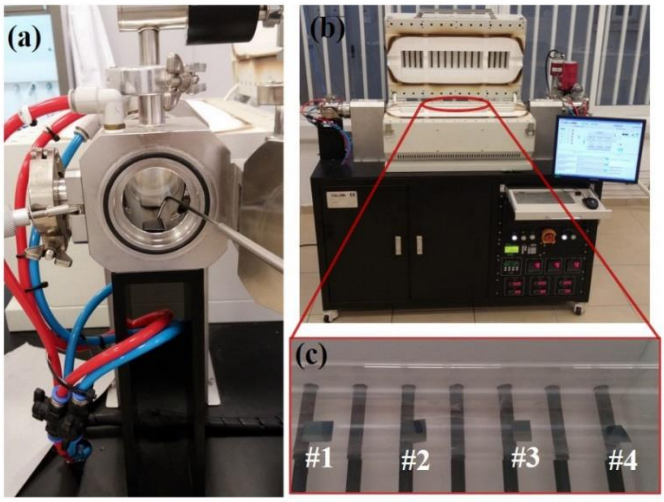

Figure 4-5: (a) sample placement into the fused silica tube, (b) zone #2, where the samples were placed and (c) sample distribution in the zone #2

Before the start of the procedure, it was important to define the thermal cycle of the process, namely the temperature, time and gases that will be used. Figure 4-6 presents an example of a thermal cycle which refers to 2 hour of thermal oxidation but was applied for all the fabricated samples, with respect to their exposure times. According to that graph, the whole process starts with only Argon gas flow (100 sccm), continues with only Oxygen gas flow (200 sccm) after 800°C and finishes again with only Argon gas from 800°C until the cover is opened. The usage of Ar gas at the initial and final stage of the oxidation process is in order to clean the oxidation chamber from contamination species and reduce the surface states of the produced silicon dioxide layers (Campbell 2008). On the other hand, the introduction of O_2 gas before reaching the working temperature (1100^{o}C) is performed in order to give some time (about 15 minutes) to the system to reach a steady state condition of O_2 partial pressure.

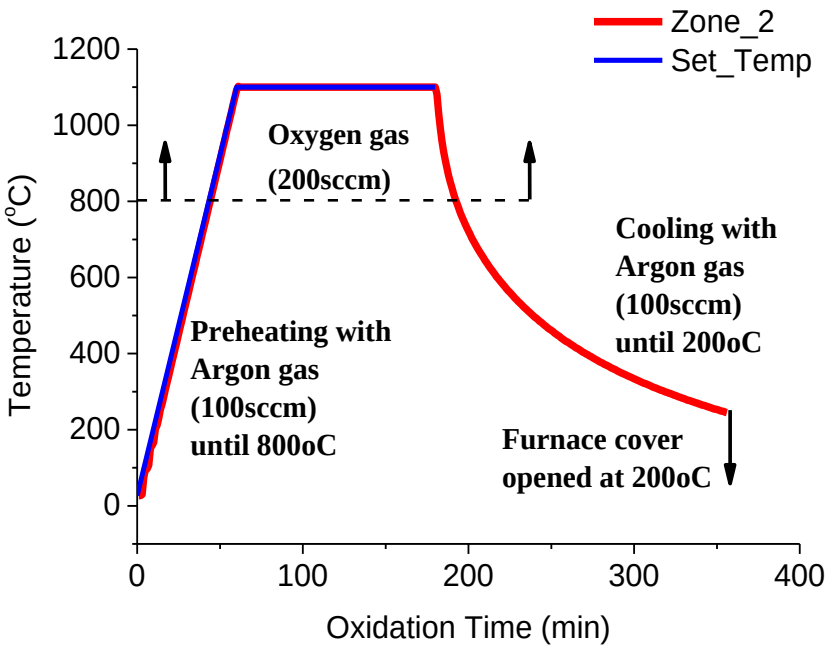

Figure 4-6: Thermal cycle of the silicon dioxide thin films fabrication (i.e. TCVD22_2h)

The planarTECH control software (Figure 4-7) was used to define parameters for each oxidation process by controlling the temperature, time, valves, and rotary pump under safe conditions.

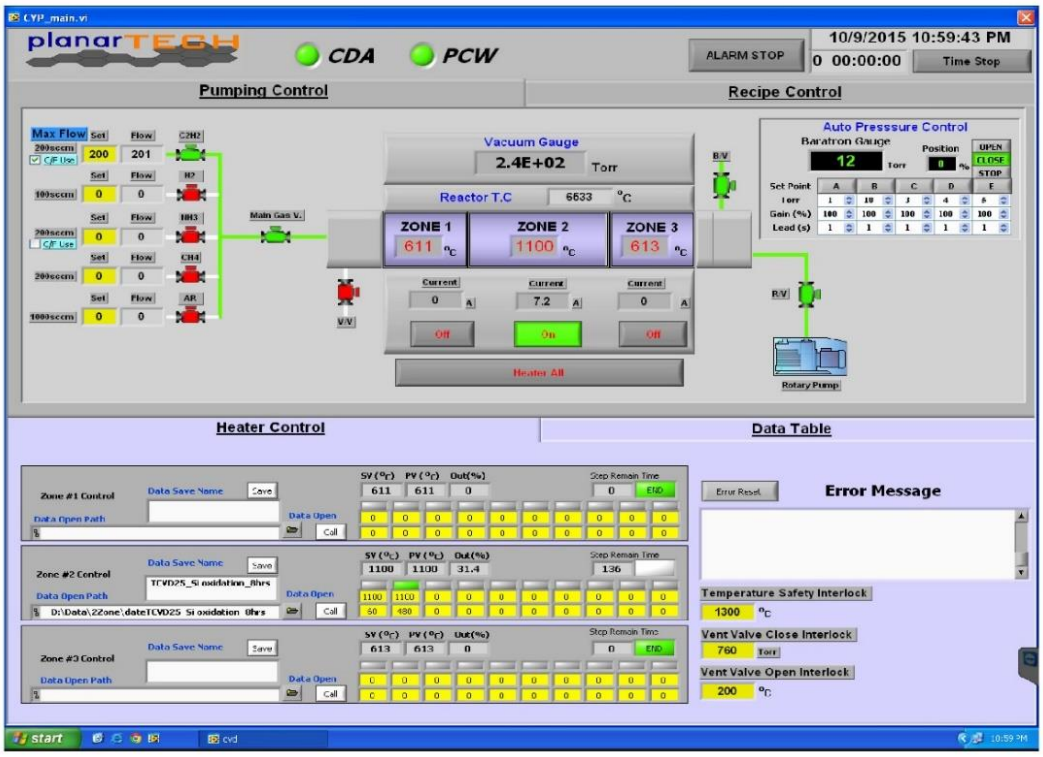

Figure 4-7: LabVIEW Control software of the TCVD system

Seven samples of thermally grown SiO_2 samples were fabricated and stored in plastic petri dishes (Figure 4-8). These samples were fabricated at 1,100ºC, same thermal cycle, but different oxidation times, and different partial pressures. The fabricated samples along with their synthesis characteristics are summarized in Table 4-1.

Table 4-1: Summary of the fabricated samples

Set of samples	Sample name	Time of exposure at 1100°C [h]	Average partial pressure of O2 (200sccm) [bar]
1	TCVD_27	0.5	0.29
2	TCVD_21	1	0.30
3	TCVD_22	2	0.30
4	TCVD_23	3	0.30
5	TCVD_26	4	0.32
6	TCVD_24	6	0.26
7	TCVD_25	8	0.27

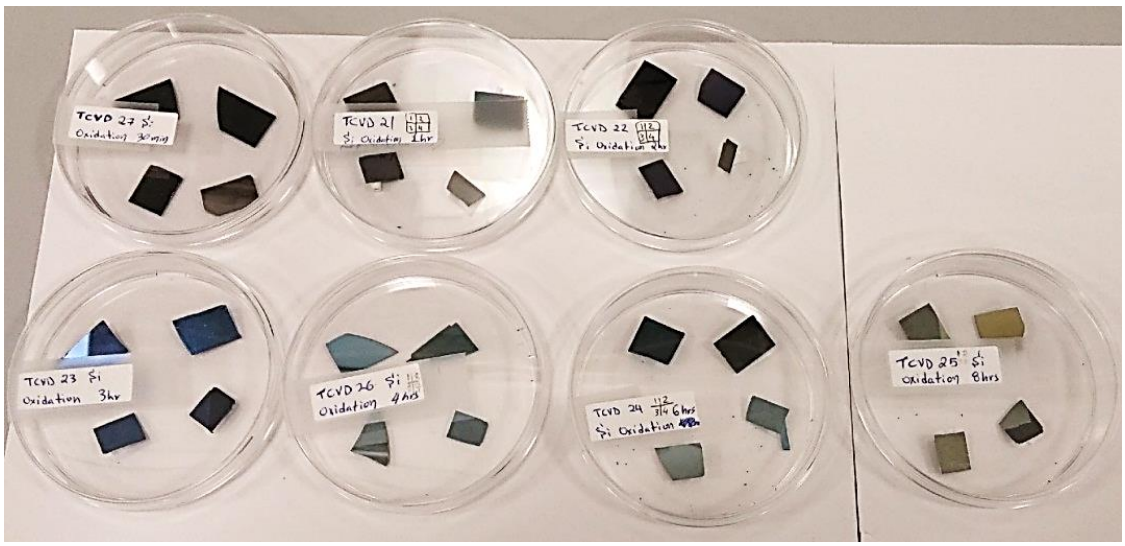

Figure 4-8: Thermally grown SiO_2 samples

4.3 Characterization Techniques

The optical, topographical and physical properties of all grown materials have been studied. Optical properties are probed using ultraviolet–visible (UV-VIS) spectrophotometry, topography and roughness using Atomic Force Microscopy (AFM), density and film thickness

using X-ray Reflectivity (XRR) and wetting properties using contact angle (CA) measurements.

4.3.1 UV-VIS Reflectance Spectrophotometer

UV/VIS Spectrophotometry

UV-VIS is a technique that refers to absorption spectroscopy or reflectance spectroscopy in ultraviolet – visible wavelength range. It uses light in visible, near UV and near infrared (IR) ranges. In this work the reflectance spectrum of all the fabricated SiO_2 thin films was recorded in order to investigate their optical properties (color) and how they change with respect to the oxidation time.

The spectrometer used to record the reflectance spectra of each SiO_2 thin film is a Thetametrisis FR-Basic UV/VIS Spectrometer, which contains FR-Monitor Software for analysis purposes. The spectrometer installed at RUNMS is shown in Figure 4-9b. The basic components of FR-Basic Spectrometer is the light source which consists of Deuterium and Halogen lamps operating at wavelengths of 250–850 nm, optical fibers which transport the light and FR-Monitor software (see Figure 4-9a) that analyzes the signals providing the reflectance, absorbance and transmittance spectra.

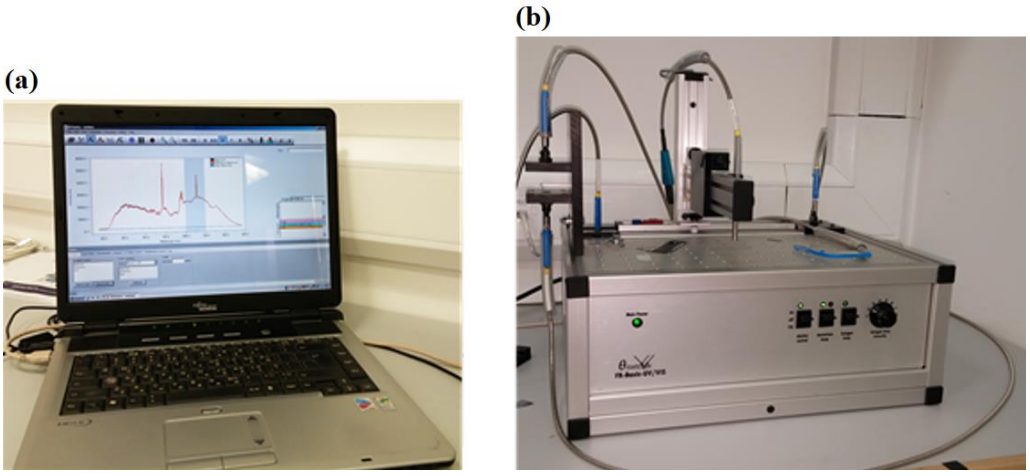

Figure 4-9: (a) FR-Monitor analysis and control software, (b) FR-Basic UV/VIS Spectrometer

The procedure for data collection is shown in Figure 4-10, where the generated light travels through optical fibers and interacts with the material that is under investigation. The reflected light is detected and transferred through optical fiber to the photocell detector (spectrometer). Afterwards the collected signal is converted to wavelength numbers and used in mathematical equations which compute and plot the reflectance spectra.

It is important to mention that all the measurements were taken at room temperature and for precise measurements of the reflectance characteristics correction of room light sources was taken into account through:

$$R(\lambda) = \left(\frac{I_s - I_d}{I_r - I_d}\right) \times 100\% \qquad (4\text{-}1)$$

where I_d is the dark intensity, i.e., the light intensity recorded by the spectrometer with the light source switched–off, I_s is the source intensity (incident light), and I_r is the reflectance intensity (reflected light).

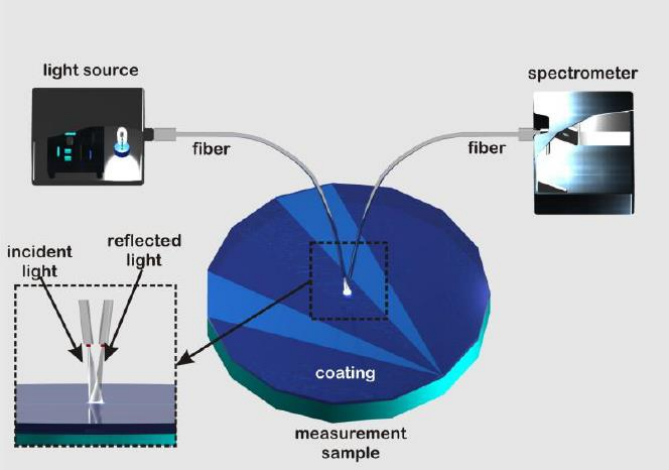

Figure 4-10: Schematic diagram of optical reflectance spectroscopy procedure, image adopted from (Thetametrisis)

4.3.2 White Light Reflectance Spectroscopy (WLRS)

The oxide thickness is a very important parameter of the oxidation process, and thus many ways have been developed to measure it. In this work the thickness calculation of oxide layer was achieved by White Light Reflectance Spectroscopy (WLRS). The WLRS is a methodology that uses a broad band light source, in our case UV-VIS and a PC-driven spectrometer to calculate the thickness of each layer. WLRS uses white light produced by combined Halogen and Deuterium lamps, which is guided through a bifurcated optical fiber onto the sample under the investigation from where after the reaction it is reflected and collected by reflection probe in order to finally direct it via optical fiber to the spectrometer. The schematic diagram of a WLRS set up is shown in Figure 4-11.

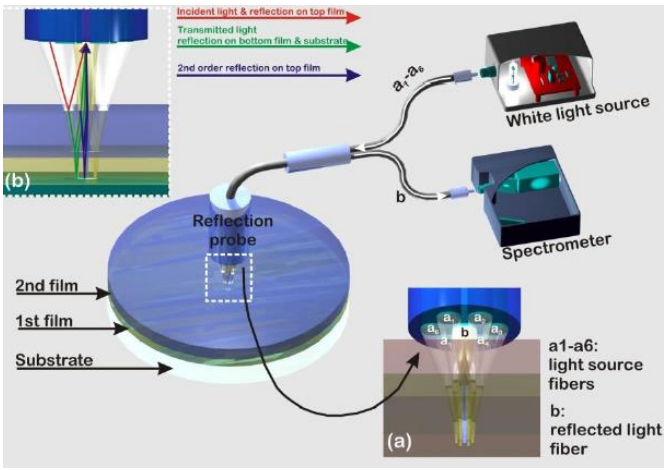

Figure 4-11: Typical WLRS set up. (a) detail of the configuration of reflection probe, (b) detail of the light optical path through a two layer sample, image adopted from (Thetametrisis.com 2015)

The sample under investigation must consist of a stack of transparent and/or semi–transparent films over an appropriate reflective substrate. In our case the investigated samples consisted of the thermally grown SiO_2 films and the reflective substrate was the underlying Si. The total reflection coefficient for a k-layer sample, in FR–Monitor software is calculated by Abeles approach (Thetametrisis.com 2015). From this set of equations the reflectance from any k-th layer can be calculated using the following equation:

$$\rho_{k-1}e^{i\Delta_{k-1}} = \frac{r_{k-1} + \rho_k e^{i\Delta_k - 2i\delta_{k-1}}}{1 + r_{k-1}\rho_k e^{i\Delta_k - 2i\delta_k}} \tag{4-2}$$

where ρ is the amplitude, r is the Fresnel coefficient, and Δ is the phase. In the case of a SiO_2 layer between the substrate (Si) and the environment (air) the total energy can be written as (Thetametrisis.com 2015):

$$E = \frac{A}{B} \tag{4-3}$$

$$A = r_{01}^2 + r_{12}^2 + 2r_{01}r_{12}\cos\left(\frac{4\pi}{\lambda}n_1t_1\right) \tag{4-4}$$

$$B = 1 + r_{01}^2 r_{12}^2 + 2r_{01}r_{12}\cos\left(\frac{4\pi}{\lambda}n_1t_1\right) \tag{4-5}$$

where n_i is the refractive index of each layer (i=0 for air, 1 for the SiO_2 layer and 2 for the Si), t_i is the thickness of each layer, λ its wavelength, and r_i the Fresnel reflection coefficient (0: air, 1: SiO_2 and 2: Si). The light propagation of a layer stack together with the reflectance spectra of SiO_2 thin film over a Si substrate are shown in Figure 4-13 and Figure 4-13 respectively.

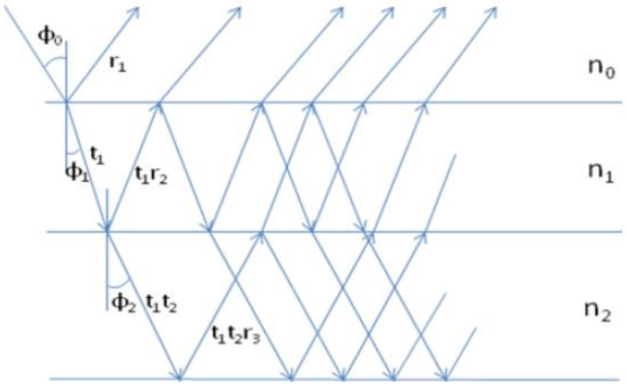

Figure 4-12: Light propagation schematic in a stack consisting of one layer stack

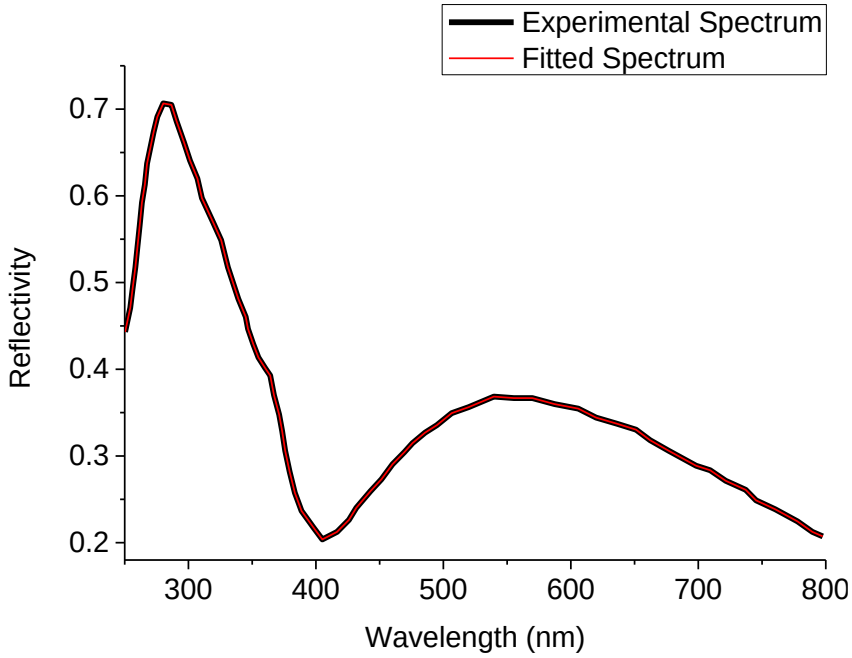

Figure 4-13: Reflectance spectrum of SiO_2 layer on Si substrate

The fitting of experimental spectrum (Figure 4-13b), is performed via Eqs. (4-2) – (4-5) using the Levenberg–Marquardt algorithm. It is important to mention that before the fitting process, fitting parameters such as number of layers, material of each layer, and their estimate

thicknesses must be applied. In particular case, air and Si layers with infinite thickness and SiO_2 with estimated range of thickness from 0–200 nm were chosen, as it is shown in Figure 4-14.

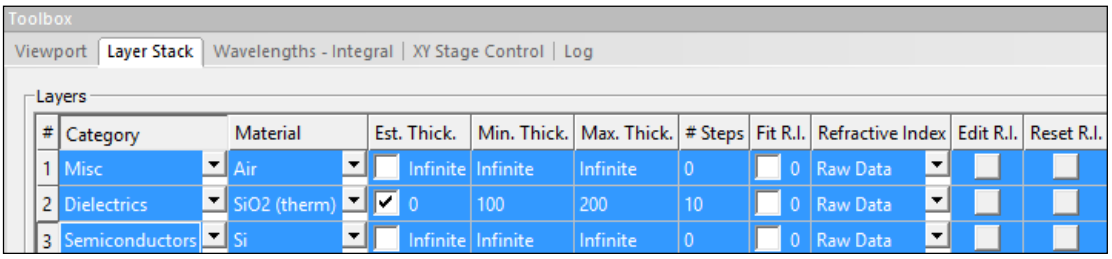

Figure 4-14: Fitting parameters of FR – Monitor software, image adopted from (Thetametrisis.com 2015)

With the selection of materials FR–Monitor's database is notified. This database consists of refractive indices (n_i) of different materials which have been already calculated by spectroscopic ellipsometry. Consequently, after the completion of fitting process, the FR–Monitor software correlates the refractive indices with embedded database and presents the calculated thickness, 198.7 nm, as it is shown in Figure 4-15.

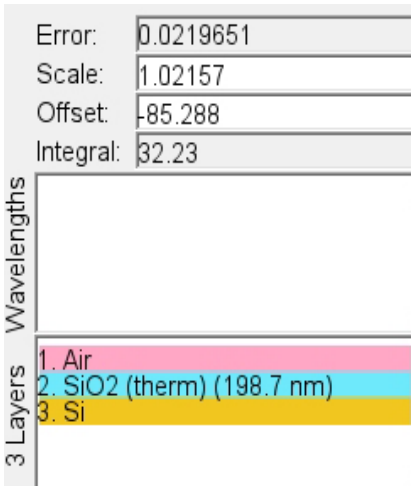

Figure 4-15: Calculated thickness by FR – Monitor software, *Thetametrisis* (i.e. 8hr thermally grown SiO_2 – sample # 4)

4.3.3 Atomic Force Microscopy (AFM)

Atomic force microscopy (AFM) was been developed by IBM scientists Binning, Quate and Gerber in 1986. AFM is very high–resolution type of scanning probe microscopy allowing to characterize and manipulate a wide range of materials at the nanoscale. Due to its abilities of high resolution surface roughness determination, identification of atoms at the surface, evaluation of interaction between a specific atom and its neighbors, AFM is applicable in many scientific areas such as semiconductor physics, cellular biology and material science.

The basic components of an AFM system are a cantilever with a sharp tip (probe) connected to a small piezoelectric element, a laser beam, a photodiode detector and a piezoelectric scanner, as illustrated in Figure 4-16b.

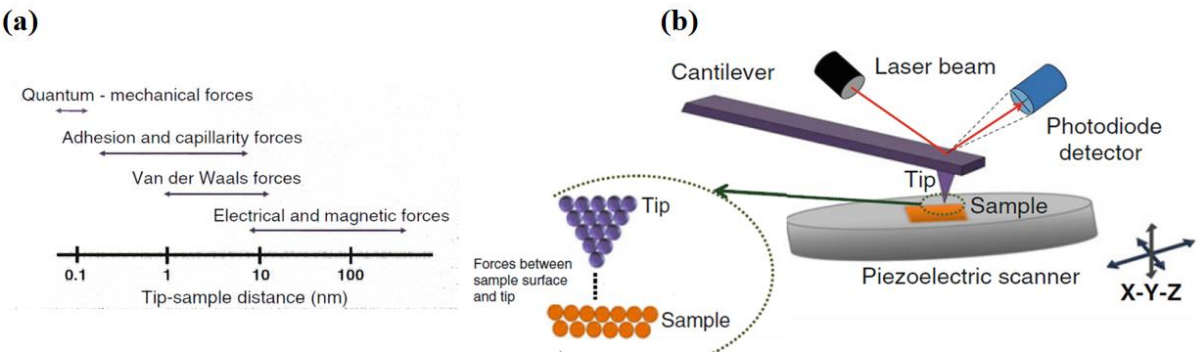

Figure 4-16: (a) Interaction forces between tip and sample in AFM, (b) schematic diagram of AFM, image adopted from (Doctoral 2014)

AFM operation is based on quantifying the interactions between a tip and the surface of the sample (Figure 4-16a). These interactions cause the bending of the cantilever which is recognized by the photodiode after the change of laser beam which is reflected from the back surface of the cantilever. The photodiode detector converts the deflection of cantilever into an electrical signal which is later being processed by electronically in order to finally define the topography in 2 or 3 dimensions. In this work, topography and roughness of thermally grown SiO_2 thin films were determined using an NTEGRA Prima, NT-MDT instrument which has been recently installed at the Research Unit for Nanostructured Material Systems (RUNMS) at Cyprus University of Technology (Figure 4-17).

Figure 4-17: NT-MDT NTEGRA AFM, (RUNMS Characterization Lab, 2015)

AFM measurements were performed in air, at room temperature, using silicon tips with resonance frequency of 200 – 300 kHz and an average tip radius ≤ 10 nm. The samples #2 (Figure 4-2) were chosen for AFM investigation and the used operating modes were set to constant force and semi-contact mode.

Constant force is the mode in which a feedback mechanism is employed to adjust the tip-to-sample distance in order to maintain a constant force between the tip and the sample. This is important because if the tip was scanned at a constant height, a risk would exist that the tip collides with the surface, causing damage.

Tapping or semi-contact mode, is a dynamic mode, where the cantilever is driven to oscillate up and down at or near its resonance frequency by a small piezoelectric element. The amplitude of this oscillation is greater than 10 nm, typically it is 100 – 200 nm, (Ntmdt.com).The interaction forces acting on the cantilever when the tip approaches the surface (Figure 4-16a), cause the amplitude of this oscillation to decrease as the tip gets closer to the surface. An electronic servo uses the piezoelectric actuator to control the height of the cantilever. The servo adjusts the height to maintain a set cantilever oscillation amplitude, as the cantilever is scanning over the sample.

The images taken from AFM were analyzed using an NT-MDT software. The collected data for each sample consisted of 10 μm x 10 μm topography and 3D Route Mean Square (RMS) roughness which is calculated by the software using the Eq. 4-6 which is based on (Figure

4-18). This data was used to investigate the influence of thermally grown SiO_2 thin films on Si substrate.

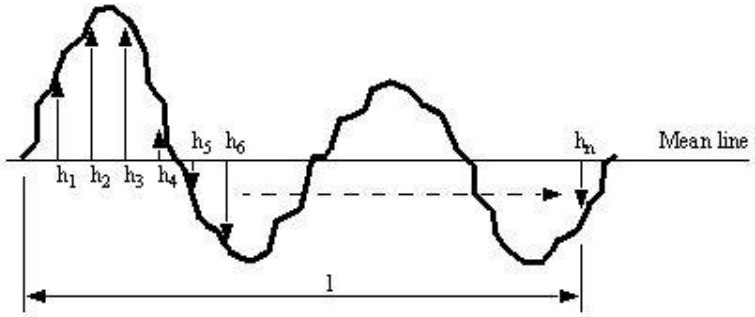

Figure 4-18: Root mean square roughness calculation formula

$$\mathrm{RMS} = \mathrm{R_q} = \sqrt{\frac{\mathrm{h_1^2} + \mathrm{h_2^2} + \mathrm{h_3^2} + \cdots + \mathrm{h_n^2}}{\mathrm{n}}} \tag{4-6}$$

4.3.4 X-ray Reflectivity (XRR)

X–ray reflectivity (XRR) is a technique used to analyze the reflection intensity curves from grazing incident angles of X –ray 'beam' to determine several thin–film parameters including thickness, density and surface or interface roughness, (Yasaka 2010). XRR technique is applicable to:

- Study single crystalline, polycrystalline or amorphous materials
- Evaluate the surface and interface roughness nondestructively
- Determine the layer structure of a multilayer or single–layer film, and
- Measure film thickness from several to 1000 nm

The physics of XRR technique are based on X–ray wave reflection and refraction. In the case of X–ray incident waves the refractive index of material is slightly less than 1, as a result the phase velocity is slightly larger than the light velocity. Generally interaction with flat surface causes X–ray's total reflection (Figure 4-19a), when the angle between the beam and the surface is less than the critical angle (θ_c). On the other hand for angles greater than the critical angle, the X–rays penetrate into the material reducing rapidly the reflection profile (Figure 4-19b).

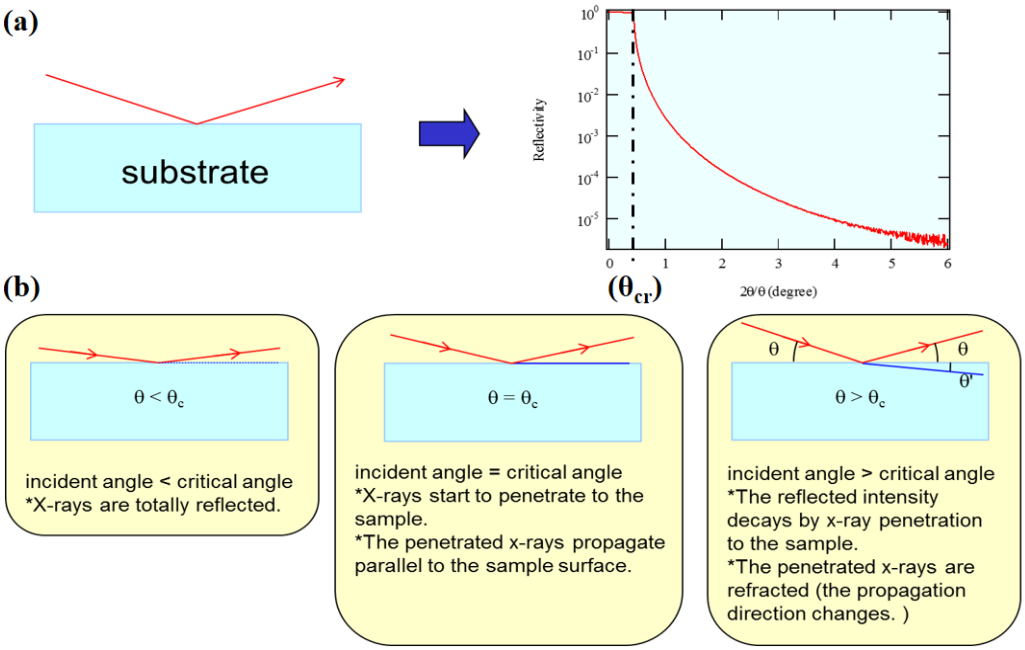

Figure 4-19: (a) - X–ray interaction with flat Si surface, (b) X-ray penetration in to the material, image adopted from (Yasaka 2010)

Additionally the reflected waves from the top and bottom interfaces interfere constructively or destructively creating an oscillation profile on the reflection intensity vs. grazing incident angles as shown in (Figure 4-20). Eventually these oscillations provide thickness, density and roughness information that can be extracted after fitting a layered model X-ray interaction.

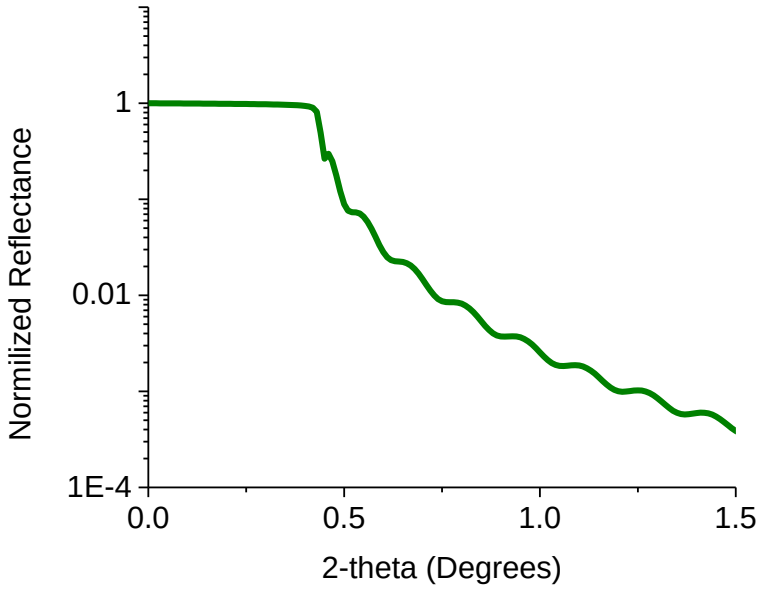

Figure 4-20: XRR Reflectance profile

The study of the XRR reflectance profile revealed that the period of the oscillations has direct correlation with film thickness. The thicker the film, the smaller is the period of the oscillation and vice versa, (Figure 4-21b). Similarly the critical angle (θ_c) and the amplitude of the oscillations provide information about the difference in density between the substrate and film. The higher is the difference in density the larger is the critical angle and the amplitude of the oscillations and vice versa, (Figure 4-21, (c) and (d). Finally the surface and interface roughness is provided by the decay rate of X –ray reflectivity. The higher is the decay rate, the larger is the surface roughness and vice versa, (Figure 4-21a), (Yasaka 2010).

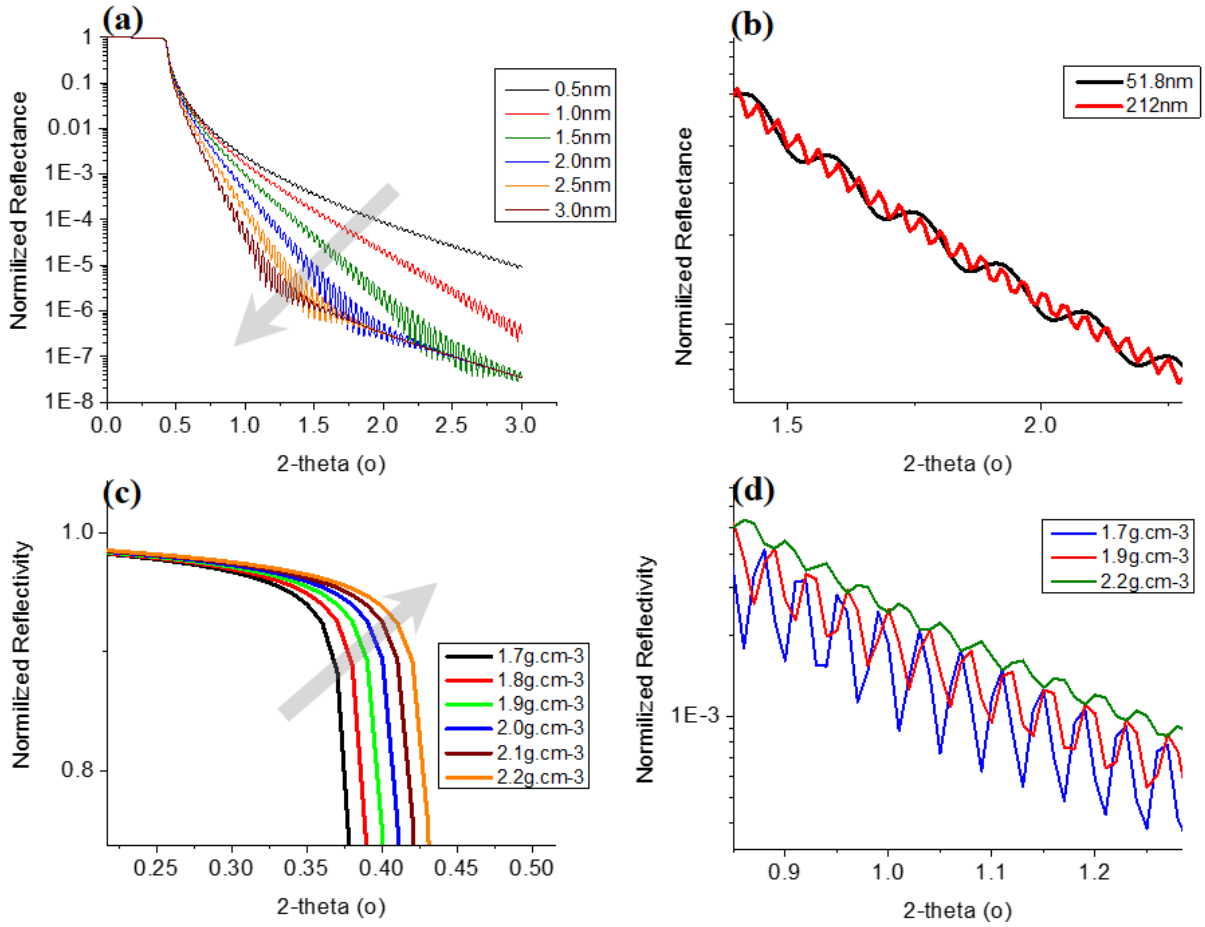

Figure 4-21: XRR profile analysis, (a) Surface roughness effect on decay in X–ray reflectance, (b) Thickness of film effect on the period of oscillation, (c) Density effect on critical angle, (d) Density effect on amplitude of the oscillation.

In this work the diffractometer of Research Unit for Nanostructured Materials Systems (RUNMS) Rigaku Ultima IV (Figure 4-22), with a 285mm radius goniometer operating in θ/θ mode was used to obtain the XRR profiles for each fabricated sample. It is important to mention that for films thicker than 150 nm, oscillations of X–ray reflectivity cannot be observed using

the default optics system. This is because the period of the oscillation changes depending on film thickness. With larger film thickness, the period of the oscillation is smaller, and the resolution of the X–ray optics used for measuring the reflectivity must be increased. Thus, based on WLRS technique only the samples with thickness values less than 150 nm will be investigated using XRR technique.

Figure 4-22: Rigaku Ultima IV, RUNMS Characterization Lab, 2015

4.4 Chapter Summary

The planarTECH system was used to thermally grow (1100°C) silicon oxides at various oxidation times and pressure conditions. Seven samples were synthesized that were subsequently characterized physically, topographically, geometrically and optically. The principles of the major characterization techniques have been presented in this chapter, the results of which will be subsequently discussed.

CHAPTER 5 EXPERIMENTAL INVESTIGATION OF THERMAL OXIDATION: RESULTS AND DISCUSSION

5.1 Chapter Outline

The results obtained from the experimental investigation outlined in Chapter 4 will be presented and critically discussed within this chapter. The oxidation rates as well as the induced changes on the topographic, microstructural and optical characteristics of the thermally grown SiO_2 surfaces are discussed.

5.2 Oxidation Kinetics

5.2.1 Oxidation Thickness: Experiments

The kinetics of oxidation have been experimentally quantified by measuring the thickness of the oxidized material for various oxidation times. Table 5-1 presents the thicknesses of all SiO_2 films as measured through White Light Reflectance Spectroscopy (WLRS). We recall that a stack of air/silicon dioxide/silicon was used in the fitting process for calculating the silicon dioxide thicknesses.

Table 5-1: Thicknesses of the fabricated sets of samples calculated using the WRLS technique.

Time of Oxidation [h]	0.5	1	2	3	4	6	8
Thick. Sample #1 [nm]	46	52.4	78.5	114.8	157	160	194.5
Thick. Sample #2 [nm]	51.8	58.2	89.2	125.3	168.5	171.9	212
Thick. Sample #3 [nm]	52.7	60.9	92.9	125.2	167.2	176.4	212.1
Thick. Sample #4 [nm]	51.5	56.1	80.3	116.8	157.9	165.4	198.7
Average Thickness [nm]	*50.50*	*56.90*	*85.23*	*120.53*	*162.65*	*168.43*	*204.33*
Standard Deviation	*3.04*	*3.59*	*6.93*	*5.52*	*6.04*	*7.21*	*9.08*

As it can be observed from Table 5-1, each set of samples exhibits different thickness values with respect to sample number. In fact, one can correlate the thickness variation for a given set with the location of the each sample within the T-CVD chamber (Figure 4-5); samples #2 and #3 which are situated within the center of the heater exhibit higher oxidation thicknesses

compared to samples #1 and #4 which are located at the edges towards the side zones with temperatures lower than the central region.

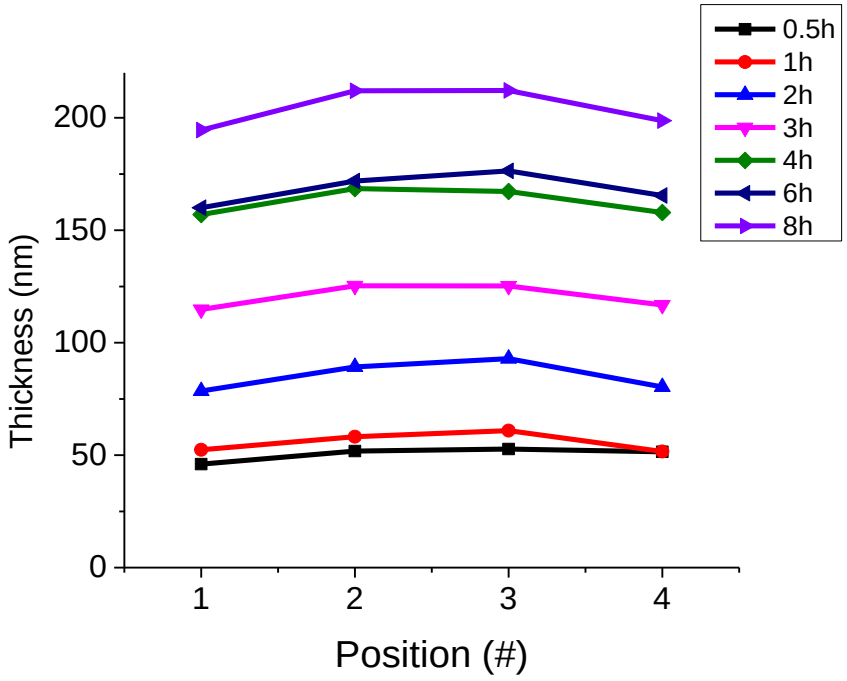

Figure 5-1: Thickness of each sample with respect to their position in the chamber of T-CVD system

In order to explain the difference in thickness of each sample with respect to their position in the chamber of T-CVD system, the theory of oxide growth, must be invoked. According to the theory of oxidation, the most important parameters that affect the oxide growth rate are the partial pressure of the oxygen, the crystal orientation of the Si wafers and the ambient temperature. Given the fact that all Si wafers have the same crystal orientation (100) and that the partial pressure is almost the same along the entire chamber of the T-CVD system, the temperature parameter must be investigated. Thus in Figure 5-2 the temperature and temperature profile of each zone during the oxidation process is presented. The temperature profiles show some differences between zones 1,2,3 which relate to the fact that the thermal elements of these zones were disabled during the oxidation process since all the samples were placed in zone 2. As a consequence this difference in temperature is the factor that led samples 1 and 4 to exhibit smaller thicknesses, result that is confirmed by Figure 5-1.

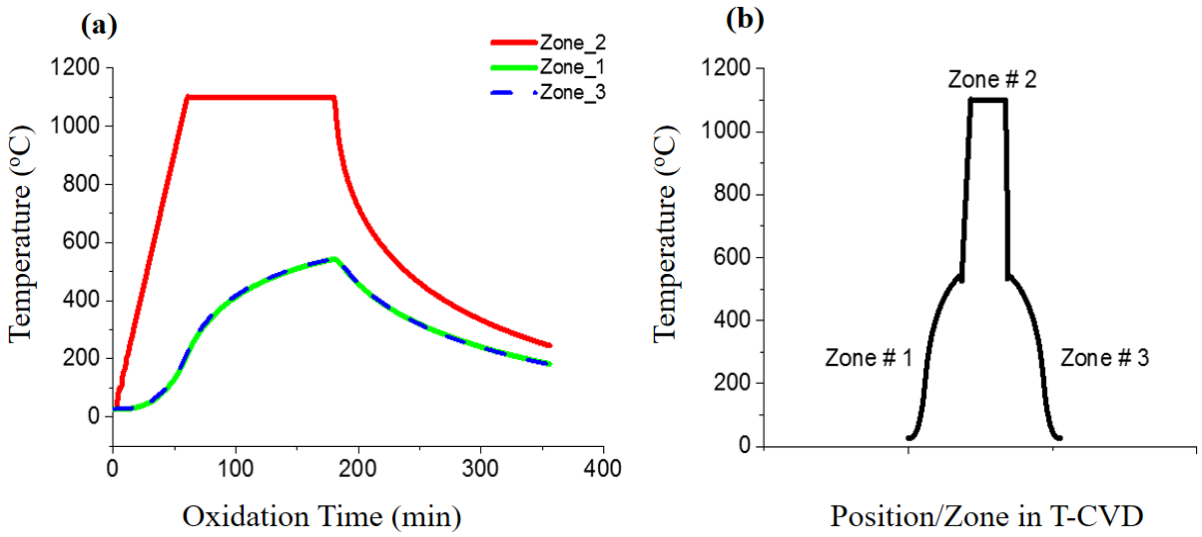

Figure 5-2:(a) Temperature vs. oxidation time in each zone of TCVD system, (b) Temperature profile in each zone during the oxidation process.

The oxidation rates calculated using the average thickness values from Table 5-1 are shown in Figure 5-3. According to that graph, the oxidation rates for short time are larger than those at relatively longer oxidation time. This can be explained through the theory of oxide growth, Chapter 3. The theory mentioned that while the oxide thickness increases, it takes more time for the oxygen species to diffuse through that dense layer and produce new oxide bonds.

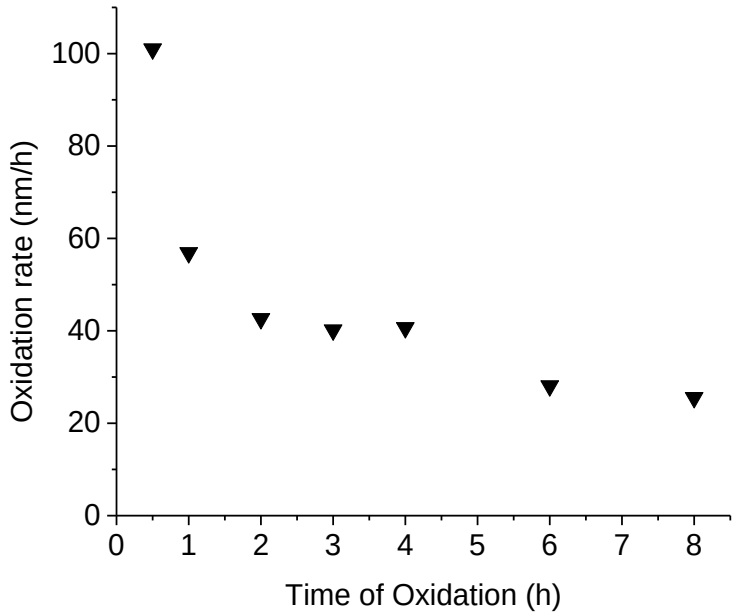

Figure 5-3: Thermal oxidation rates

5.2.2 Oxidation Thickness: Deal–Grove Model

To calculate the theoretical thickness based on the D–G model the rate constants of oxidation must be determined for each condition. Given that the oxidation process was performed at 1,100ºC, parameters *A*, *B*, *B/A* and τ could be selected using Table 5-2, that was proposed by Deal and Grove (Deal & Grove 1965). Since the values of these parameters are related to silicon wafers with crystal orientation (111) and oxygen partial pressure of 1 atm, correction factors on each parameter must be applied according to the theory that was presented in Section 3.2.3.

Table 5-2: Rate constants for Si (111) in dry oxidation process, (Deal & Grove 1965)

Oxidation Temperature [ºC]	A [μm]	B [μm2/h]	B/A [μm/h]	τ [h]
1200	0.040	0.045	1.12	0.027
1100	**0.090**	**0.027**	**0.30**	**0.076**
1000	0.165	0.0117	0.071	0.37
920	0.235	0.0049	0.0208	1.40

Rate constant correction due to partial pressure

Table 5-3 shows the average partial pressure of O_2 gas in the chamber of T-CVD system. Using these values and Eqs. (5-1) and (5-2) the correction of parameters B, B/A is performed.

Table 5-3: Average partial pressure values for each oxidation process

Sample name	Time of exposure at 1100°C [h]	Average partial pressure Pg of O_2 (200sccm) [bar]
TCVD_27	0.5	0.29
TCVD_21	1	0.30
TCVD_22	2	0.30
TCVD_23	3	0.30
TCVD_26	4	0.32
TCVD_24	6	0.26
TCVD_25	8	0.27

$$B(P_g) = B_{1atm} \times P_g \quad (5\text{-}1)$$

$$\frac{B}{A}(P_g) = \frac{B}{A}(1\ \text{atm}) \times P_g^{0.75} \tag{5-2}$$

$$\tau_{Pg} = \frac{x_i^2 + Ax_i}{B_{Pg}} \tag{5-3}$$

Rate constant correction due to crystal orientation

The correction of rate parameters due to the crystal orientation of the Si wafers was performed using Eqs. (3-31) and (3-32):

$$\frac{\left(\frac{B}{A}\right)_{111}}{\left(\frac{B}{A}\right)_{100}} = 1.68 \quad \leftrightarrow \quad \left(\frac{B}{A}\right)_{100} = \frac{\left(\frac{B}{A}\right)_{111}}{1.68} = Z \tag{5-4}$$

$$\left(\frac{B}{A}\right)_{100} = Z \quad \leftrightarrow \quad A_{100} = \frac{B}{Z} \tag{5-5}$$

Corrected rate constants values

Eventually, the corrected parameters are used to calculate the overall time offset value τ which depends on the crystal orientation of Si wafers (parameter *A*) and on partial pressure (parameter *B*). In order to calculate that value, an imaginary initial thickness t_i must be used in order to take into account the higher initial oxidation rate. This initial thickness can be calculated using *τ*, *A* and *B* values from Table 5-2 and solving Eq. (3-14) with respect to the initial thickness, as shown below:

$$\tau = \frac{x_i^2 + Ax_i}{B}$$

$$x_i = \frac{-A + \sqrt{A^2 + 4B\tau}}{2} = \frac{-0.090 + \sqrt{0.090^2 + 4 \times 0.027 \times 0.076}}{2} = 0.0188\ \mu m$$

Thus, the calculation of the corrected τ–values is given by:

$$\tau_{100\&P_g} = \frac{0.0188^2 + A_{100} \times 0.0188^2}{B_{P_g}}$$

Table 5-4 summarizes the corrected oxidation parameters used to calculate the theoretical thickness of the SiO_2 films.

Table 5-4: Corrected oxidation rate constants

Time	Oxidation Constant Parameters at 1100°C							
t [h]	B/A f(111) [μm/h]	B/A f(100) [μm/h]	A f(111) [μm]	A f(100) [μm]	Pg [bar]	B f = (1 bar) [μm²/h]	B = f(Pg) [μm²/h]	τ = f(100,Pg) [h]
0.5	0.3000	0.1786	0.090	0.1512	0.29	0.027	0.00783	0.41
1	0.3000	0.1786	0.090	0.1512	0.30	0.027	0.00810	0.39
2	0.3000	0.1786	0.090	0.1512	0.30	0.027	0.00810	0.39
3	0.3000	0.1786	0.090	0.1512	0.30	0.027	0.00810	0.39
4	0.3000	0.1786	0.090	0.1512	0.32	0.027	0.00864	0.37
6	0.3000	0.1786	0.090	0.1512	0.26	0.027	0.00702	0.46
8	0.3000	0.1786	0.090	0.1512	0.27	0.027	0.00729	0.44

As detailed in Section 3.2.3, the D–G model has 3 regimes which provide different equations to calculate the oxide thickness. The linear regime that predicts the oxide thickness for relatively small oxidation times, the parabolic regime which predicts the oxide thickness for relatively large oxidation times and the general equation of oxidation that covers both domains. In order to determine which equation will be used to calculate the theoretical thickness of the grown SiO_2 layers, the graph of Figure 5-4 and Table 5-4 are used in order to calculate the dimensionless group which refers to x-axis values of Figure 5-4. Therefore, the results presented in Table 5-5, show that the corresponding relationship that must be used in order to determine the correct thickness values is the general equation of oxidation since the dimensionless groups contains values in the 1–11 range.

$$\frac{t+\tau}{\frac{A^2}{4B}} \text{ dimensionless group}$$

Table 5-5: Oxidation parameters calculation for the case of each process that been mentioned

Time of Oxidation	A	B	τ	$\frac{t+\tau}{A^2/4B}$
0.5	0.1512	0.00783	0.41	1
1	0.1512	0.0081	0.39	2
2	0.1512	0.0081	0.39	3
3	0.1512	0.0081	0.39	5
5	0.1512	0.00864	0.37	8
6	0.1512	0.00702	0.46	8
8	0.1512	0.00729	0.44	11

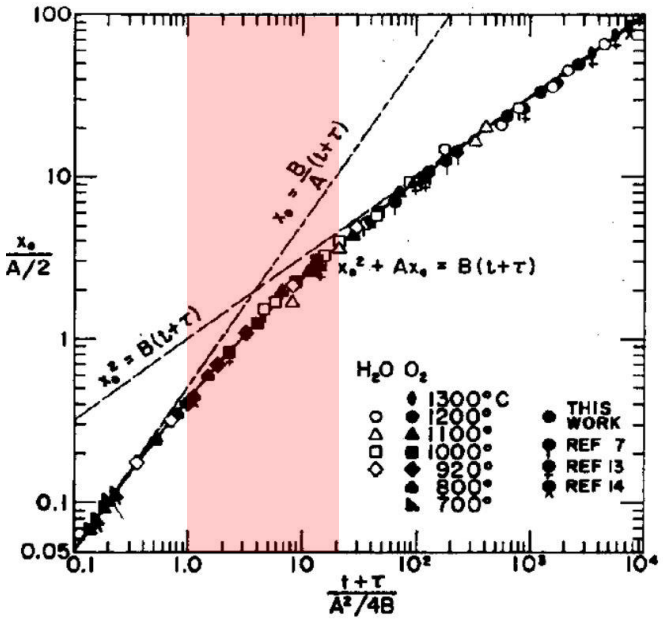

Figure 5-4: General relationship for thermal oxidation of silicon

Therefore, using the D–G general equation the theoretical thickness for each oxidation time is calculated and presented in Table 5-6 using the general Eq. (3-15). For comparison, Figure 5-5 shows graphically the experimental and theoretical oxidation kinetics, while the discrepancy between the two quantified through the percentage error is tabulated in Table 5-6.

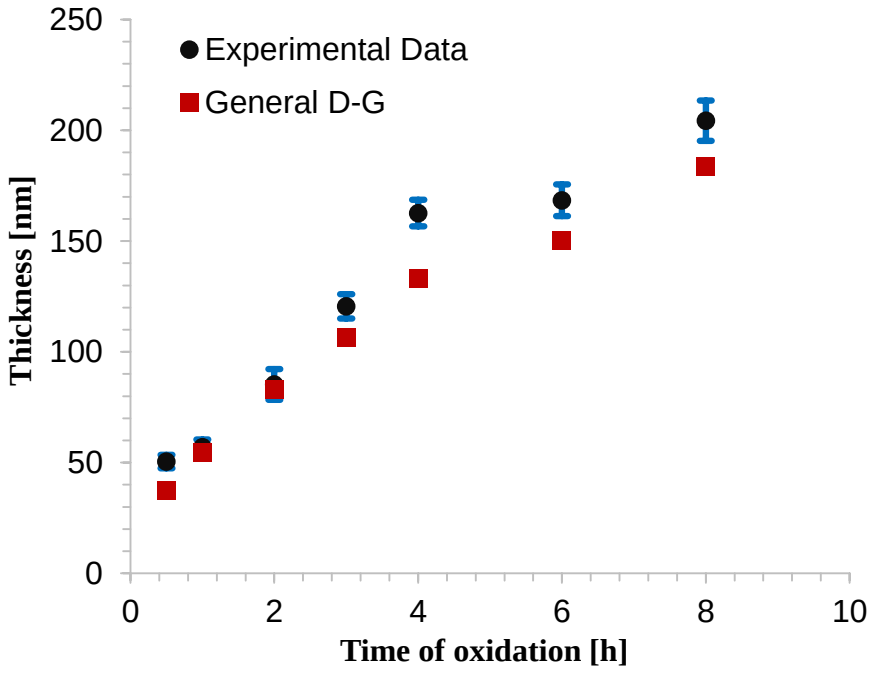

Figure 5-5: Experimental and theoretical oxidation kinetics

It is evident that the theoretical values are smaller than the experimental, with the maximum error reaching 25.4% for the 0.5h oxidation time. The thickness difference occurs due to the thermal cycle of each process in which, oxygen gas was introduced into the chamber from 800^{o}C, namely before the working temperature of 1,100^{o}C was reached. This led to an early start of oxidation process which finally gave greater than expected thicknesses. According to Figure 4-6, the early use of O_2 gas aimed to reach the partial pressure steady state condition before the main oxidation process.

Table 5-6: Experimental, theoretical oxide thickness and their percentage deviation.

Oxidation Time [h]	Average Experimental Thickness [nm]	Theoretical D – G Model Thickness [nm]	$\text{Error} = \frac{\text{Exp} - \text{Theo}}{\text{Exp}} \times 100$ [%]
0.5	50.50	37.7	25.4
1	56.90	54.8	3.6
2	85.23	82.9	2.8
3	120.53	106.6	11.5
4	162.65	132.9	18.3
6	168.43	150.3	10.8
8	204.33	183.7	10.1

5.2.3 XRR Thickness Measurements

Oxide thicknesses were also probed using XRR measurements. Figure 5-6 shows the reflectance spectra for samples oxidized for 0.5, 1, 2 and 3 hours. According to the theory of XRR profile analysis, the period of the oscillations provides information about the thickness of the film. Here it is obvious that the sample oxidized for 0.5h shows the largest period and the sample oxidized for 3h shows the smallest period.

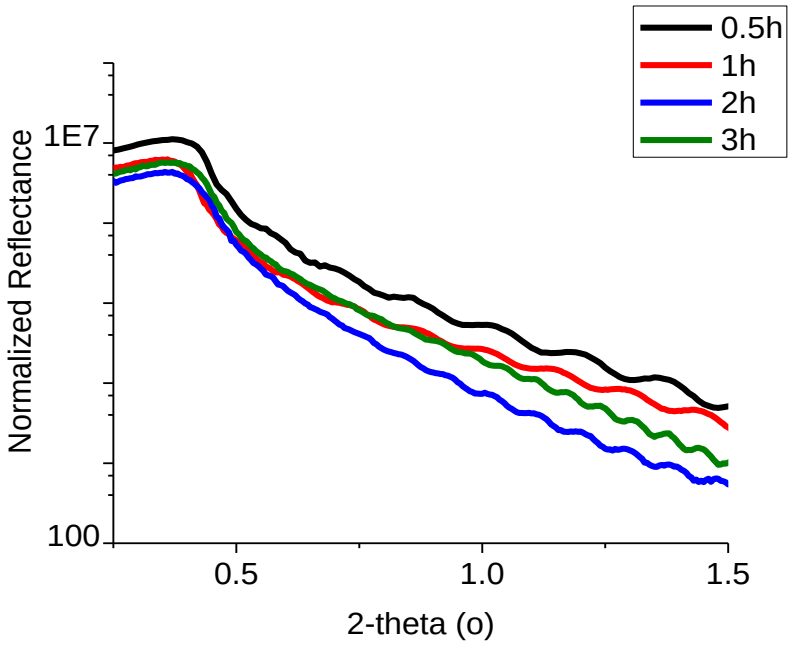

Figure 5-6: XRR profile of samples 0.5h, 1h, 2h and 3h of oxidation

In order to obtain the exact thickness values of the selected samples, the XRR profiles of each sample was fitted, using a Fourier transformation technique, as it is shown in Figure 5-8. The extracted results are plotted against the thickness values given by WLRS technique showing an almost perfect agreement Figure 5-7 with deviations being within 9% for the first 4 group of samples (0.5h, 1h, 2h and 3h of oxidation).

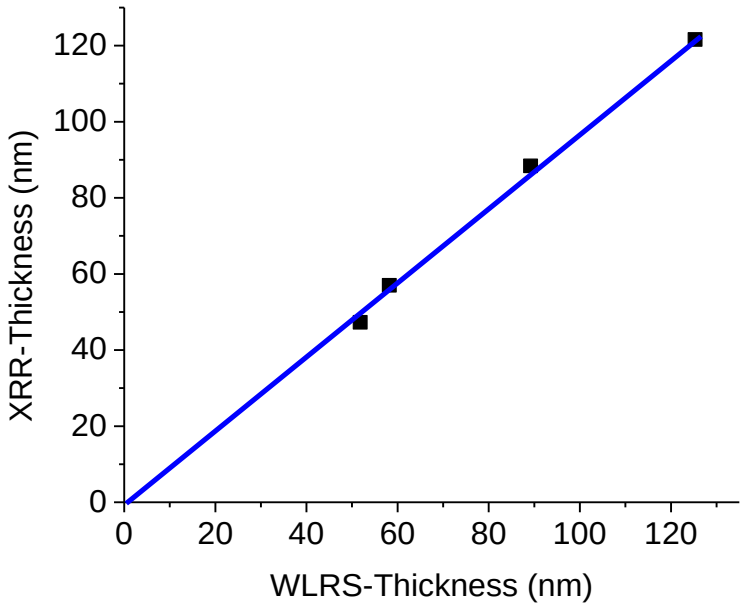

Figure 5-7: XRR vs. WLRS technique for thickness calculation

The minor discrepancies could be attributed to two factors: (a) The imperfect Fourier transformation fitting technique of XRR data provided by Global Fitting Software, and (b) experimental errors during data collection. It should be noted that in XRR technique the thickness is calculated almost over the whole surface area of the sample, while in WLRS technique the thickness is calculated at one point of the surface. The very good correspondence between the measurements confirms the uniformity of the oxide thickness over the whole specimen.

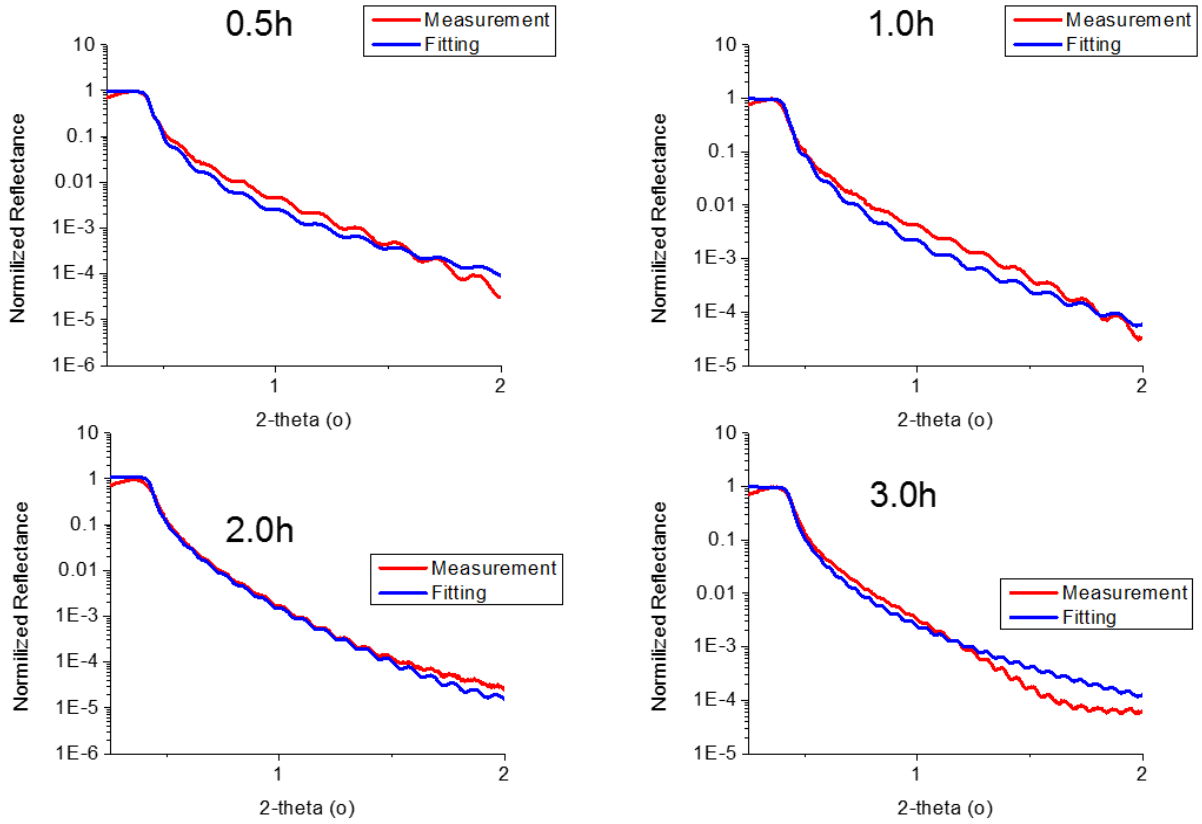

Figure 5-8: Fourier transformation used to fit the XRR profiles of the samples 0.5, 1, 2 and 3 hours of oxidation

Generally the error between the two techniques can be assumed negligible which means that the WLRS technique is a reliable, easy and fast technique for thickness calculation of a multilayer or single–layer film.

5.3 Surface Topography

In order to explain the surface topography images taken by AFM it is important to mention again the theory of oxide growth and their theoretical geometry. The oxidation process consists of 4 steps:

1) Diffusion of the oxygen from gas state to the surface of silicon wafer
2) Adsorption of the oxygen atoms or molecules on the surface
3) Diffusion through the growing oxide to the oxide – silicon interface
4) Reaction of oxygen atoms or molecules with Si atoms

The geometry of one–dimensional planar oxide is shown in Figure 5-9 and the thickness of Si wafer consumed during the oxidation process can be calculated using the below equation:

$$X_{Si} = X_{ox} \times \frac{N_{ox}}{N_{Si}} = 0.46 X_{ox} \quad (5\text{-}6)$$

where X_{si} is the thickness of Si consumed (planar oxidation) [nm], X_{ox} is the thickness of oxide layer [nm], N_{ox} is the molecular density of SiO_2 [= 2.3e22 molecules/cm^3], and N_{Si}: Atomic density of Si [= 5.0e22 atoms/cm^3]. Moreover using the atomic and molecular densities of Si and SiO_2 respectively, can be used in order to determine the volume of SiO_2 films, due to the following equation:

$$\text{Volume of } SiO_2 = 2.16 \times \text{Volume of Si consumed} \quad (5\text{-}7)$$

The above analysis and Figure 5-9 show that the final thin film grows 45% downwards and 54% upwards.

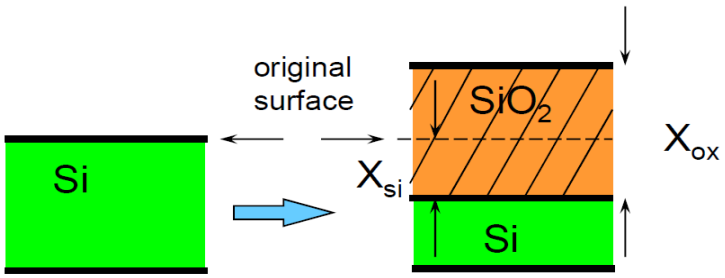

Figure 5-9: Geometry of thermally grown oxide, image adopted from (Sio & Sio 2013.)

Before the analysis of the topography of each sample, it is important to present the Si wafer 2D AFM topography upon which the samples were thermally grown. The surface of Si wafer is very smooth with only 0.148 nm rms roughness, (see Figure 5-10)

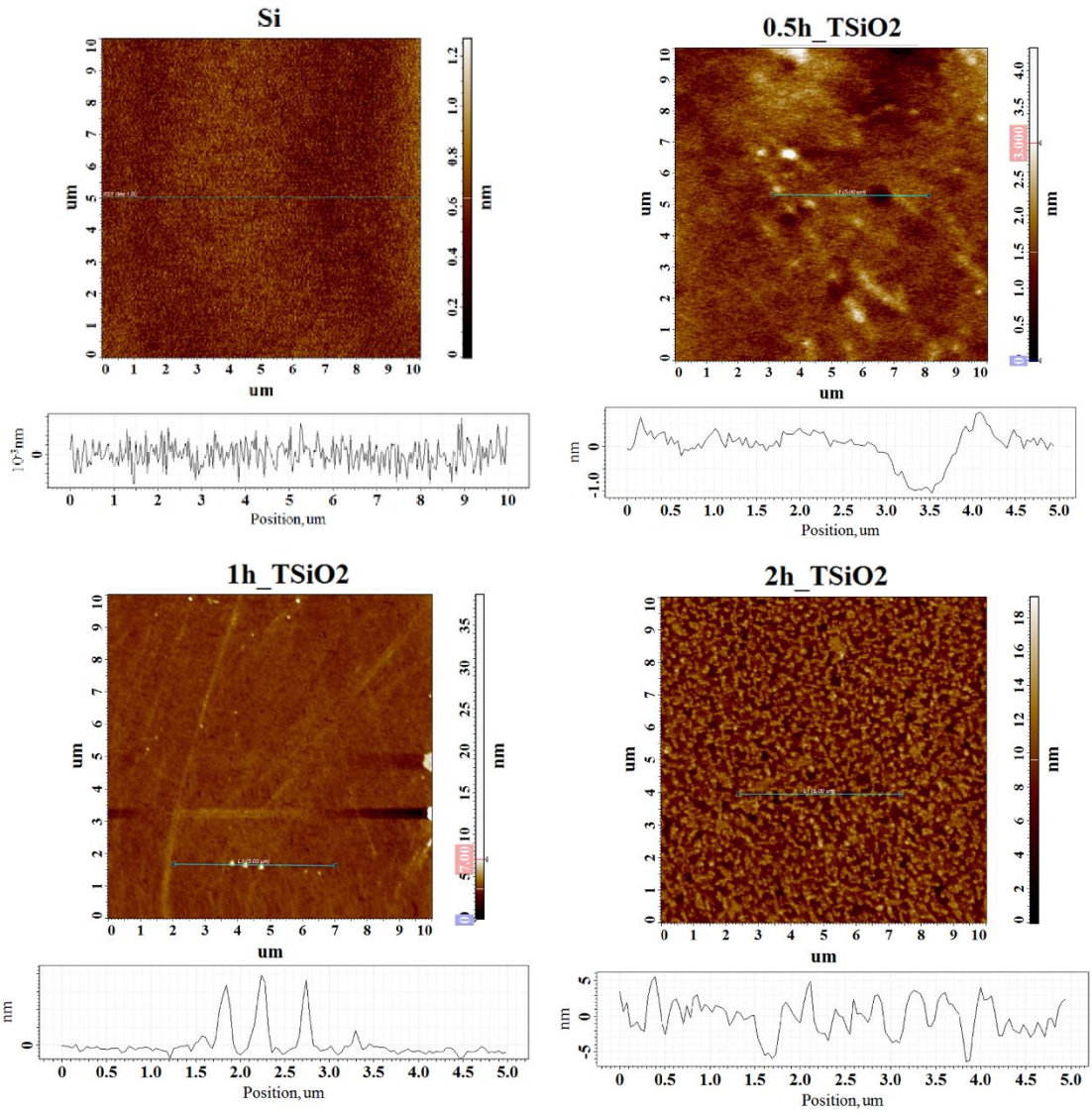

Figure 5-10: AFM images of bulk Si and of 0.5-2h thermally grown oxides

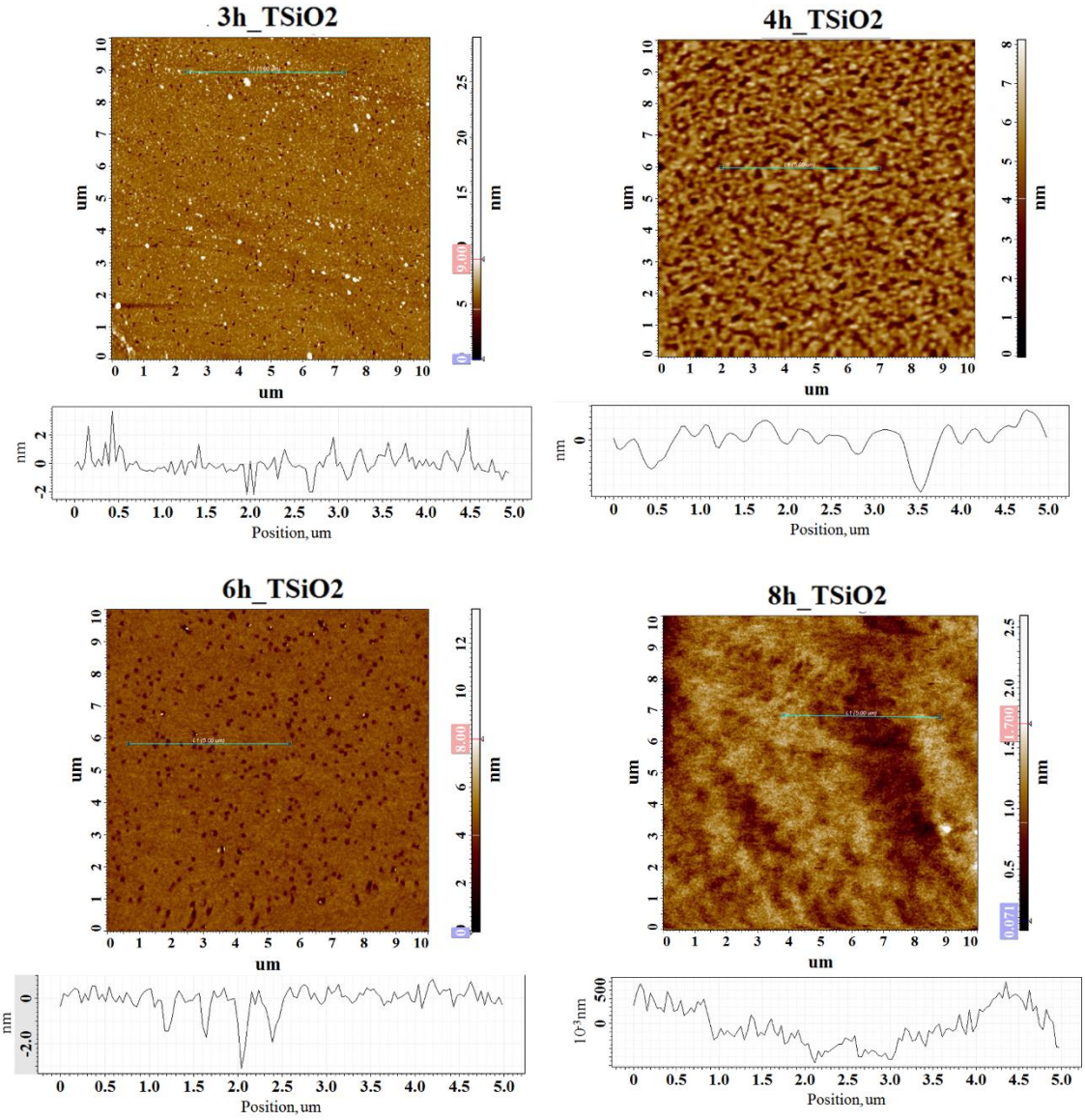

Figure 5-11: AFM images for 3-8h thermally grown oxides

The surface topography and cross section of the samples at relatively small oxidation times (0.5h and 1h) is presented in Figure 5-10. Due to these images it is obvious that the Si wafer topography has been changed due to the presence of SiO_2 structures but both 0.5 and 1 hour of oxidation samples show relatively smooth surface. On the other hand sample of 2h oxidation, shows a surface that consists of pores and sharp peaks of around 5 nm. According to the theoretical geometry (Figure 5-9), the oxide grows both upwards and downward. Since the process is not ideal and contamination factors can be presented during the process some points of the surface can show lower oxidation rates. Thus peaks and pores like in 2h sample can be appeared.

Sample of 3h oxidation (Figure 5-11), shows that pores and sharp peaks are reduced in amplitude over the time, and the surface tend to be relatively smooth again. The sample of 4h oxidation shows a surface that contains peaks and porous which in this case are smoother and have smaller amplitude. On the other hand, the surface of 6h oxidation present a relatively smooth surface that is contains a large amount of randomly distributed pores. Eventually after 8 hours of oxidation the surface starts to create peaks with larger period while the surface roughness remains relatively small. Using NTMDT AFM system, the rms roughness of all the samples is calculated and presented in (Figure 5-12) below. Generally the surface roughness increases until 6h of oxidation, where it starts to fall trying to reach the Si wafer's roughness.

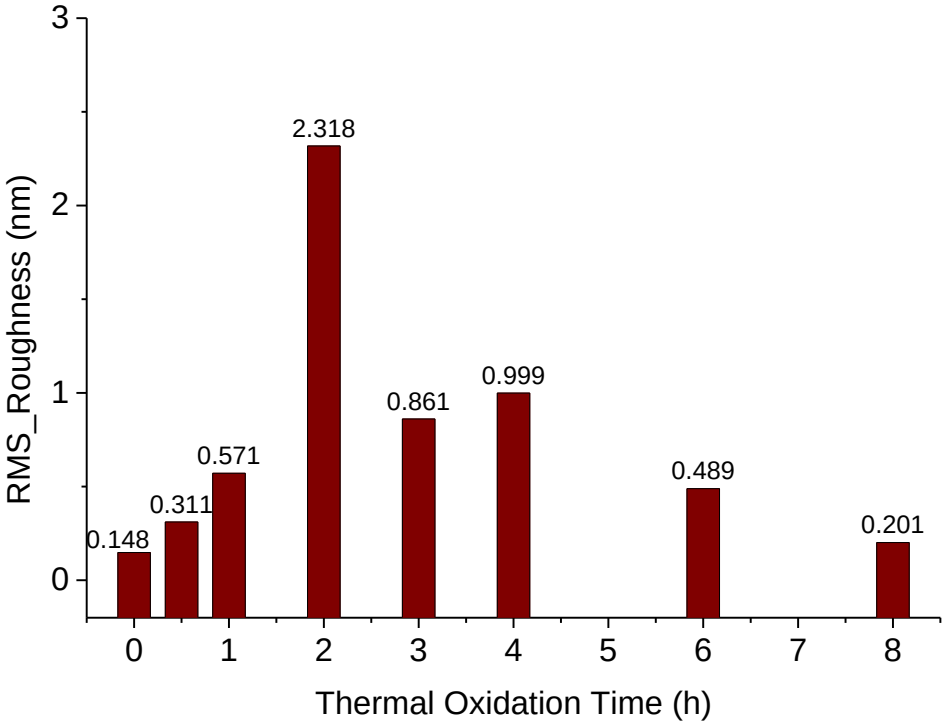

Figure 5-12: Rms roughness of thermally oxidized Si at different exposure times

5.3.1 Density and physical structure of fabricated thin films

The density of the first four samples as it was calculated using XRR technique, is presented in Table 5-7. All values except the 2h, show an excellent agreement with the literature. For instance Brodsky et al, found that the density values of thermally grown silicon oxides ranging between 2.08–2.26 g/cm^3 and according to (Mit.edu 2015; Azom.com 2015) densities near 2.2 g/cm^3 correspond to amorphous silicon dioxide material (a-SiO_2).

Table 5-7: Calculated via XRR density of the fabricated thin films

Oxidation time [h]	Density [g/cm3]
0.5	2.18
1	2.19
2	2.44
3	2.17

As it was mentioned in Section 2.2, amorphous silicon dioxide (a-SiO_2), or fused silica is a glassy material with high working and melting temperatures. According to (Campbell 2008) the physical structure of a-SiO_2 can be thought of as four oxygen atoms sitting at the corners of a triangular polyhedron. In the center of each polyhedron a single silicon atom is covalently bonded to the four oxygen atom, satisfying its valence shell, as it's been shown in Figure 2-3. If each oxygen atom is part of two polyhedral the valence of the oxygen would also be satisfied giving a crystal structure called quartz (c-SiO_2). Consequently combining the literature knowledge and experimental data, this work can state that the thermally grown silicon oxides synthesized in this work, are actually amorphous silicon dioxide (a - SiO_2) thin films.

5.4 Optical Properties

After the completion of synthesis process, important color change have been observed on each set of thermally grown oxides. Specifically each set of samples gain a specific color which differs from set to set, as it is shown in Figure 5-13. In order to explain how each set of samples gain a specific color, and how this color differs for other set of samples, experimental and theoretical analysis must be applied.

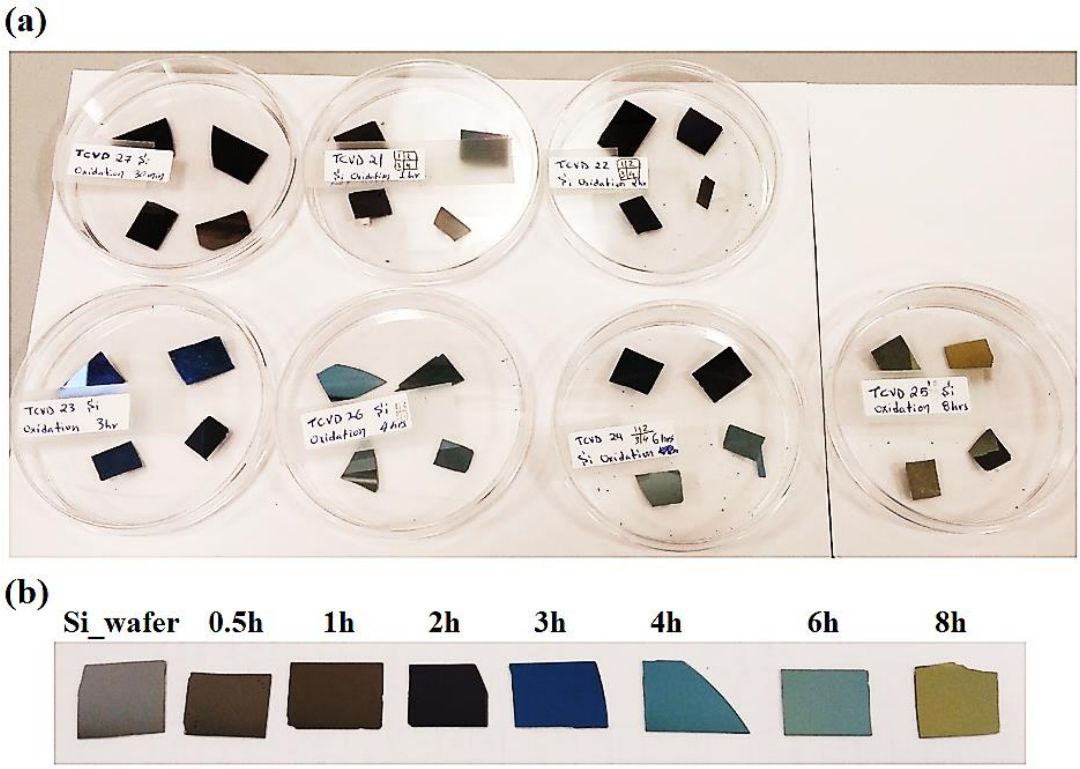

Figure 5-13: (a) Fabricated samples stored in plastic petri dishes, (b) their characteristic color

5.4.1 Reflectance Spectra

As is well known the color of a surface or an object arises from its ability to reflect the light in a specific range of visible wavelength. Therefore the characteristic color of each set of samples can be interpreted using their reflectance spectra. Figure 5-14 shows the reflectance spectra of sample #2 from each fabricated set in the visible wavelength range of 390nm–700nm. Before analyzing the results it's important to mention that all the reflectance spectra were recorded ignoring the scattered reflectance.

According to Figure 5-14, the reflectivity of each sample changes with respect to the reflectivity of the bulk silicon. In the case of 0.5h and 1h there is an overall reduction of

reflectivity, for the samples of 2h and 3h the reflectivity reduces exponentially, for 4h and 6h a maxima at 450 nm of their reflectance spectrum is observed, and finally for 8h maxima at 600 nm and minima at 425 nm of its reflectance spectrum is observed.

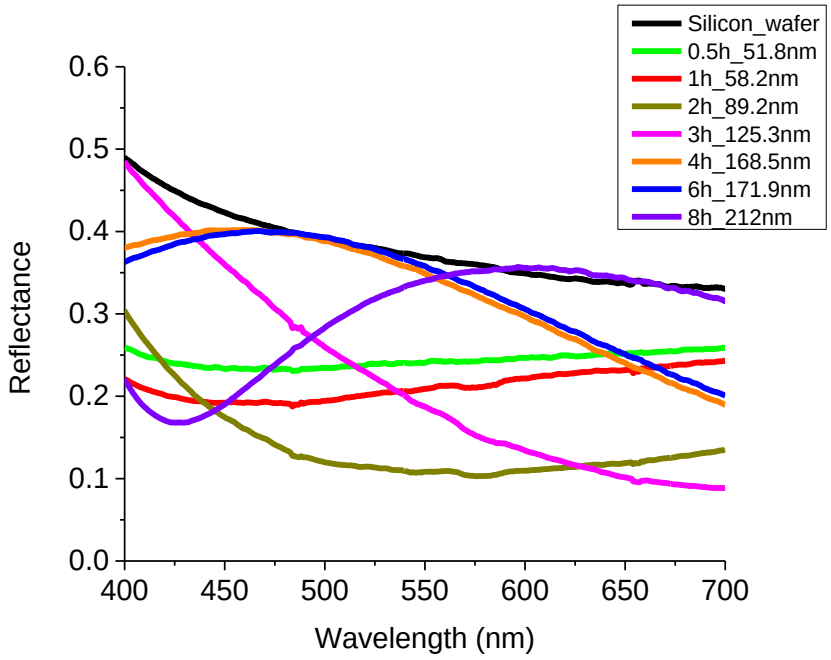

Figure 5-14: Reflectance spectrum of sample # 2 from each set

In order to simplify Figure 5-14 and understand how exactly the reflectance spectrum is correlated with the sample's color, individual graph of the reflectance spectrum of each sample is constructed and presented in Figure 5-15. Each graph contains a color bar of the visible spectrum and the actual color of each sample. The actual color was captured exactly above each sample under fluorescent light.

Using the graphs of Figure 5-15 the specific color of each sample can be easily explained. For example the dark brown color of the TCVD27_0.5h and TCVD21_1h samples is a result of the maximum reflectance in the region of violet and red color of the visible spectrum. The combination of these two colors, together with the relatively low reflectance (< 30 %) gives samples their dark brownish color. With the same way, TCVD22_2h sample dark violet color is due to its maximum reflectivity in the violet range of visible spectrum combined again with the relatively low reflectivity. According to that way of explanation someone could expect that the color of bulk silicon wafer should be violet. It is true that Si has its maximum reflectivity in the violet range of the visible spectrum, however its reflectivity in other wavelengths is

relatively high. Therefore the combination of all the colors with respect to their intensities gives Si its dark silver appearance. In the case of TCVD23_3h sample, the interference of all the wavelengths depending on their intensity confer to the sample its dark blue color. Moreover Figure 5-15 shows clearly the correlation between the sample color and its reflectivity. For instance, TCVD26_4h and TCVD24_6h show a maxima on their reflectance spectrum in the blue range of the visible spectrum. Thus the samples present respectively blue and bright blue colors. Finally sample TCVD25_8h shows a dark yellow color due to the combination of higher reflectivity in the range of 525 nm to 700 nm lower reflectivity in the range of 400 nm to 500 nm. The combination of the visible light colors in the higher reflectivity zone, provide this sample with its dark yellow color.

According to the above experimental analysis a good agreement between the characteristic color and the reflectance spectrum of each sample is shown. However it is not apparent why, and how the reflectivity changes from one set of samples to another. Hence the explanation of this phenomenon is investigated in more depth in the following section.

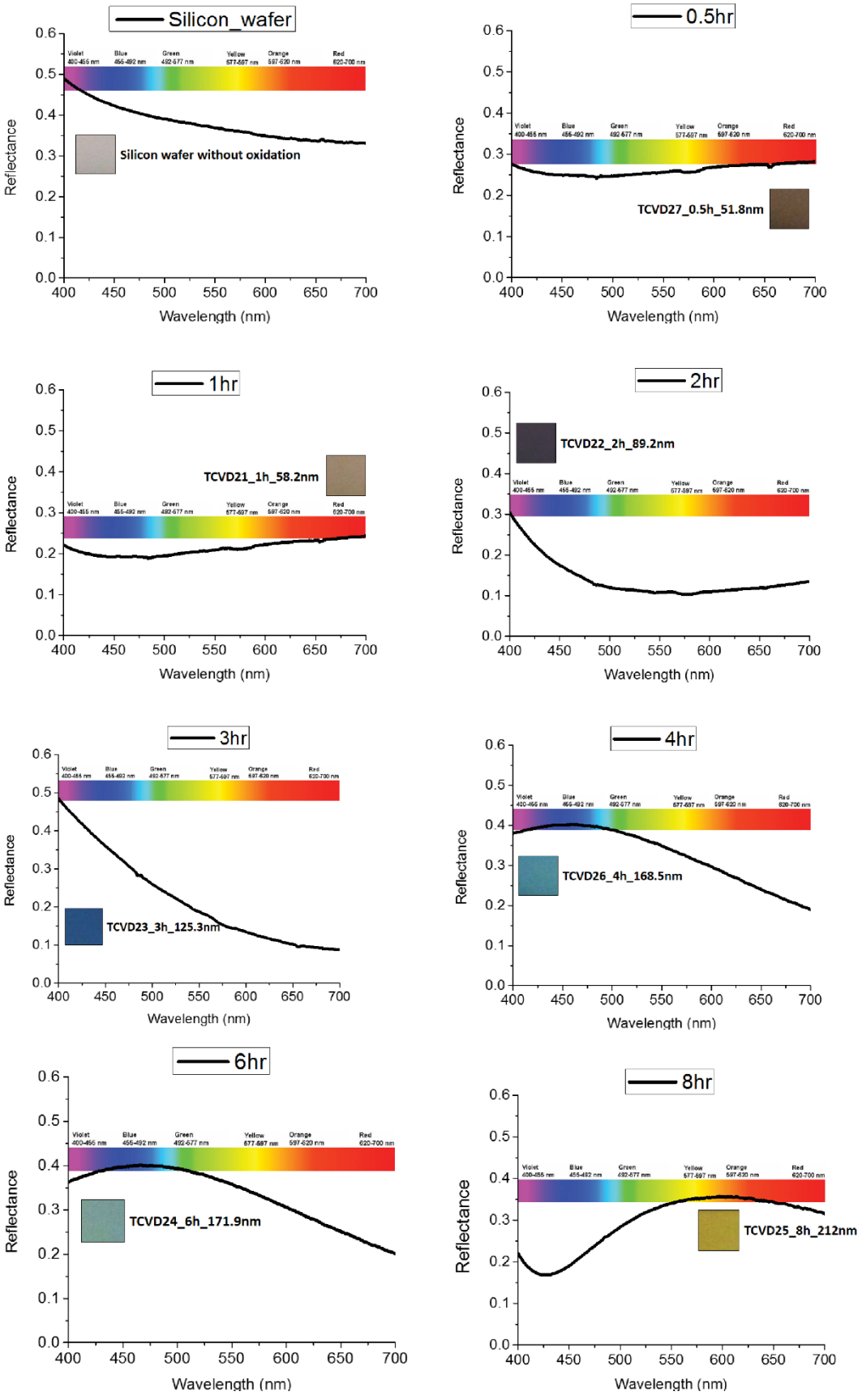

Figure 5-15: Reflectance spectrum of bulk silicon wafer and of 0.5h – 8h thermally grown oxides

5.4.2 Thin Film Interference

Since the thicknesses of the fabricated samples are in the range of nanometers, they can be considered as thin films. Hence in order to understand which parameters control their reflectance spectrum, the physics of light interaction with thin films and their interfaces is studied in this section. When a light 'beam' strikes the interfaces between two media with different indices of refraction it can split into two (Physicscentral.com 2015):

Part of its energy is reflected: If the medium beneath a reflection boundary has a higher index of refraction, namely the light bends more than in the above layer, the reflected ray undergoes a phase shift of (π) or 180^o. On the other hand, in the case of lower refractive indices, the reflection process does not change the wave's phase.

Part is refracted – transmitted: The transmitted wave will bend according to Snell's law and its energy will be lowered since part of it has been already reflected. Propagating through media the transmitted wave will interact with the next interfaces and with the same way, part of it will be reflected and part refracted as shown in Figure 5-16. This process will be repeated until the energy of the wave be will totally eliminated. The overall reflectivity of a thin film therefore is the superposition of multiple reflected 'beams' which cover different optical paths.

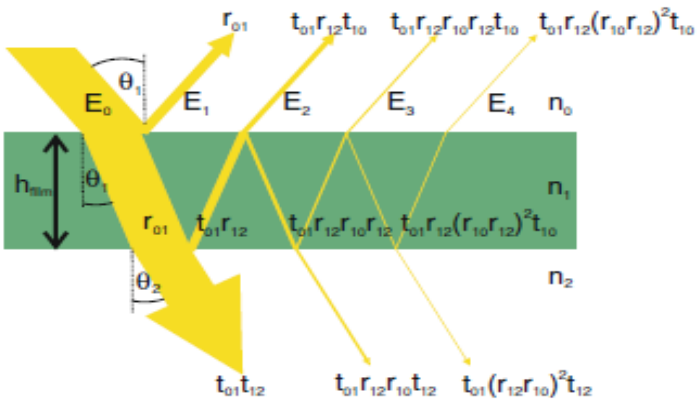

Figure 5-16: Thin film interference, Fresnel equations used to determine the reflection and transmission coefficients of EM waves at each optical interface, image adopted from (Guldin 2013)

The different covered distances of each wave can lead to phase difference among the other waves, (Figure 5-17b). If the overall difference in phase is 0^o, crests and troughs of the waves will be lined up, and the amplitude of the wave will increase due to constructive interference of the waves, (Figure 5-17a). The increase of amplitude will lead to higher reflectance intensity and thus to brighter colors. If the reflected waves have a phase difference of 180^o, then they

will destructively interfere, cancelling each other producing no light reflectance, (Figure 5-17b).

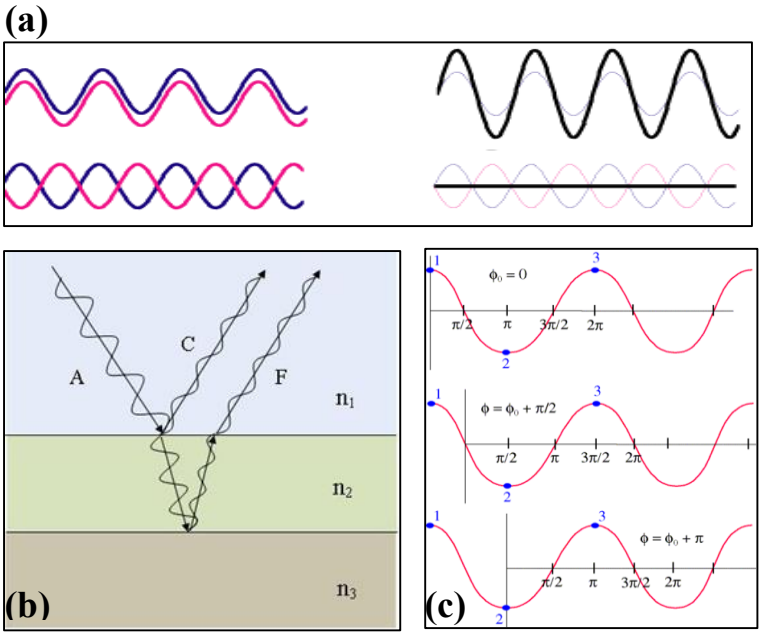

Figure 5-17: (a) Constructive and destructive interference of waves, (b) Light wave reflection and refraction image adopted from (http://c21.phas.ubc.ca/), (c) wave phase difference calculation

Hence the produced color is the product of the interference waves which have different phase shifts. These phase shifts depend on the traveled distance of each wave, which according to (Guldin 2013) is given by:

$$\Delta = 2n_f h\cos\theta_1 \tag{5-8}$$

where Δ is the optical path difference of two adjacent rays [nm], n_f is the refractive index of the thin film, θ_1 is the light incident angle [degrees], and h is the thin film thickness. Consequently the corresponding phase shift of the wave is calculated using Eq. (5-9)

$$\varphi = (m+1)\left(\frac{2\pi}{\lambda}\right)\Delta = (m+1)\left(\frac{2\pi}{\lambda}\right)2n_f h\cos\theta_1 \tag{5-9}$$

where φ is the phase shift, m is the number of total internal reflections, and λ is the wavelength of each wave [nm]. The resulting overall amplitude is then given by a geometric series, which with the contribution of Maxwell equations, Fresnel coefficients and Snell's Law finally produce the equation of reflectivity of a thin film:

$$R = \frac{I_r}{I_o} = \frac{r_{01}^2 + r_{12}^2 + 2r_{01}r_{12}\cos 2\varphi}{1 + r_{01}^2 r_{12}^2 + 2r_{01}r_{12}\cos 2\varphi} \quad (5\text{-}10)$$

Since the source spectrum, source power and light incident angle were constant during the recording of the reflectance spectrum, the only parameters that left to be investigated are the thickness and the refractive index. The study of these two parameters will give the answer to the color change phenomenon.

5.4.3 Reflectance Dependence on Refractive Index

In order to get a clear view of how the refractive index affects the reflectance spectrum, data for a stack of air, silicon dioxide and silicon layers were used. The thicknesses of the air and silicon layers were set to infinite and the thickness of the silicon dioxide layer to a constant value of 100 nm. Then the reflectance spectra for different indices of refraction was plotted in the range of the visible wavelengths and presented in 3 separated groups, as it is shown in Figure 5-18. According to these graphs, the reflectivity changes between 3 groups of refractive indices in different ways:

In the first and second groups, (Figure 5-18a-b) the reflectivity reduces in the range of 425 nm – 700 nm, due to the spontaneous change of the refractive index. The higher refractive index increase the covered optical path difference Eq. (5-8) that lead to higher shift on the phase of the waves, Eq. (5-9). As a result these shifts interfere destructively on the specific wavelengths reducing uniformly the reflectance spectrum.

In the third group the rise of the reflectance spectrum is appeared in the range of 400nm – 525 nm. That means the lights refracts with a way that constructive interference occurred in the range of 400nm – 525 nm and destructive interference in the range of 525nm – 700 nm.

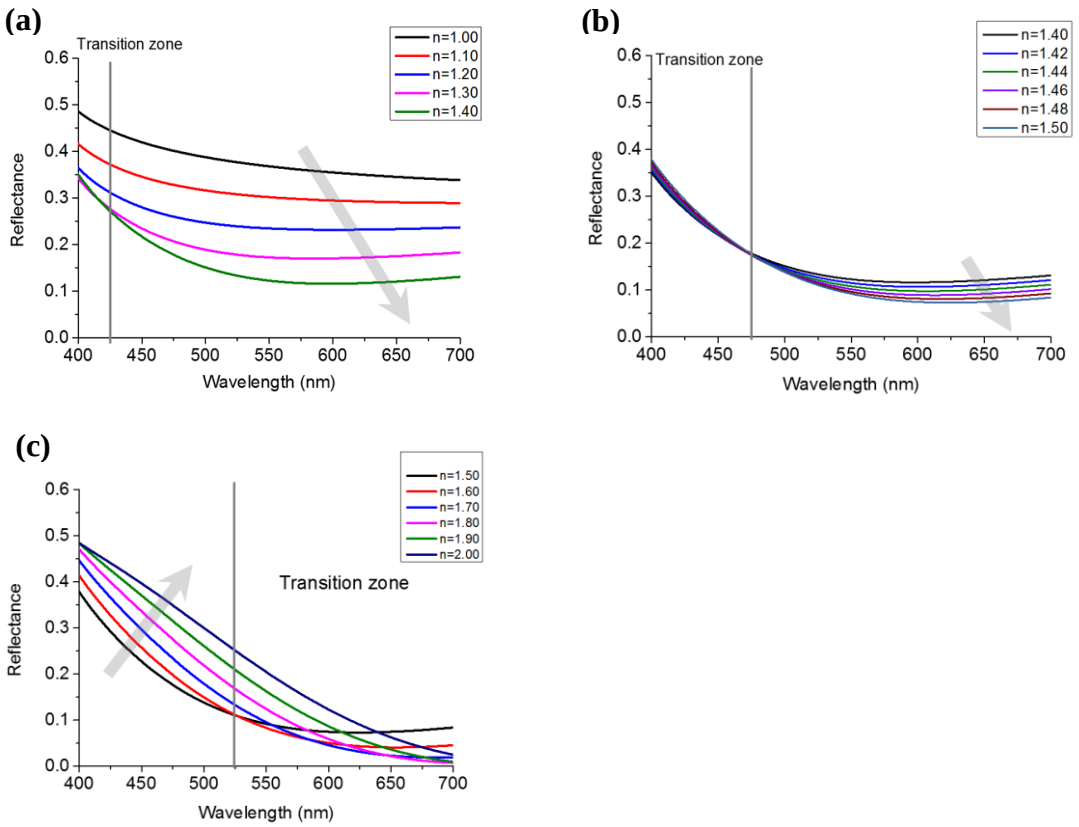

Figure 5-18: Refractive index dependence of the reflectivity. (a) Refractive index values from 1.0–1.40, (b) refractive index values from 1.40–1.50, (c) refractive index values from 1.50–2.0, data adopted from (Filmetrics 2015)

Since the refractive index is a property of the material, it must be constant for the same material. Thus a parametric analysis of refractive index performed in order to define the refractive index of the fabricated thin films.

According to (Filmetrics 2015) for SiO_2 the refractive index at 632.8nm is equal to 1.457. In order to define the refractive index of the fabricated samples, reflectance spectrum from Filmetrics for refractive index 1.457 and different oxide thicknesses were used. Figure 5-19 shows the experimental vs Filmetrics reflectance spectrum of the same oxide thickness samples. All the samples show good correlation meaning that the fabricated samples are really SiO_2 thin films, with refractive index 1.457 at 632.8nm.

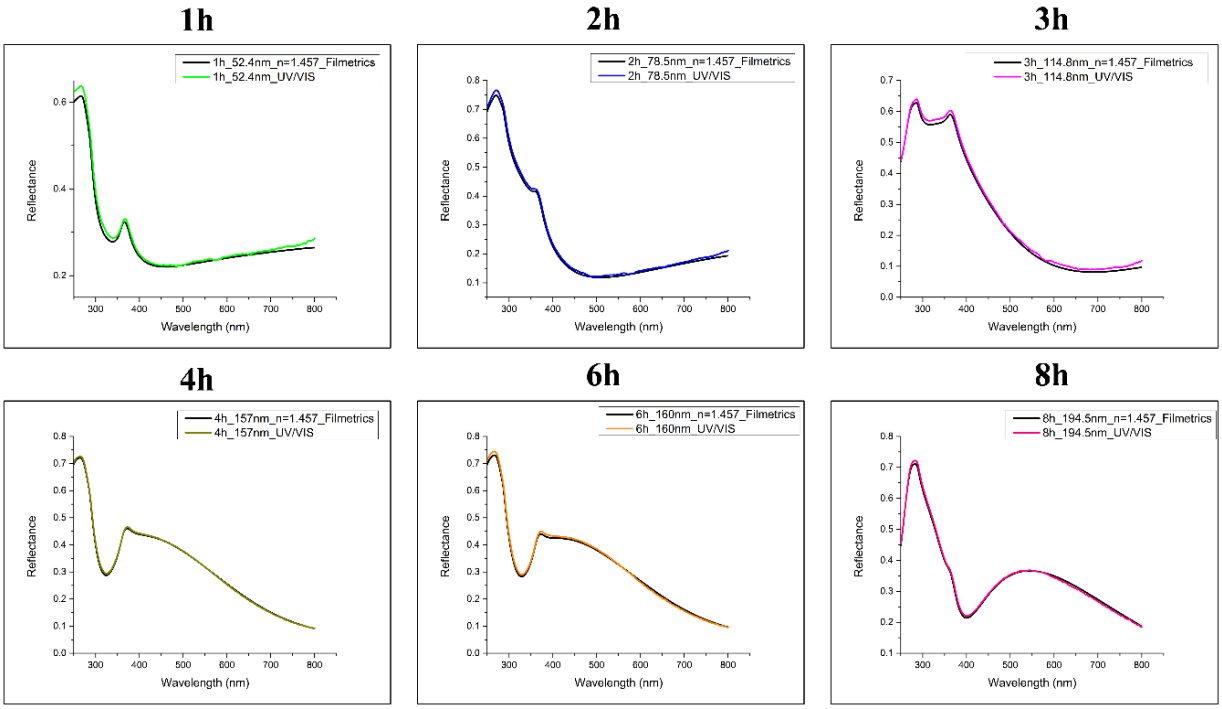

Figure 5-19: Refractive index parametric analysis, Filmetrics data vs Experimental data (UV/VIS)

5.4.4 Reflectance Dependence on Film Thickness

In order to understand how the film thickness affects the reflectance spectrum, data from Filmetrics for different SiO_2 thicknesses was obtained. Figure 5-20 shows the reflectance spectra separated into different groups of oxide thicknesses. The phenomenon of wave constructive and destructive interference can clearly explain the observed behaviors. In the group of 0nm–50nm the destructive interference leads to uniform reflectance reduction, while in the ranges 50nm-110nm and 110nm-170nm both constructive and destructive interferences occur at different wavelengths. The phenomenon of both constructive and destructive interferences is continued with higher intensity in the ranges of 170nm-300nm, 300nm-600nm and 600nm-1000nm. At thicknesses 1-10μm the reflectance spectrum shows oscillations which mean that constructive and destructive interferences occur almost at each wavelength. The combination of the wavelengths with higher intensity finally confer the characteristic color of the sample.

If the layer is very thin, only a uniform reduction of the reflectance spectrum will occur. The color of the thin film will be almost the same as the color of the substrate, only in darker version due to low reflectance intensity.

On the other hand, if the layer is thick constructive and destructive interferences will occur in almost all wavelengths. Thus the color of the thin film is the product of the combined high intensity wavelengths. Shorter period means thicker film and vice versa.

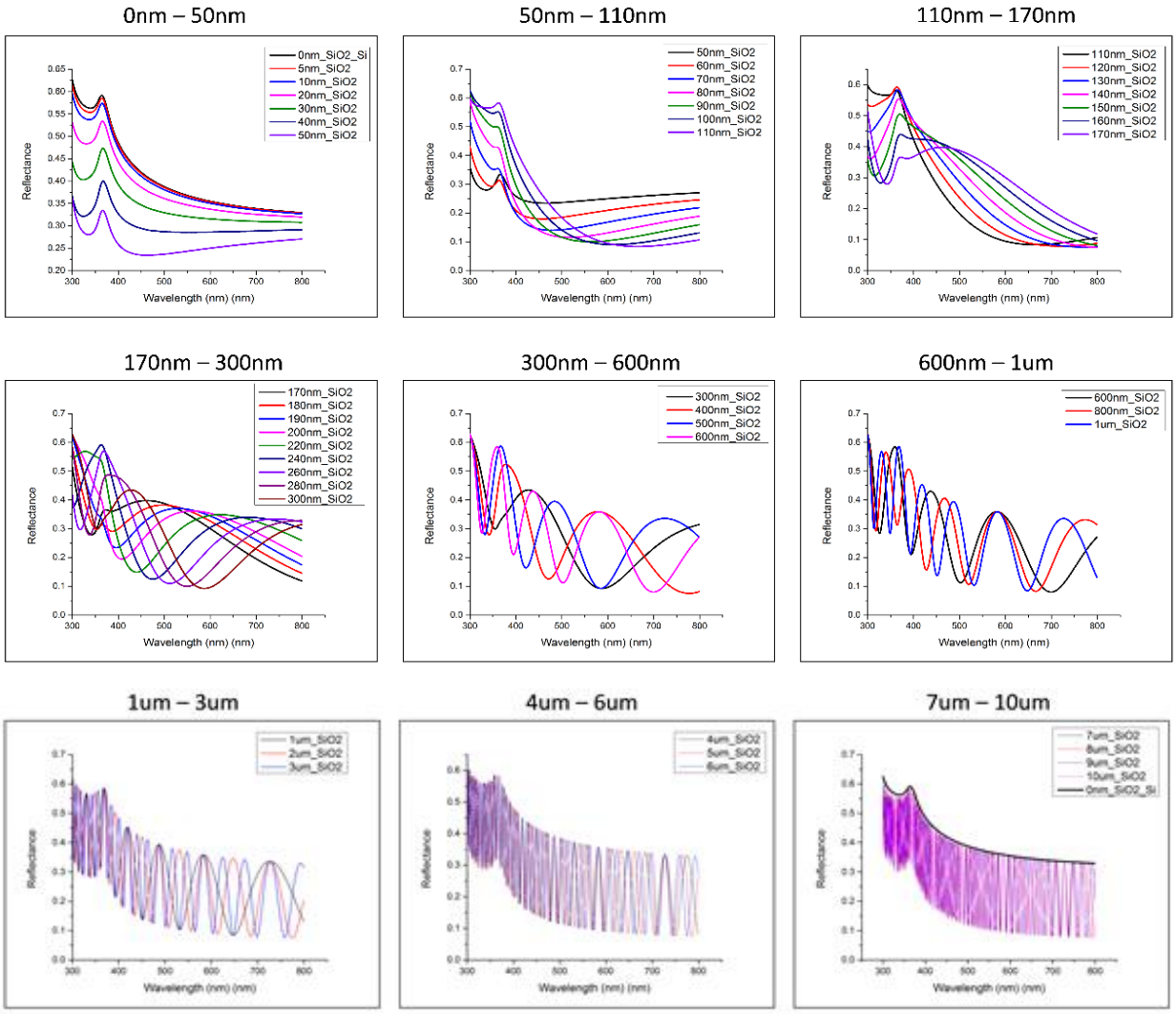

Figure 5-20: Reflectance spectrum of different SiO_2 thicknesses

5.4.5 Calculation of the perceived color of dielectric films on silicon

Considering the theory that was presented above, the prediction of thin film color can be performed if its thickness is known and vice versa. Hence (Henrie et al. 2004), published a work about 'Electronic color charts for dielectric films on silicon'. The main purposes of this work were, to create a color map for engineers allowing them to easily determine the oxide thickness, and to explain the physical parameters and methods for calculating film colors. Using a standard thin film matrix approach the reflectance equation for a single SiO_2 layer on Si substrate was extracted and calculated for various SiO_2 thicknesses. Subsequently the

reflectance spectra were converted to RGB parameters and displayed on a standard computer monitor as shown in (Figure 5-21).

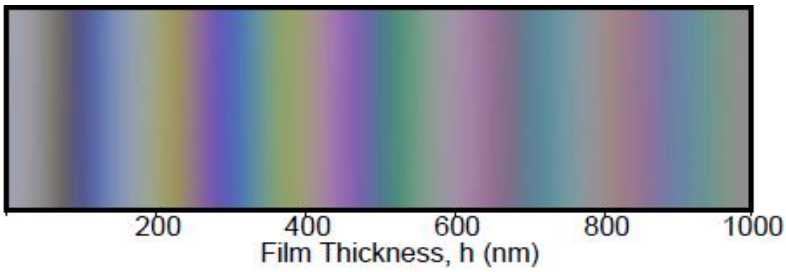

Figure 5-21: Color of a SiO_2 film as a function of film thickness with a source and viewing angle $\theta_i=0^o$, image adopted from, (Henrie et al. 2004)

The conclusion of this work is that the color of the dielectric film on silicon substrate depends on:

- The luminance of the light source
- The incident angle of the light source (θ_i)
- The thickness of the dielectric film (h)
- The dielectric material

With regards to the work of (Henrie et al. 2004) and their electronic color charts for SiO_2 films on Si substrate, the color of the fabricated SiO_2 films is compared in Figure 5-22. This figure establishes that the color correlation and thicknesses of the fabricated samples show a very good agreement with the theoretical color.

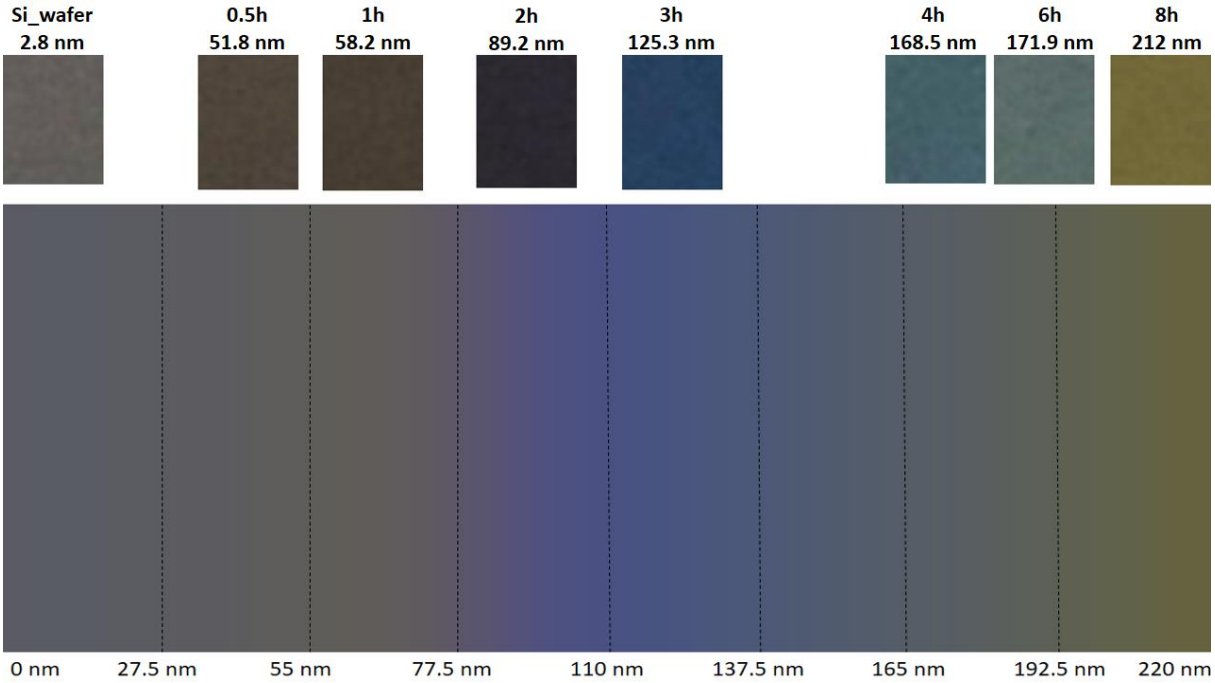

Figure 5-22: Color comparison between (top) thermally grown SiO_2 of this work, and (bottom) electronic color chart for SiO_2 films on silicon, image adopted from (Cleanroom.byu.edu 2015)

5.5 Chapter Summary

Silicon oxides of various thicknesses have been grown using dry thermal oxidation of crystalline silicon wafers [100] using a T-CVD device at 1,100°C. The oxide thicknesses were measured using WLRS and confirmed using XRR measurements. The density of the oxide products as measured through the critical angle for total X-ray reflectance (XRR measurements) confirmed their amorphous and uniform nature irrespective of time of oxidation. The oxidation kinetics appears to be in excellent agreement with the theoretical D-G model which can serve as a predictive tool. Surface oxidation of silicon increases in part the surface roughness of the material shifting it into the nanometer regime and significantly changes its reflectance characteristics with implications on the visible color of the specimens. This can be used as a visual tool for indirect oxide thickness monitoring on microelectronic or other processes.

PART B: PLASMA PROCESSING OF SILICON AND PDMS

CHAPTER 6 INTRODUCTORY REMARKS: POLYDIMETHYLSILOXANE (PDMS) AND PLASMA PROCESSING

6.1 Chapter Outline

This chapter provides an introduction to the material system under investigation and the relevant processing methodology that will be used in this part of the thesis. The major physical, chemical, structural, thermal, optical and mechanical characteristics of PDMS are presented together with methods of synthesis and most notable applications. Moreover, the plasma processing technique is presented and relevant literature results on the plasma processing of hard and soft materials are reviewed.

6.2 Polydimethylsiloxane (PDMS)

This part of the thesis aims in investigating the influence of plasma processing on hard and soft materials. The hard materials that will be investigated relate to the material systems already introduced in Part A: silicon and silicon dioxide. On the soft matter end, a silicon-based polymer, the polydimethylsiloxane (PDMS) is used and it will be introduced in this chapter. PDMS belongs to a group of polymeric organosilicon (C-Si bonds) compounds that are commonly referred to as silicones. It is the most widely used silicon-based organic polymer and is particularly known for its unusual rheological properties (Schneider et al. 2009).

6.2.1 PDMS Characteristics

The chemical formula of PDMS is described by Eq. (6-1), where *n* is the number of repeating monomer units (in bold):

$$CH_3 - [\mathbf{Si(CH_3)_2O}]_{\mathbf{n}} - Si(CH_3)_3 \qquad (6\text{-}1)$$

The industrial synthesis which produces liquid PDMS begins from dimethyldichlorosilane – an organosilicon compound with chemical formula $Si(CH_3)_2Cl_2$ and at room temperature is a colorless liquid – and water by the following chemical reaction:

$$n\mathrm{Si(CH_3)_2Cl_2} + n + \mathrm{H_2O} \rightarrow \mathrm{HO[-Si(CH_3)_2O-]_nH} + 2n\mathrm{HCl} \qquad (6\text{-}2)$$

Since the reaction produces liquid PDMS, a cross-linking process is required to generate a solid form of PDMS, which is basically the final product that is used in various applications. The PDMS and cross linker discussed over this part of the thesis are commercial products that have been purchased from Dow Corning Corporation, which uses Sylgard 184 silicone elastomer (PDMS) and SiH silicone elastomer curing agent as cross linker (Figure 6-1).

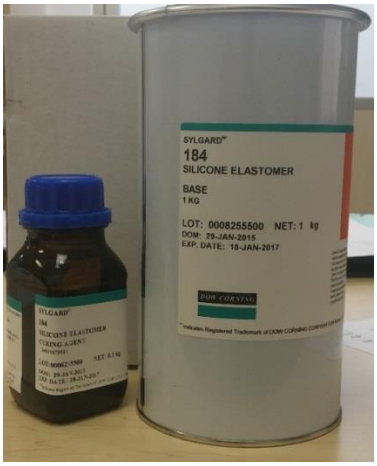

Figure 6-1: Cross linker (left) and liquid PDMS elastomer (right)

After cross linking PDMS becomes hydrophobic with water static contact angles that vary from 90º-120º (Jin et al. 2005). The Young's Modulus of PDMS is 1.76MPa but depends on the elastomer to cross-linker ratio and optical properties refractive index 1.4295 at wavelength 635nm of cross-linked PMDS (Schneider et al. 2009). Its mass density 0.97 g/m^3, thermal conductivity 0.15 W/mK and electrical resistivity 4x10^{13} Ωm are reported in (Mit.edu 2016). The most notable properties of cross linked PDMS are summarized in Table 6-1.

Table 6-1: Most notable properties of cross linked PDMS, Sylgard 184

Characteristics	Property	Value/Comment
General	Density [g/cm^3]	0.965
	Structure	Cross linked polymeric chains
Wetting properties	Hydrophobicity, Static Contact Angles	90º-120º
Thermal	Thermal Conductivity [W/m-K]	0.15
Mechanical	Young's Modulus [MPa]	1.76
Electrical	Electrical Resistivity [Ω-m]	4x10^{13}
Optical	Appearance	Colorless
	Refractive Index	1.4295 at 635nm

6.2.2 PDMS Applications

PDMS has been applied to a variety of applications ranging from contact lenses and medical devices to shampoos, food (antifoaming agent), lubricants and heat-resistant tiles. Due to its good rheological characteristics, liquid PDMS can be casted in various geometries replicating surface characteristics of the mold. PDMS can, therefore, be used in microfluidic applications (McDonald & Whitesides 2002) and superhydrophobic surface generation (Yoon et al. 2008) or superhydrophilic surfaces (Lee & Yang 2012). Additionally, due to its ability to transform from liquid to solid, PDMS can be used as a matrix in nanocomposite materials (Julia et al. 2003), (Nikolaou et al. 2015). Some of the mentioned applications are shown in Figure 6-2.

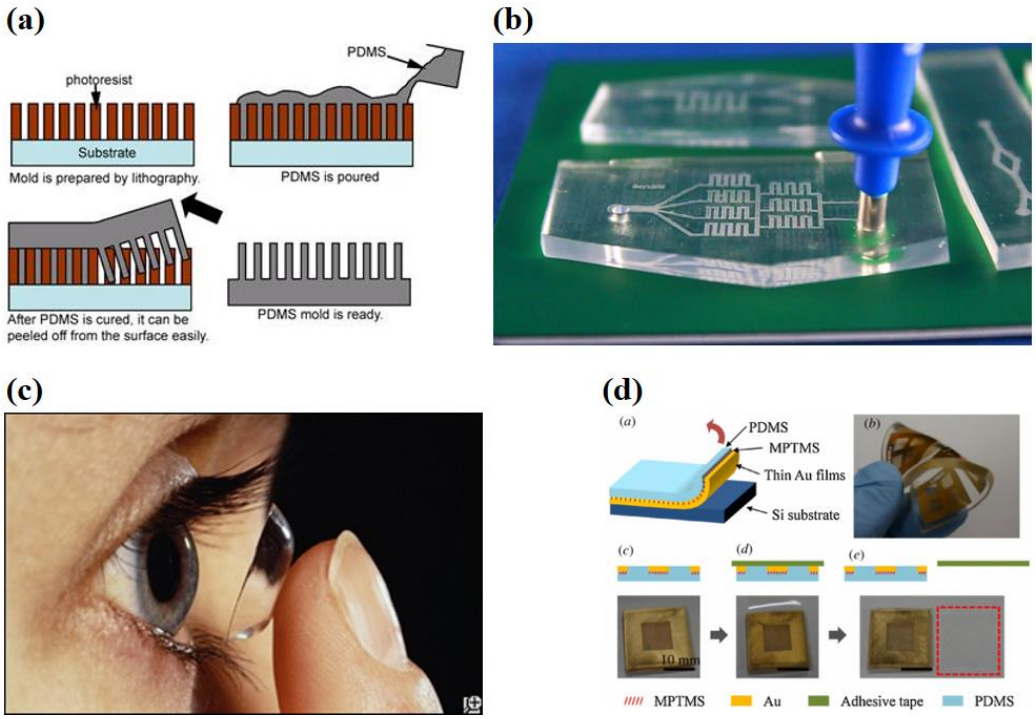

Figure 6-2: Some of PDMS applications, (a) PDMS surface patterning, (Bumems.ee.boun.edu.tr 2016), (b) PDMS usage in microfluidic devices, (Chemistry.beloit.edu 2016), (c) main material in contact lenses, (Thaimedicalnews.com 2016), and (d) PDMS used as a capping material in a flexible device, (Byun et al. 2013)

6.3 Plasma Processing

Plasma processing is a plasma–based technology that aims at modifying the chemical and physical properties of a materials surface. Low pressure plasmas, non-equilibrium plasmas and glow discharge processes are the main techniques for microfabrication processes such as sputtering, thin film deposition, dry cleaning and plasma etching. Thereby this section is focused on plasma physics and its most notable industrial applications, knowledge basically acquired from (Eliezer 1989; Love 2003, Rack 2015). Additionally, the literature on plasma processing of hard and soft silicon-based materials is reported.

6.3.1 Plasma Physics

Plasma is frequently referred as the fourth state of matter beyond the well-known solid, liquid and gas fundamental states. Plasma is a partially ionized gas composed of atoms/molecules, ions, electrons, photons and neutral species all presented in various states and conditions.

Plasma generation methods

Plasma in general can be generated by two ways of gas processing: (1) heating a gas at very high temperatures and (2) exposing a gas to a strong electromagnetic field. In the first process gas species receive a huge amount of thermal energy which causes them to vibrate and move at high velocities. This movements cause collisions that produce ions which together with electrons, photons and neutral gas atoms and molecules give the plasma state. In the second process Direct Power (DC) or radio frequency power (RF) are usually the most famous techniques used as external energy sources. In DC a gas source is located between two electrodes which receive large voltage that causes any free electrons to rapidly accelerate towards the anode. In their path, electrons collide with slow-moving gas molecules and atoms, causing their ionization. Newly produced electrons continue to accelerate towards the anode and the process cascades. Therefore the gas rapidly becomes filled with positive and negative particles and the steady state condition gives the plasma state of matter. On the other hand RF external energy source basically transfer energy to electrons through high frequencies (typically 13.56MHz). This frequency affects only the free electrons giving them a high mobility, which leads to multiple collisions with gas molecules and finally create the plasma state.

An RF based plasma generation is called inductively coupled plasma (ICP). ICP is becoming one of the most important types of plasma reactors used in semiconductor processing and

surface modification. A typical ICP reactor consists of a vacuum chamber, pumping unit, gas feeding system and gas controllers, pressure gage, an RF power supply and a power transfer device (Figure 6-3). The major advantages of this type of generator are that no internal electrodes are needed, the plasma is easily sustained at a low pressure and plasma has high ionization efficiencies. A radio frequency inductively coupled plasma (RF-ICP) is used in this research to modify hard and soft substrates. The RF-ICP generation system will be discussed in detail in the following chapter.

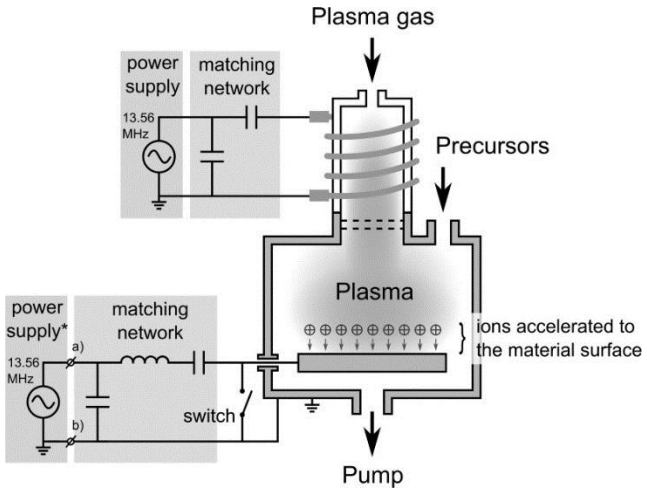

Figure 6-3: A typical Inductively Coupled Plasma (ICP) generator, image adopted from (Esl.ecsdl.org 2016)

Plasma characteristics

Although plasma is closely related to the gas phase it differs in a number of ways including the following: (1) plasma has a very high to infinite electrical conductivity while the electrical conductivity of a gas is very low, for instance air is an excellent insulator, (2) in plasma electrons, ions, protons and neutrons act independently while in gas state all particles behave in a similar way (3) in plasma state the particles can interact at long ranges through the electric and magnetic forces while in gas state two particle collisions may happen but in general body collisions are extremely rare, finally (4) plasma has a characteristic color which depends on the gas being used for its generation, while of course the gas phase is colorless.

Industrial applications of plasma

The unusual properties of plasma such as high temperatures, energetic electrons and ions and the existence of plasmas in a very broad range of pressures and temperatures can provide a wide range of high technological applications. Some of the most notable applications (Figure

6-4) are: plasma welding, cutting and processing, plasma space propulsion, plasma display panels, plasma material synthesis (PECVD) and plasma surface modification.

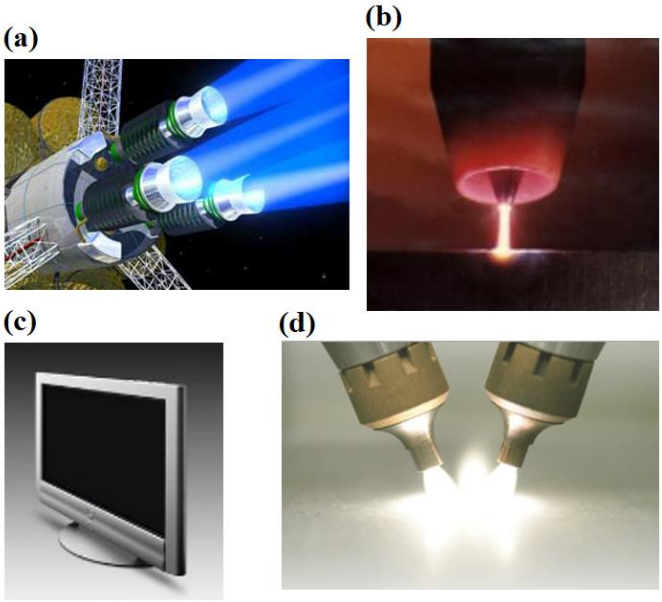

Figure 6-4: Plasma applications, (a) plasma space propulsion, (Pro-fusiononline.com 2016), (b) plasma welding, (Images.dailytech.com 2016), (c) plasma display panel and (d) plasma surface modification, (Dsftm.cnr.it 2016)

In recent years, plasma surface modification aroused to a very high level. Precise surface etching, patterning (see the world's smallest coin in Figure 6-5a) and chemical modification are nowadays achievable, and high technological applications such as superhydrophobic surfaces can be produced (see Figure 6-5b). The work presented in this part of the thesis will focus on plasma processing technique.

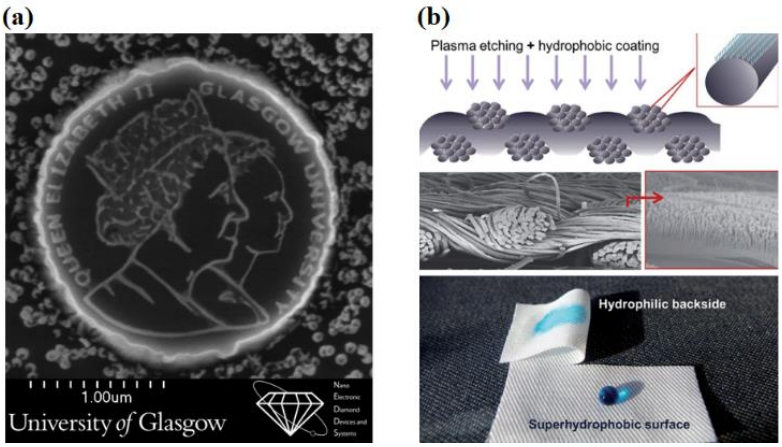

Figure 6-5: (a) World's smallest coin created by multiple plasma-masking etching, (Oxford-instruments.com 2016) and (b) superhydrophobic surface after plasma etching and hydrophobization techniques, (Kwon et al. 2014)

6.3.2 Plasma surface modification

As a solid surface undergoes plasma exposure, plasma species attack the surface chemically or physically dividing the process to respectively reactive and non-reactive plasma processing. A non-reactive plasma is created by noble gases such as Argon (Ar), Helium (He), Neon (Ne), Xenon (Xe), etc. which have extremely low reactivity with other substances. Non-reactive plasma processing lead to two main surface phenomena: (1) physical etching and (2) ion implantation–modification. Both processes are depended on the material that is exposed to the non-reactive plasma processing. Physical etching generally occurs at hard materials and can be paralleled to sand blasting technique, only instead of sand particles, positive ions (plasma) 'bombard' and remove material from the surface (Donnelly & Kornblit 2013). On the other hand, if the surface is relatively smooth (in the case of polymers), the accelerated ions can penetrate through the material or just collide creating permanent deformation of its morphology (Shirtcliffe et al. 2011).

Reactive plasma is created when high affinity gases are used, such as oxygen (O_2), nitrogen (N_2), hydrogen (H_2), tetrafluoromethane (CF_4) and many more. As stated earlier, plasma basically consists of ions, electrons and free radicals. In general ions are used for physical etching, while the free radicals are used for dry chemical etching (Probe et al. 2015). Free radicals are atoms or molecules that have at least one unpaired electron and thereby they are unstable and highly reactive. It is the free radicals that react with the surface creating volatile particles that are released from the surface. Free radicals are formed by particle collisions within the plasma and once produced they diffuse towards the exposed surface where they adsorb and chemically react. The byproducts of this reaction desorbed from the surface and diffuse back to the plasma. A reactive plasma processing is generally the well-known reactive ion etching (RIE) technique, since the exposed surface is going through etching and chemical modification. The RIE of silicon is described very well by (Jansen et al. 1996). To conclude, Figure 6-6 shows the transition zones of reactive and non-reactive plasma etching processes (both cases use a reactive gas source). It is important to note that although a reactive gas is used, only physical or combined physical and chemical etching can occur when the parameters of pressure and RF power are properly adjusted.

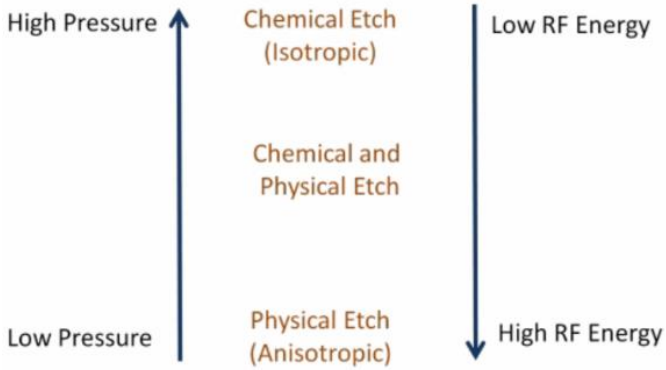

Figure 6-6: Transition zones of reactive and non-reactive plasma etching processes (in both cases a reactive gas is used)

To conclude, in order to utilize the recently installed equipment at RUNMS synthesis laboratory, this work will exploit the available Argon gas for plasma processing technique. In fact, this part of the thesis will focus on Argon Ion Bombardment of hard and soft surfaces. The next two sections present the relevant information available in the literature.

6.3.3 Si/SiO_2 exposure to Argon Ion Bombardment (AIB) – Literature Review

When a hard material is exposed to AIB, physical etching occurrs and material is removal in the process. Comfort et al. 1987 studied a low-energy AIB technique in order to remove native oxide from Si wafer and synthesize a high quality epitaxial silicon. In order to achieve this goal they investigated the silicon dioxide and silicon etching rates with respect to plasma power, substrate bias (voltage), gas pressure and substrate temperatures. For the case of SiO_2 material they discovered that the etching rates increase with increased plasma power, gas pressure, and magnitude of substrate bias. The strongest dependence was found to be on substrate bias with weaker dependence on plasma power and pressure. Moreover SiO_2 etching rates was nearly doubled when the substrate temperature was increased from 600 to 800^{o}C. These results show a strong dependence of the sputtering process on temperature. Based on ion energies of 100eV, fluxes $5x10^{13}cm^{-2}s^{-1}$, very low pressures and temperatures varied from 600^{o}C-800^{o}C the general reported oxide etching rates varied from 0.4-2.5nm/min while for pure silicon the etching rates were lower and varied within 0.3-0.7nm/min. The rates for Si were again a strong function of applied bias but only a weak function of applied power.

Hu et al. 1991 investigated the AIB of SiO_2 on crystalline silicon (c-Si) substrates at energies from 300 to 1200eV. Results showed that AIB causes etching rates of 10-15 nm/min. Moreover the AIB causes significant damage to the underlying c-Si surface. Todorov & Fossum 1988

investigated the AIB of SiO_2 at relatively low energies of 40-100eV. The results showed that at energies less than 50eV no sputtering occurred. Moreover the oxide removal at a constant 60eV energy and different ion doses was studied. The results showed a linear and strong dependence of etching rate to ion doses.

6.3.4 PDMS exposure to Argon Ion Bombardment (AIB) – Literature Review

Although argon ion bombardment (AIB) has been studied since 1987, the AIB of soft-polymer materials has been the subject of more recent investigations. In fact AIB of poly-dimethylsiloxane (PDMS) surfaces is only mentioned in a few recent publications.

(M. A. C. Aguila 2010) used a direct current magnetron argon plasma to examine the effects of plasma exposure on the surface of PDMS. Contact angle (CA) and FTIR spectroscopy measurements showed that the plasma treatment led to significant hydrophilicity on the PDMS. However hydrophobic recovery of PDMS surface during the first few hours after plasma treatment was also observed. The changes of wetting properties during and after the plasma processing are related with surface chemistry modification.

Work done by (Malecha et al. 2010a) showed again that the PDMS passes through hydrophilic and hydrophobic recovery stages. In this work argon microwave plasma treatment of PDMS was used. X-ray photoelectron spectroscopy (XPS) showed that after plasma treatment the surface content of carbon reduced while the content of oxygen and silicon increased. Thus the hydrophilicity of PDMS appeared due to the presence of polar groups on the surface. Additionally this work reported that the hydrophobic recovery of PDMS is due to the migration of polar groups of low molecular weight from the surface to the bulk of the material, reducing at the same time the surface energy. However the work reported that the recovered hydrophobic properties of PDMS were different than the unexposed PDMS. The work assumed that this phenomenon is because of the permanent changes in surface microstructure.

6.4 Chapter Summary

In this chapter PDMS is presented together with its properties, and most notable applications. Additionally a new technique, plasma processing is deeply investigated. Plasma physics, generation methods, properties and most popular applications are summarized together with plasma surface modification method. A literature review on non-reactive plasma processing specifically on argon ion bombardment of Si, SiO_2, and PDMS showed that this technique

exhibited promising results on surface modification. The motivation for each material system is summarized below:

- **AIB of Si and SiO_2:** Plasma processing of hard materials has shown that the surface undergoes a physical etching process, which is strongly depended to various parameters. Therefore our goal is firstly to determine the etching rates of the Inductively Coupled Plasma (ICP) 'Ion beam source' of the Hybrid Deposition System (HDS) of RUNMS synthesis lab and secondly to investigate the topography of the exposed surfaces in order to determine the quality of the etching.
- **AIB of PDMS:** Generally the largest amount of work is focused on reactive plasma processing, thus we wanted to study the exposure of soft surfaces like PDMS to a non-reactive plasma processing, specifically to AIB. The literature review showed that the AIB of PDMS changes its chemistry and its wetting properties. However the literature do not investigate what is happening with topography and optical properties of the exposed PDMS surfaces. Therefore our goal is to investigate the changes of wetting properties, topography and optical properties of the exposed PDMS surfaces.

CHAPTER 7 EXPERIMENTAL INVESTIGATION OF PLASMA PROCESSING: MATERIALS AND METHODS

7.1 Chapter Outline

The materials and methods used for experimentally investigating the effect of plasma processing on hard and soft surfaces are described in this chapter. More precisely, material synthesis methodology for depositing PDMS films and the subsequent optical, morphological and wetting characterization processes, such as uv-vis transmittance spectroscopy, contact angle, WLRS and AFM are presented.

7.2 Materials and Methods

7.2.1 Si and Silicon Dioxide Films

Plasma has been used as means to process the surfaces of hard and soft materials within this part of the thesis. Considering hard surfaces, single crystal silicon wafers, purchased from (Microchemicals.com 2016), have been used. Furthermore, thermally grown thin films of SiO_2 (see Section 4.2.2) have also been included in the investigation. It was decided to use thicknesses around 100nm, thus the thermal oxidation was performed for 3hrs at 1,100°C giving thicknesses of 107±0.7 nm.

7.2.2 PDMS Film Synthesis

PDMS was purchased from Dow Corning in two separate parts, Sylgard 184 base and its cross-linker. The deposition process of PDMS films can divided in 4 main steps: (a) mixture preparation, (b) substrate cleaning, (c) mixture deposition, and (d) material solidification. All steps are separately discussed below:

Mixture preparation

PDMS precursor mixtures were prepared by combining Sylgard 184 base with its cross-linker at a ratio of 10:1 by weight and were subsequently mixed in a beaker for several minutes in order to uniformly disperse the cross-linker (Figure 7-1 a-c). The prepared mixture was then placed in a desiccator and degassed under vacuum (~0.8 bar below atmosphere) until no visible bubbles remained in the bulk (Figure 7-1 d-e).

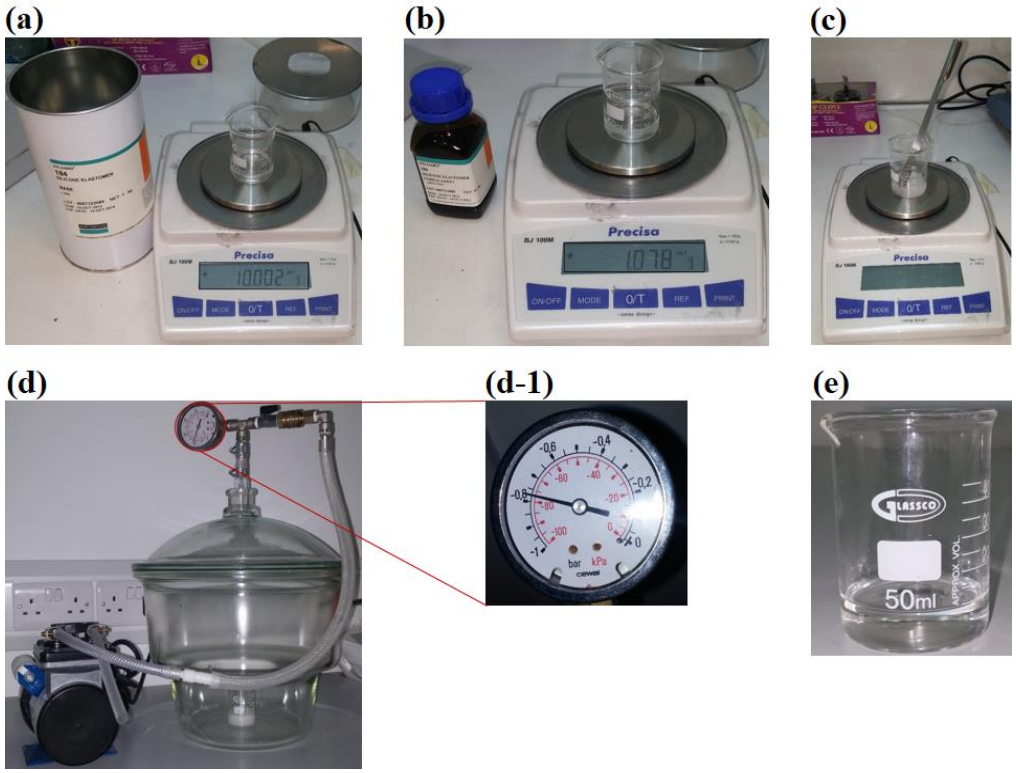

Figure 7-1: (a) Sylgard 184 base 10g poured into beaker. (b) Approximately 1g of curing agent is poured into the beaker, maintaining the 10:1 ratio. (c) Mixing with spatula for several minutes. (d) Mixture placed in desiccator for 10 min. (d-1) Desiccator pressure about 0.8bar below atmospheric. (e) Bubble free mixture.

Substrate preparation and cleaning

Typical lab glass substrates were cut into uniform pieces with a diamond glass cutter (Figure 7-2a). The pieces were subsequently cleaned in an ultrasonic acetone bath for 10 minutes (Figure 7-2b), and dried with N_2 gas gun in order to ensure that the surface is clean before PDMS deposition (Figure 7-2c).

Figure 7-2: (a) Glass chopping by diamond cutter. (b) Ultrasonic acetone bath for 10 min. (c) Drying with N_2 gas.

PDMS coating and solidification

The precursor mix was spin-coated onto orthogonal glass substrates for 10 seconds and 6V (3000 rpm) of power supply. The spin coating equipment was a custom-made device constructed by members of the RUNMS. As shown in Figure 7-3a it consists of a dc power supply and a small motor, which generated the necessary centrifugal force that is required to spread the liquid material onto the glass substrate. Finally, all coated samples were annealed at 150^{o}C for 10 minutes using a hotplate.

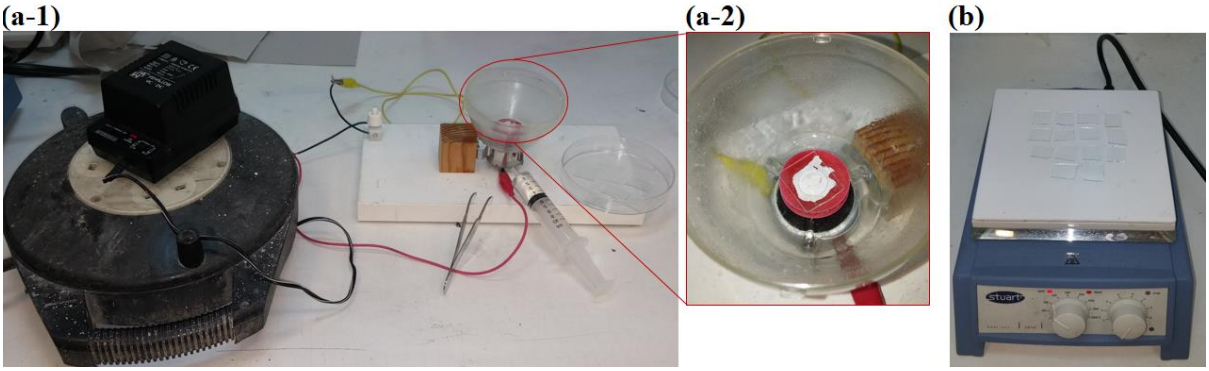

Figure 7-3: (a-1) Custom-made spin coating equipment, (a-2) Substrate holder, and (b) Annealing at 150^{o}C for 10 min using a hotplate

7.2.3 Plasma Processing of Surfaces

The abovementioned materials, namely Si, thermally grown SiO_2 and PDMS have been exposed to an inductively coupled plasma (ICP) generator. As it was previously mentioned, ICP is a type of plasma source in which the external energy is supplied by electric currents which produce electromagnetic induction that is a time-varying magnetic field. There are three types of ICP geometries: planar, cylindrical and half-toroidal. In this work, a cylindrical ICP generator was used for surface processing. The generator was purchased from Mantis Deposition Ltd (Mantisdeposition.de 2016), and has been installed in the Synthesis Lab of the Research Unit for Nanostructured Materials Systems.

Inductively Coupled Plasma (ICP) source

Mantis combined MATS30 and RFMAX30 ICP, hereafter referred to as 'Ion Source' (Figure 7-4b), is a part of a Hybrid Deposition System (HDS) of the RUNMS synthesis lab (Figure 7-4a). This specific ICP is also a hybrid system because it can operate as a plasma source RFMAX30 or as a deposition system MATS30 where the plasma dissociates the process gas into ions and neutral reactive atoms, which finally deposit high-quality compound materials. In this work, only the plasma source, namely 'RFMAX30' will be used.

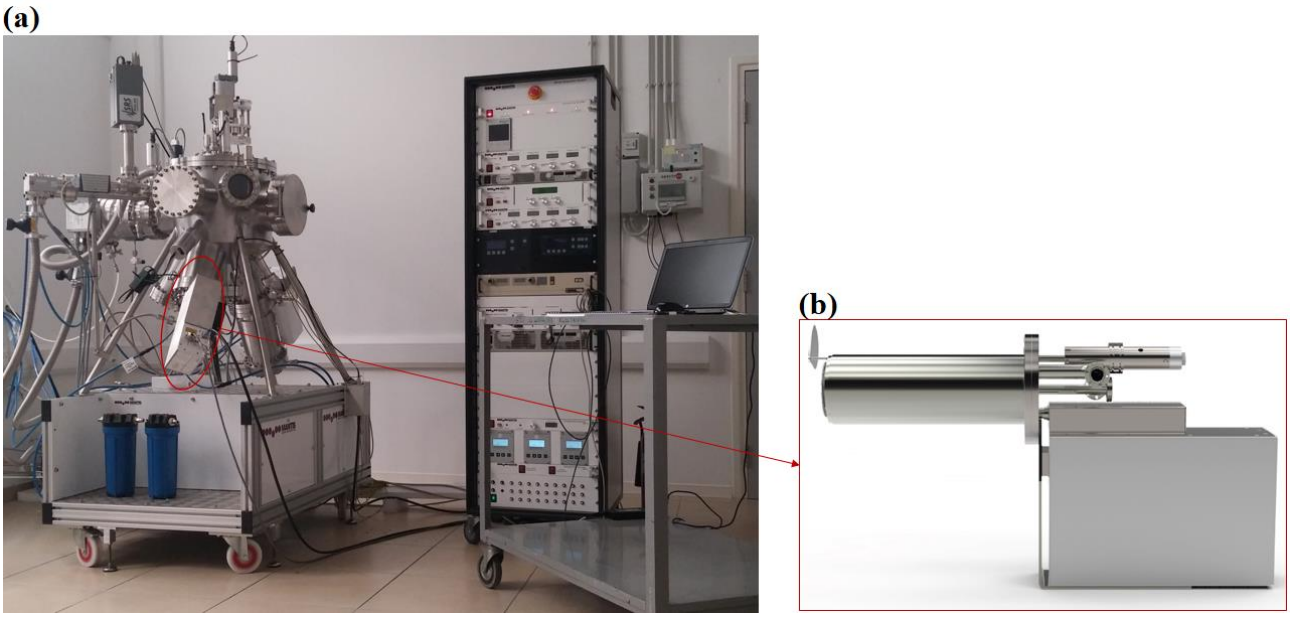

Figure 7-4: (a) HDS system, and (b) 'Ion Source'

The ion source is designed to work under ultra-high vacuum conditions (~10^{-9} mbar) and consists of integral shutter, matching network controller, water cooled induction coil, a high purity ceramic discharge tube and a bias grid (see Figure 7-5a).

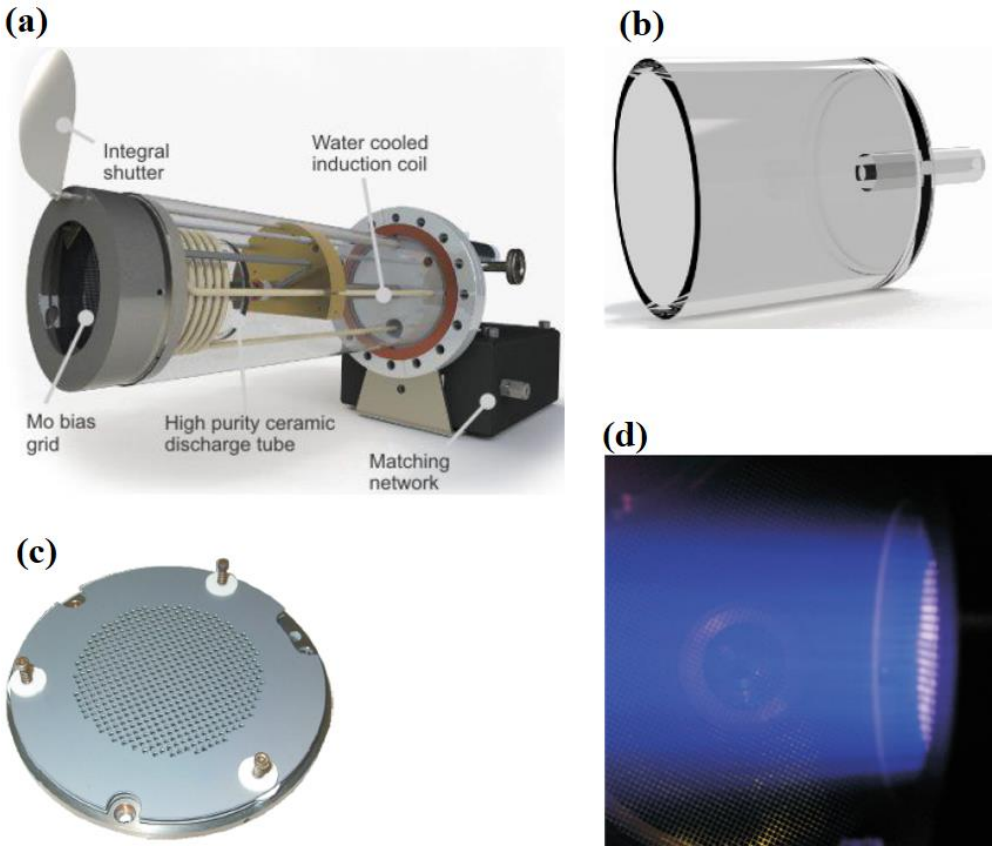

Figure 7-5: (a) Ion source main components, (b) discharge tube, and (c) Carbon bias grid. (d) Broad ion beam created from ICP-RFMAX30 source; images adopted from (Mantisdeposition.de 2016)

Operation

An RF external energy source transfers energy to the electrons through high frequencies which do not affect the generated ions. In our case, RF power (50-400W) transfers energy via a cylindrical induction coil which covers the discharge tube (see Figure 7-5b). When the necessary vacuum (~10^{-5} mbar) is reached and in the presence of gas in the discharge tube, RF power transfers energy to free electrons which gain high mobility that lead to multiple collisions with gas molecules. These collisions result in high energy state positive ions, as well as free radicals which finally represent the plasma state. The discharge tube is enclosed by a pair of high-transparency grids (Figure 7-5c). The inner grid has a voltage applied which is equal to the energy of the ion beam the user wishes to generate, i.e. the voltage values are equal to ion energy with eV units, while the outer grid is held at earth potential. This potential difference between the grids creates a negative field gradient which acts to draw the positive ions from the plasma and through the holes in the outer grid forming one broad ion beam which emerges into the chamber (Figure 7-5d). The beam is targeted directly onto the substrate holder

(Figure 7-6b) and the plasma processing begins once the shutters of ion beam 'gun' and substrate holder open.

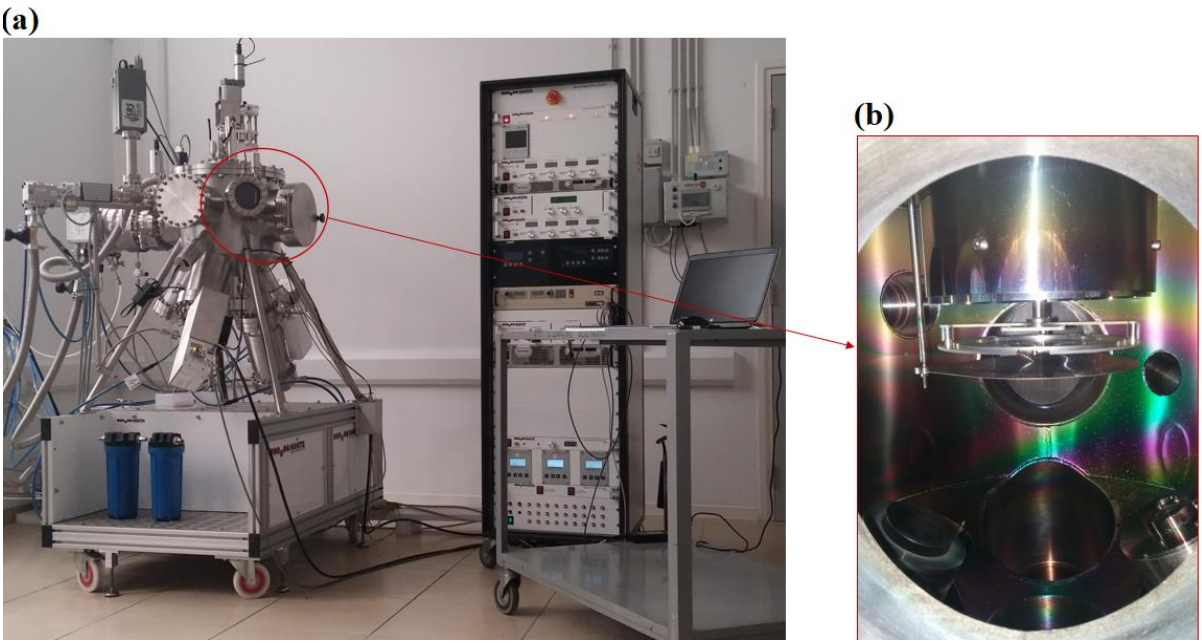

Figure 7-6: (a) HDS system, and (b) Substrate holder

Important parameters and system specifications

The parameters of hybrid ICP source can be divided into 3 groups: parameters that are correlated with (a) plasma generation, (b) ion characteristics and (c) all remaining parameters.

1. **Parameters controlling plasma generation**

The first parameter is the RF power, which is provided by an external controller and as it was mentioned before plays a crucial role in plasma generation. The manufacturer (Mantis Deposition Ltd) provides a graph, shown in Figure 7-7a, that explains the correlation between RF power and beam current. As we can see a linear relationship exists, which can be translated as means of modifying the beam current by changing the RF power with a conversion rate of 0.33mA/W. The current rate basically represents the ion density, thus the higher the current the larger the amount of generated ions. The second parameter that correlates with plasma generation is the gas flow. It is easy to understand that increasing the gas flow means more available for collisions molecules will fill the chamber giving the possibility to generate more ions. However the flow of the gas has a limit value which depends on the dimensions of the reaction chamber, and the power of the system. For instance, if the flow is too high, the RF power and the free electrons will not be enough to create the required amount of ions and

therefore plasma state will never be reached. Hence, the manufacturer advices to use high precision mass flow controllers with flows from 0.1-10 sccm (standard cubic centimeters per minute) for this particular system.

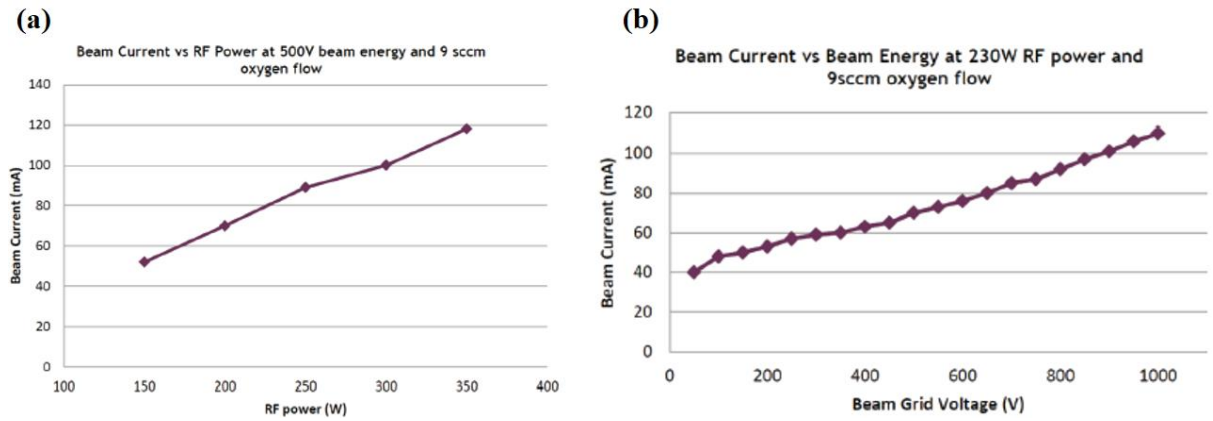

Figure 7-7: (a) Relationship between RF power and ion beam current, and (b) Relationship between grid voltage and beam current, images adopted from (Mantisdeposition.de 2016)

2. Parameters correlated with ion characteristics

As it was stated before, the 'C bias grid' is the component that attracts the generated ions and drives them onto the substrate holder in the form of a beam. Therefore, bias grid is the parameter that controls the kinetic energy of the ions. Increasing the grid negative potential, higher attraction of the ions appears (Mantisdeposition.de 2016). This relation is presented in Figure 7-7b, where a linear correlation between grid voltage and beam current can be observed. Another important parameter that can increase the ion kinetic energy is the substrate bias voltage. Applying a negative voltage on the substrate holder can generate additional attractive forces and subsequently lead to higher acceleration of impacting ions.

3. Other parameters

The remaining RFMAX30 system characteristics are presented in this section. These include the ion angle of attack and substrate temperature. Based on literature data reviewed in sections 6.3.3 and 6.3.4 these parameters are primarily linked with the reactions between ions and processed samples. In the case of non-reactive argon ion sputtering, considered herein, these parameters are of secondary importance. Table 7-1 summarizes the ion beam characteristics.

Table 7-1: RUNMS ICP source specifications; data from (Mantisdeposition.de 2016)

Gas compatibility	O_2, N_2, H_2, Ar	*RF power*	50-400W
Beam diameter	30 mm	*RF Tuning*	Automatic
Gas flow	0.1 – 10 sccm	*Power Supply*	600 W RF power supply
Water cooling	0.5 l/min	*Shutter*	Manual

Experimental Plan

The experimental plan described in this section was decided according to the literature review and the parameters and capabilities of the available 'Ion Source' described above. Since this work is going to investigate the non-reactive plasma processing, Argon (Ar) gas is used for plasma generation. The plasma characteristics were kept constant on all experiments with RF power at 200W and Ar gas flow at 10 sccm. We here investigate the effect of grid voltage and time of exposure (fluence) on the surface process response. Substrate bias voltage was not applied and substrate temperature was not controlled.

The exposure time is very important for the determination of material removal rate, etching rate, while grid voltage is very important in topographical investigation of the samples. Therefore, the experimental plan consisted of two cases. The first case keeps every parameter constant instead of the exposure time, and the second case keeps every parameter constant instead of the grid voltage. The detailed experimental plan is shown in Table 7-2.

Table 7-2: Plasma processing experimental parameters and cases

CONSTANT PARAMETERS	
RF Power	200 W
Argon gas flow	10 sccm
Substrate bias voltage	0
Substrate holder rotation	10 rpm (for uniform processing)
EXPERIMENTAL CASE 1: EFFECT OF EXPOSURE TIME	
Grid Voltage	200 V
Exposure Time	5, 10, 20 and 30 min
EXPERIMENTAL CASE 2: EFFECT OF ION ENERGY	
Exposure Time	30 min
Grid Voltage	150, 200, 250 and 300 V

7.3 Characterization Methods

Optical, topographical, physical and wetting properties of Ar plasma treated materials have been studied. Specifically for the PDMS plasma exposed samples, ultraviolet-visible (UV-VIS) spectrophotometry and contact angle measurements (CA) were performed to determine respectively the optical transmittance and wetting properties. The SiO_2 film thickness after plasma exposure was measured using white light reflectance spectroscopy (WLRS). Finally for all PDMS, SiO_2 and Si samples, atomic force microscopy (AFM) was used in order to determine the topography and roughness after plasma processing. Since WLRS and AFM techniques are described in Part A of this thesis, only CA and uv-vis transmittance characterization methods will be discussed.

7.3.1 UV-VIS Transmittance Spectroscopy

The transmittance spectra of all PDMS films were recorded in order to investigate the optical transparency as a function of the plasma exposure. The spectrophotometer used to record the transmittance spectra is a Thetametrisis FR-Basic UV/VIS spectrophotometer, which has been described in Section 4.3.1

Procedure of Measurement

Before the data collection process, it is important to verify that the appropriate optical fibers are used. The procedure starts when the generated light travels via optical fibers passing through the material that is under investigation and transferred again through the optical fibers to the photocell detector. The detector collects and converts the signal to wavelength numbers and transmittance intensity, which finally gives the transmittance spectrum. For precise measurements of the transmittance characteristics, the following algorithm is used in FR-Monitor software:

$$T_{(\lambda)} = \frac{I_{s(\lambda)} - I_{d(\lambda)}}{I_{o(\lambda)} - I_{d(\lambda)}} \times 100\% \qquad (7\text{-}1)$$

where I_o is the reference light intensity, i.e the light intensity of the light source used as it is recorded by the spectrometer without passing through the sample of interest. In our case the reference light intensity is the light passed through the glass which was used as substrate for PDMS coating. I_s is the light intensity through recorded after it passed through the sample of interest, and I_d is the dark intensity which is the light intensity recorded by the spectrometer

with the light source switched-off, without sample, namely it is the intensity recorded from the room light sources. T is the transmittance of the under investigation material and it can be presented either as values from 0-100% or just from 0-1. In this work the transmittance spectra of all PDMS samples were recorded at room temperature, in the range of 300 to 800nm of source light and as reference spectrum was used the transmittance spectrum of the glass substrates.

7.3.2 Wetting Characterization

The topic of wetting has received significant attention from both fundamental and applied points of view. It plays a pivotal role in many industrial processes such as oil recovery, lubrication, liquid coating and self-cleaning surfaces (Bracco & Holst 2013). The following two subsections provide the basic physics of solid surface wettability and the apparatus that is used to characterize it.

Physics of Surface Wettability

Wetting is the fundamental process of liquid interaction at solid-gaseous interfaces, and it basically describes how a liquid comes into contact with a solid surface (Koch et al. 2008). This interaction is described by several factors and characteristics of both states (liquid and solid), namely their physical chemistry, the statistical physics, the intermolecular and long-range forces (Van Der Waals) and the fundamental laws of fluid-dynamics. Depending upon the properties of the liquid and the solid surface in contact the liquid droplet may assume two different wetting equilibrium regimes: 1) partial wetting or 2) complete wetting, Figure 7-8a and Figure 7-8b, respectively.

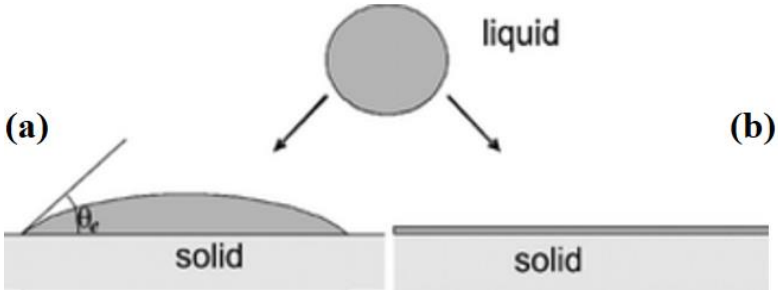

Figure 7-8: Equilibrium wetting regimes, (a) partial wetting, and (b) complete wetting

The most critical parameter which indicates the wetting property of a solid surface that is in contact with a liquid droplet is known as contact angle, θ_c. Contact angle (CA) is a quantitative measure of the degree of a solids wettability. It is defined geometrically as the angle formed

by a liquid drop at the three phase boundary where a liquid, vapor and solid intersect each other (Sakhuja 2014). Based on their contact angles, the wetting behavior of surfaces can be separated in four categories:

1) Superhydrophobic, with CA>150^o
2) Hydrophobic, with CA>90^o
3) Hydrophilic, with CA<90^o
4) Superhydrophilic, with CA<10^o

Different mathematical models that describe the wetting of a solid surface have been proposed in the literature. The most well-known are: (a) Young's model which is suitable for perfectly smooth and chemically homogenous solid surfaces, (b) Wenzel's model and (c) Cassie–Baxter model which are for more realistic solid surfaces that are rough and chemically heterogeneous (Yao & He 2014). The three models are schematically shown in Figure 7-9.

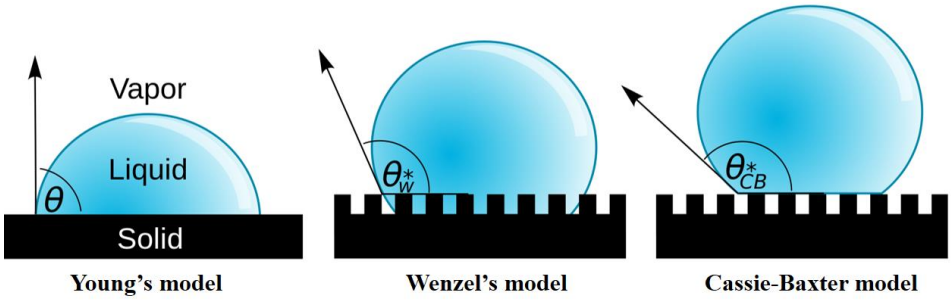

Figure 7-9: Wetting models

Contact Angle (CA) Measurements

Contact angle measurements are usually performed by an optical tensiometer (Figure 7-10). The main components of this apparatus are: substrate holder-stage, camera, light source and automated droplet system. In this work a custom-made CA apparatus was used. This is shown in Figure 7-11a and consists of all the essential components: light source, camera, substrate holder and a manual droplet injection.

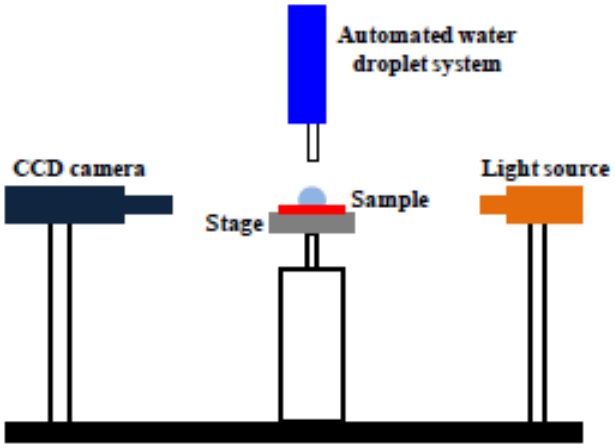

Figure 7-10: Typical Contact Angle apparatus, image adopted from (Sakhuja 2014)

The measurement procedure is performed using 2ml of deionized water droplet injection in the middle of the substrate, using a small scale syringe (Figure 7-11c). The sample is shielded with an aluminum cover in order to avoid surrounding illumination. Before the droplet photograph is taken, the light source is turned on in order to create a shade which gives the precise geometry of the droplet.

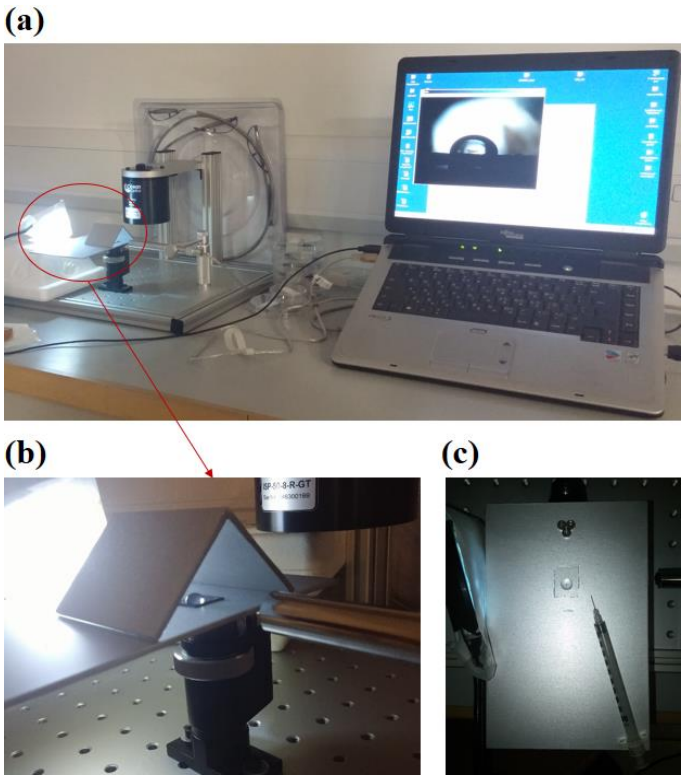

Figure 7-11: (a) Self-designed contact angle apparatus, (b) sample holder, light source and camera, (c) substrate and droplet placement

Finally in order to measure the CA, all droplet photographs are analyzed using ImageJ equipped with 'Drop Snake Analysis' plugin. This particular plugin can accurately measure the contact angle by fitting a piecewise polynomial on the snapped droplet (Bigepfl.ch 2016; Dropsnake 2011). In this work contact angle measurements were performed on all plasma exposed PDMS samples in two time scales: 1) exactly after plasma processing, and 2) 35 after plasma exposure and air storage.

7.4 Chapter Summary

PDMS films were fabricated using a chemical mixture of base and curing agent in the ratio of 10:1, a spin coating deposition and an annealing solidification process. The synthesized PDMS samples, together with Si and thermally grown SiO_2 thin films (synthesized in Part A of this thesis) were exposed to inductively coupled plasma (ICP). The investigation of the parameters of the ICP system lead to two experimental cases, grid voltage and exposure time dependency. All samples were characterized physically, topographically, geometrically and optically. The principles of contact angle and uv-vis transmittance spectroscopy techniques have been analyzed in detail, since these techniques were not mentioned in the previous part. The results from the synthesis, processing and characterization are discussed in the following chapter.

CHAPTER 8 EXPERIMENTAL INVESTIGATION OF PLASMA PROCESSING: RESULTS AND DISCUSSION

8.1 Chapter Outline

The results obtained from the experimental investigation outlined in Chapter 7 will be presented and critically discussed within this chapter. The etching rate and topographical characteristics of silicon and silicon dioxide materials cover the first part of this chapter. In the second part, the AIB-induced changes on the topographic, optical and wetting characteristics of PDMS are discussed and potential applications are outlined.

8.2 Plasma Processing of Silicon and Silicon Dioxide – Ion Etching

Based on the literature review presented in Section 6.3.3 silicon and silicon dioxide materials are expected to be etched after argon ion bombardment (AIB). Therefore, this section investigates the etching rates that can be achieved with our instrument and the topographical changes that Si and SiO_2 undergo when exposed to different exposure durations and ion kinetic energies.

8.2.1 Etching Rate of Silicon and Silicon Dioxide

The determination of etching rate was achieved by calculating the thicknesses of SiO_2 thin films before and after the AIB, using the WLRS technique described in Section 4.3.2. Table 8-1 shows the thickness values before and after AIB for ions generated at RF power of 200W and accelerated with grid voltage 200V (see case 1, page 93).

Table 8-1: SiO_2 thin film thickness values before and after 200W and 200Vgrid AIB, (measured using WLRS technique)

Exposure Time [min]	Thickness [nm]		
	Before Exposure	After Exposure	Removed thickness
5	107.6	106.3	1.3
10	107.6	104.3	3.3
20	107.8	99.3	8.5
30	106.7	93.4	13.3

Based on the values presented in Table 8-1 a plot of etched thickness versus exposure time is constructed and presented in Figure 8-1. The data lies on a straight line, a linear fit of which provides an estimate of the etching rate (slope) which is equal to 0.49 nm/min.

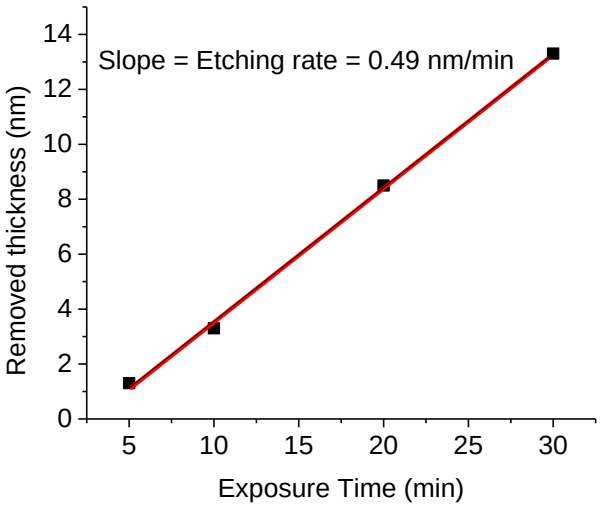

Figure 8-1: Etching rate of SiO_2 thin films under Argon Ion Bombardment (AIB)

The calculated etching rate is within the range of 0.4-2.5 nm/min reported by (Comfort et al. 1987). They also reported that the etching rate is strongly depended on the substrate bias voltage, which can be translated into the ions kinetic energy. In order to investigate the effect of ion energy on the etching rate we plotted the calculated etching rates for several grid voltages the results of which are presented in Figure 8-2. One can note the strong dependence of the etching rate to the ion energy: increasing the grid voltage from 200V to 300V one can triplicate the etching rate, reaching almost 1.5 nm/min. In the case of c-Si the removed thickness was not calculated, but according to (Comfort et al. 1987) the etching rate for silicon is lower than SiO_2 and varies within 0.3-0.7 nm/min.

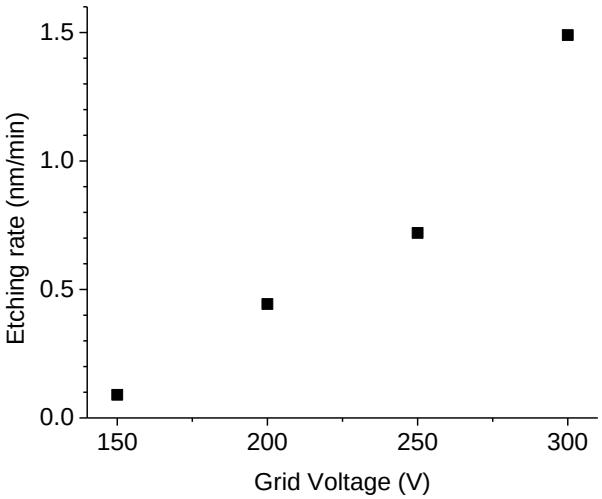

Figure 8-2: SiO_2 Etching rate vs Grid Voltage

8.2.2 Surface Quality of Ion Etched Silicon and Silicon Dioxide

In order to determine the quality of the etched surfaces we need to investigate three parameters, 1) uniformity of material removal, 2) surface topography and 3) surface roughness. Using the WLRS technique, 4 different SiO_2 samples were measured after AIB. Six thickness measurements were taken along the longitudinal center line of each sample, showing that the standard deviation varies from 0.1 – 0.6 nm. It can be therefore concluded that the material removal is uniform along the whole exposed surface.

According to (Todorov & Fossum 1988; Hu et al. 1991) the ion kinetic energy plays a crucial role not only on etching rate but also on the quality of the exposed surfaces. The higher the ion kinetic energy the larger and more aggressive are the collisions with surface atoms. For instance energies of 1200eV can cause significant damage on c-Si surface. In our work, grid voltage was used to control the ion energies, namely the applied voltage is equivalent with the electron volts (eV). Therefore based on different ion kinetic energies the topographical investigation was achieved by AFM tapping mode measurements. The results of c-Si and SiO_2 samples are shown in Figure 8-3 and Figure 8-4, respectively. The AFM images suggests that surface topography remains almost unaffected by AIB, at least for the ion energies considered within this study, however on some images nanopeaks are observed. It is assumed that these peaks related to particles that have been etched from the walls of the chamber or from the exposed materials and transferred/attached on the materials surfaces.

However the presence of these particles is not as important as the surface roughness. The determination of surface roughness was achieved using the AFM 3D rms roughness and the results for both materials are shown in Figure 8-5. Despite some fluctuations that can be observed in the RMS data, the actual values are in the Angstrom scale suggesting that the atomic scale smoothness is retained for all specimens; both c-Si and a-SiO_2.

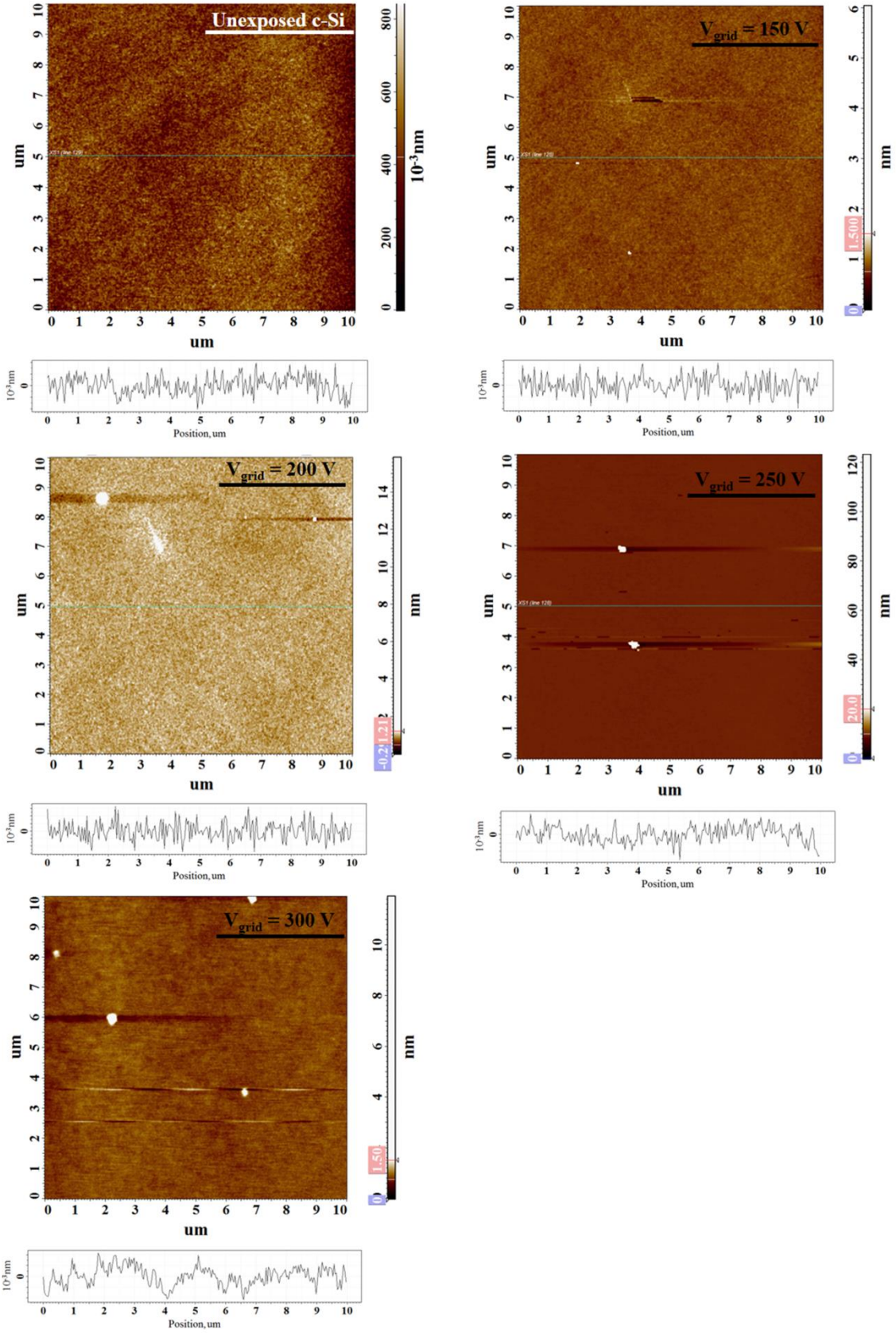

Figure 8-3: c-Si samples exposed to different ion kinetic energies, AFM 2D topography and cross section images

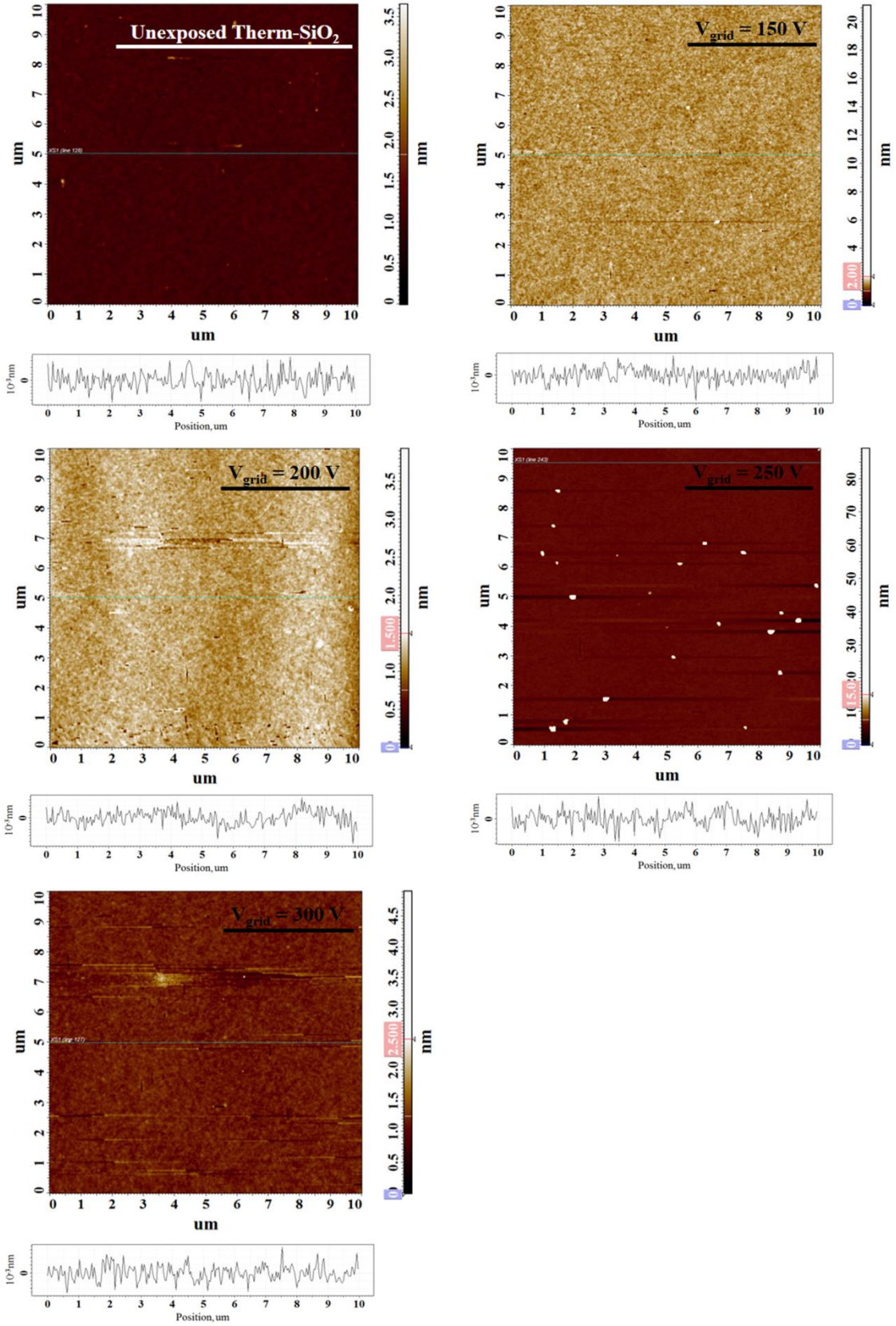

Figure 8-4: Therm-SiO_2 samples exposed to different ion kinetic energies, AFM 2D topography and cross section images

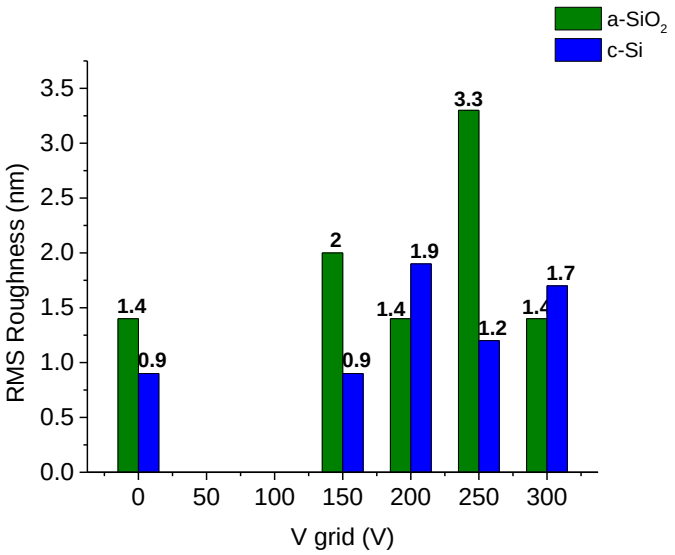

Figure 8-5: AFM 3D RMS roughness of c-Si and a-SiO_2 after AIB of different ion kinetic energies

8.3 Plasma Processing of PDMS – Ion Implantation

In contrast to Silicon and Silicon Dioxides (hard materials), AIB of PDMS led to surface pattering instead of material etching. Figure 8-6 shows the surface morphology of a PDMS exposed at AIB for 30 min and at 200eV ion energy. Impressively, the relatively smooth surface of PDMS transformed into a wrinkled pattern with several interesting characteristics that will further be investigated below. The effect of AIB parameters on the wrinkling characteristics form the basis of our investigation, the results of which are presented below.

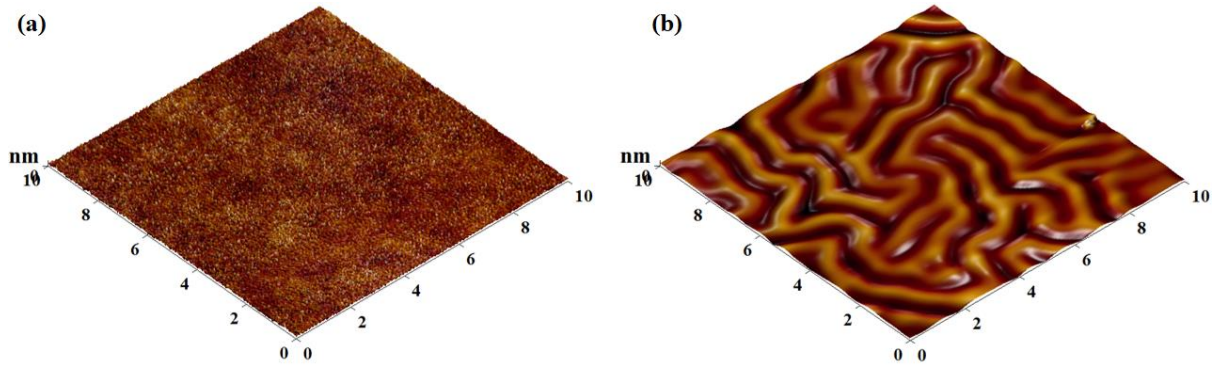

Figure 8-6: AFM 3D surface morphologies (a) Unexposed $PDMS_{10:1}$ and (b) PDMS exposed to AIB with: RF Power 200W, V_{grid} 200V and exposure time of 30 min

8.3.1 Physics of Wrinkles

In order to understand how the wrinkles are generated, it is necessary to concentrate on the changes of the surface chemistry. As it was mentioned in Section 6.2.1, PDMS is a synthetic polymer that is constructed with a repeating unit of Si-O and methyl groups (CH_3) attached directly to the silicon atom via silicon-carbon bonds (C-Si), therefore the repeating monomer of PDMS can be written as $[(CH_3)_2SiO]_n$. The exposure of PDMS surface to AIB results in a significant reduction of carbon-to-silicon ratio (C/Si) and at the same time increase in oxygen-to-silicon ratio (O/Si). This indicates that the surface is oxidized due to the replacement of methyl groups with oxygen, as reported by (Nagashima et al. 2012; Moon et al. 2007). Additionally, (Park et al. 2015) and (Moon et al. 2007) specify that the oxidation on PDMS surface creates an amorphous silica SiO_x stiff layer that is responsible for the buckling of the PDMS wrinkles observed in Figure 8-6.

(Chen & Hutchinson 2004) have dealt with wrinkles of externally compressed thin films under biaxial stress states. Generally, when a stiff film is growing on a compliant substrate, the film stress will increase at the early stage of deposition as if it was deposited on a rigid substrate. However, in the case of compliant substrate once the stress or the mismatch strain in the film exceeds a critical value, the stiff film will buckle minimizing at the same time its internal compressive energy (Figure 8-7).

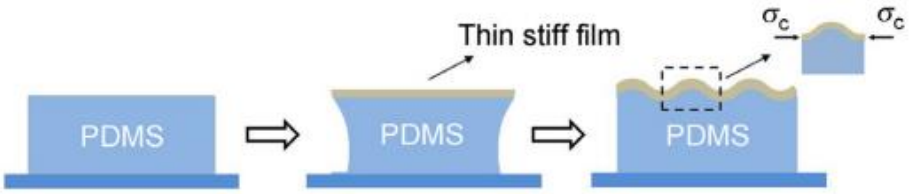

Figure 8-7: PDMS surface buckling after the deposition of a thin stiff layer, image adopted from (Wu et al. 2014)

The buckling usually creates wrinkles with specific amplitude and wavelength. (Moon et al. 2007) demonstrated that the geometric characteristics of the ion beam irradiated PDMS wrinkled surfaces can be described with high accuracy through:

$$\lambda \approx 4h_f \left(\frac{E_f}{E_s}\right)^{1/3} \tag{8-1}$$

where λ is the wavelength of wrinkles, (h_f) is the film thickness and (E_f/E_s) is the ratio of Young's moduli between the film and the substrate. Additionally, (Nagashima et al. 2012) showed that the amplitude, (A) of the wrinkles can be calculated through:

$$A \approx h_f \sqrt{\frac{\varepsilon}{\varepsilon_c} - 1} \tag{8-2}$$

where (ε) and (ε_c) are the applied strain and the critical strain to induce buckling, respectively.

8.3.2 Tailoring the Surface Topography

The wrinkling phenomenon can be tailored by monitoring the AIB characteristics. The two main parameters that are investigated within this study are: 1) the fluence which is correlated with the irradiation exposure time and 2) the ion kinetic energy which is algebraically equal to the applied grid voltage (Mantisdeposition.de 2016)

Fluence effect on wrinkles

Based on the elementary charge *($1.6x10^{-19}C$)*, the grid current, the exposure time and the ion beam cross sectional area *($25.52\ cm^2$)* the fluences can be calculated:

$$Q = Amp \times t \quad \leftrightarrow \quad Fluence = \frac{Amp \times t\,[ions - C]}{1.6 \times 10^{-19}[C]} \times \frac{1}{25.52\ cm^2} \qquad \left[\frac{ions}{cm^2}\right] \tag{8-3}$$

A summary of all fluence values used in this study are reported in Table 8-2

Table 8-2: Calculated fluence of AIB: RF = 200W and Grid Voltage = 200V

Exposure Time [sec (min)]	Grid current [Ampere]	Fluence [ions/cm^2]
300 – (5)	**0.062**	**6.3e18**
600 – (10)	**0.061**	**13e18**
1200 – (20)	**0.061**	**25e18**
1800 – (30)	**0.063**	**37e18**

Figure 8-8 shows AFM images in which the morphologies of wrinkled structures on PDMS surfaces with respect to exposed fluence are presented together with the corresponding analyses of the wrinkles' periods. The periods of the wrinkle structures were quantified using 2D Fast Fourier Transformation (FFT) power spectrum of the AFM images, as shown in Figure 8-8c. The power spectrum represents the power distribution of wrinkle pattern over spatial frequency domain converted from the spatial domain. The white point distributions indicate the

periodicity in the surface morphology and the size of the white circular distribution increase means that the wrinkle wavelengths' periods decrease. Moreover, in Figure 8-8 (b) the frequency distribution is presented. The frequency indicates the inverse of wavelengths' periods, namely the distance from one 'wave' to another and the y-axis represent the intensity of each period.

As shown in Figure 8-8 (a) no significant changes in surface morphology are presented as the ion dose increases. Figure 8-8 (c) shows that the surface contains wavelengths with almost the same periods and Figure 8-8 (b) presents distributions with the same range but different intensities. In order to see clearly the dependence of the wrinkle patterns on fluence, the plots of Figure 8-9 are constructed. Based on Eq. (8-2) (Nagashima et al. 2012) proposed that the extent of applied strain is limited by the nature of the polymer, therefore the amplitude of the patterns created should be on the order of the layer thickness. Figure 8-9 (b) shows an increase in amplitude with almost a constant rate in compliance with the above-mentioned behavior. Therefore, it can be assumed that the thickness of the generated amorphous silica on top of the PDMS surface, is in the scale of nano-meters. Additionally this behavior can be approved by the wavelength plot, Figure 8-9 (a). Based on Eq. (8-1) the wavelength is also proportional to layer thickness, but since the film thickness is in the scale of nano-meters the changes are very small and the plot shows a plateau in wavelength after 20 min of exposure time or 25e18 ions/cm^2 dose.

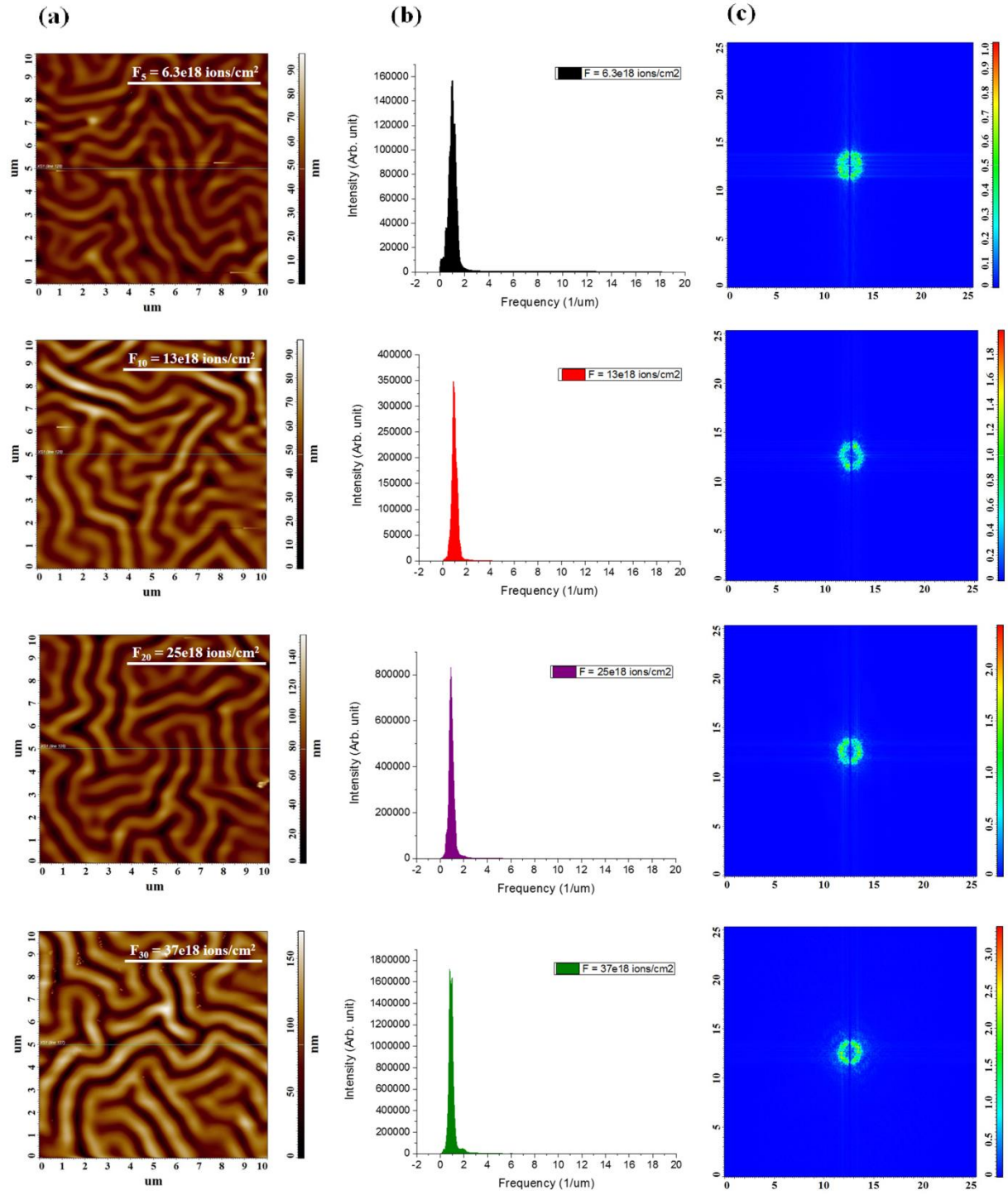

Figure 8-8: (a) AFM images, (b) wavenumber distributions, and (c) 2D FFT patterns of wrinkle structures formed on PDMS at different fluences.

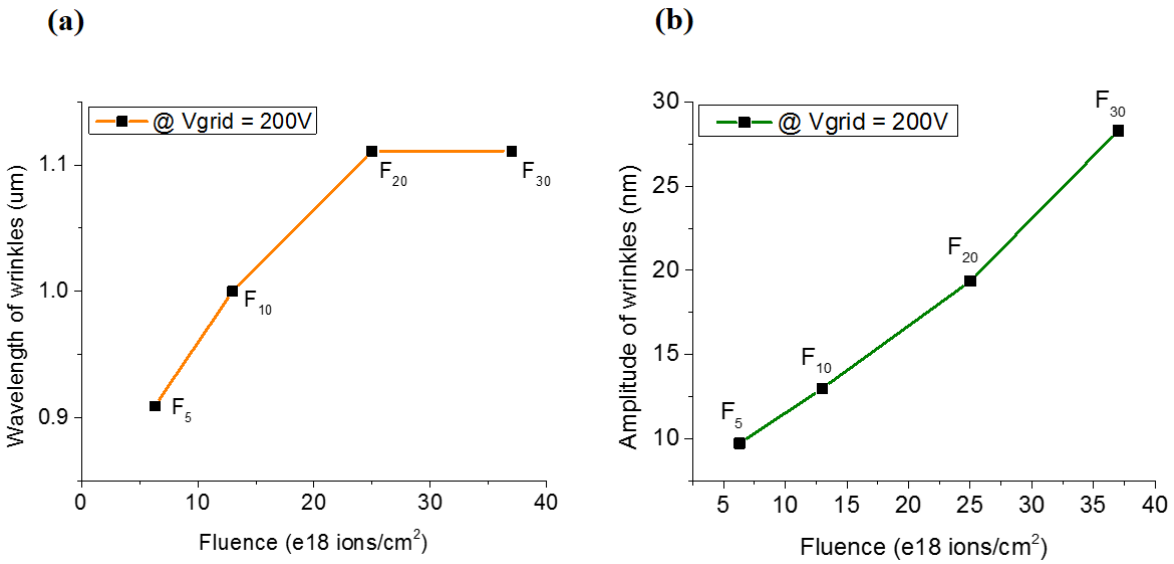

Figure 8-9: (a) Wavelength of wrinkles vs fluence, and (b) Amplitude of wrinkles vs fluence, the subscription of F values indicates to the exposure time in minutes.

Ion energy – Grid voltage

Another very important parameter that affects the morphology of the wrinkles is the grid voltage. Figure 8-10(a) shows AFM images of the exposed PDMS surfaces at various grid voltages. It is clear that the grid voltage plays an important role in wrinkle generation and further modification. Looking at the same figure, we can see that PDMS surfaces passes through a non-wrinkle stage at 150V to a completely wrinkle surface at grid voltages higher than 150V. Therefore it can be assumed that although the PDMS surface is different than its bulk nature, the grid voltage which is equal to ion energy of 150eV is not enough to make crucial changes on the surface. However the further increase of the grid voltage gives wrinkle surface with shorter wavelengths' periods, which is confirmed by the 2D FFT power spectrum and frequency distributions (Figure 8-10c and Figure 8-10b, respectively).

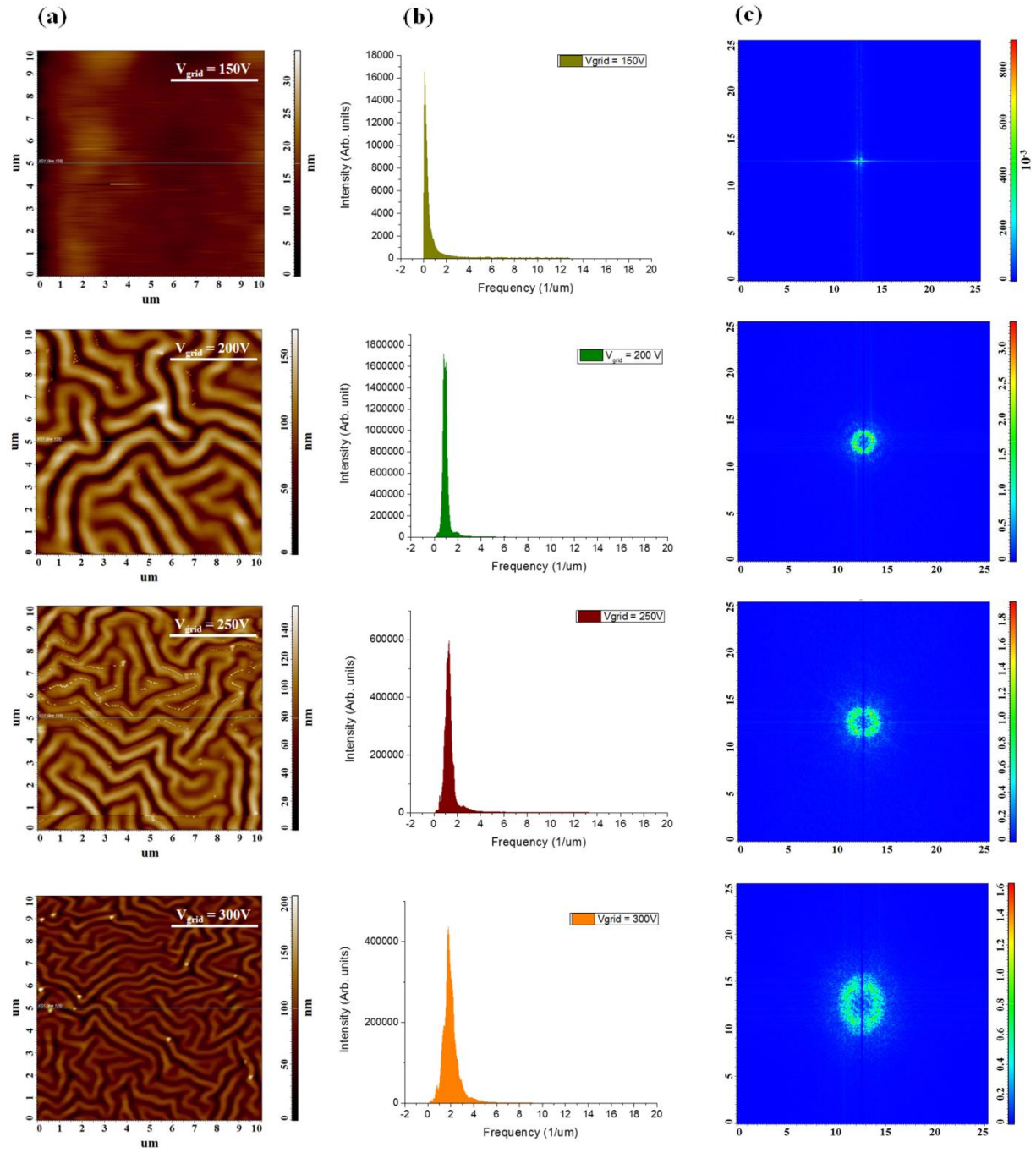

Figure 8-10: (a) AFM images, (b) wavenumber distributions, and (c) 2D FFT patterns of wrinkle structures formed on PDMS at different ion energies-grid voltage

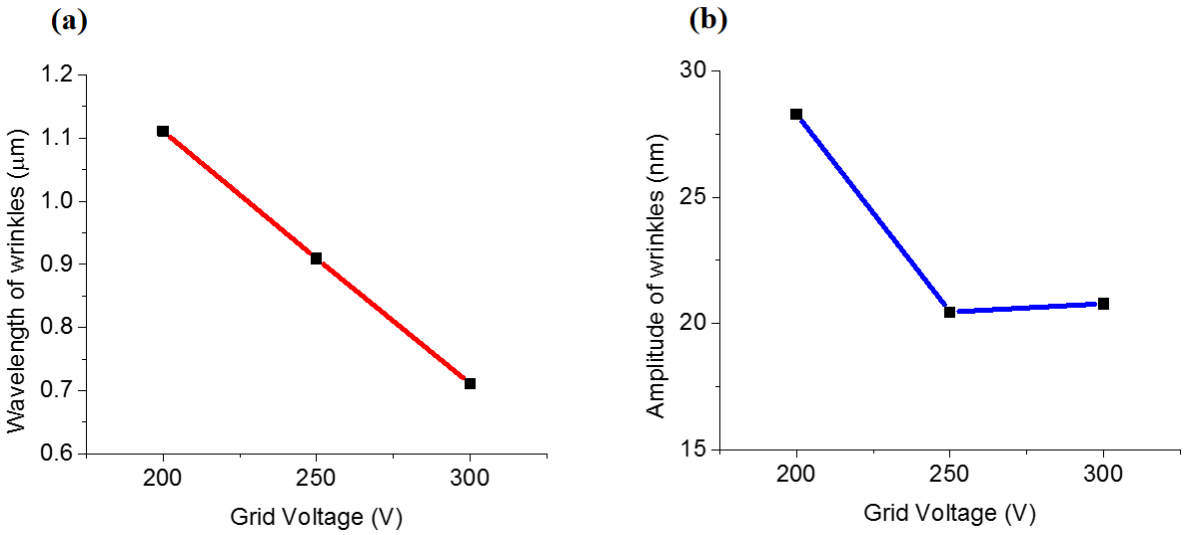

Figure 8-11: (a) Wavelength of wrinkles vs. grid voltage, and (b) Amplitude of wrinkles vs grid voltage

A reduction in amplitude of wrinkles is presented in Figure 8-11b, which shows a spontaneous reduction of wrinkle amplitude in the range of 200V – 250V, which leads to a stabilization at approximately 20 nm.

On the other hand plotting the wrinkle wavelength data versus the applied grid (the 150V case is ignored), an extreme dependence is shown in Figure 8-11a. The wavelength reduces with a rate of almost 200nm per 50V, after 200V. This dependence can be explained by 2 factors that grid voltage affects: 1) the ion fluence, and 2) the ion kinetic energy. As it was explained in Section 7.2.3, by increasing the grid voltage, more ions can be extracted from the reaction chamber, and the surface is being exposed to higher fluences (see Figure 8-12a). Although the fluence increases the values cover a range which according to Figure 8-12b do not affect the wavelengths' period. Therefore it can be assumed that all the wavelength changes are due to the ion kinetic energy. In conclusion, further investigation is needed in order to understand the physical mechanism of ion kinetic energy and wrinkle wavelength dependency.

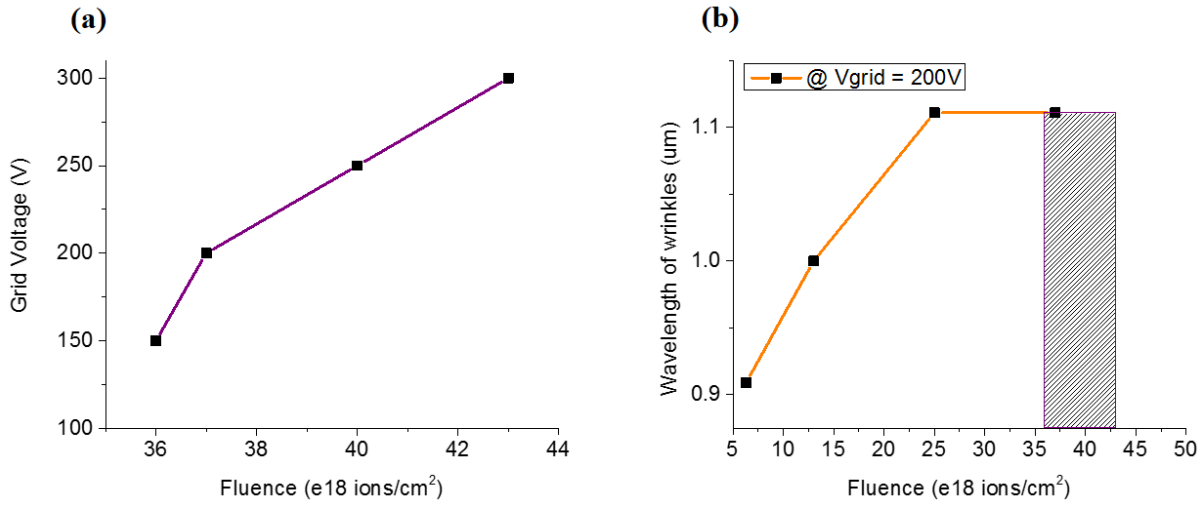

Figure 8-12: (a) Grid voltage vs fluence, and (b) wavelength changes with respect to the fluence

8.4 Wrinkled Surface Characteristics

In this section the wetting and optical characteristics of the AIB PDMS surfaces are presented and discussed.

8.4.1 Wetting characteristics

After plasma treatment, the surface of the investigated PDMS changed in nature from hydrophobic CA of 91.8^{o} to hydrophilic with CAs less than 50^{o} (Figure 8-13a-b). The physics behind this major change lie within the changes in surface chemistry. After AIB and the oxidation of PDMS surface, incorporation of various polar functionalities increased the hydrophilicity of the surface (Malecha et al. 2010). Since different works reported that hydrophobic recovery of PDMS surfaces appears after some aging time, it was decided to investigate this phenomenon. CA measurements of the same samples were performed 35 days after AIB exposure (Figure 8-13a). Therefore, the modification effect was not permanent due to the migration of polar groups of low molecular weight from the surface to the bulk of the material to reduce the surface energy (Malecha et al. 2010). In general the hydrophobic recovery does not reach the initial wetting properties of PDMS due to some permanent changes on the surface.

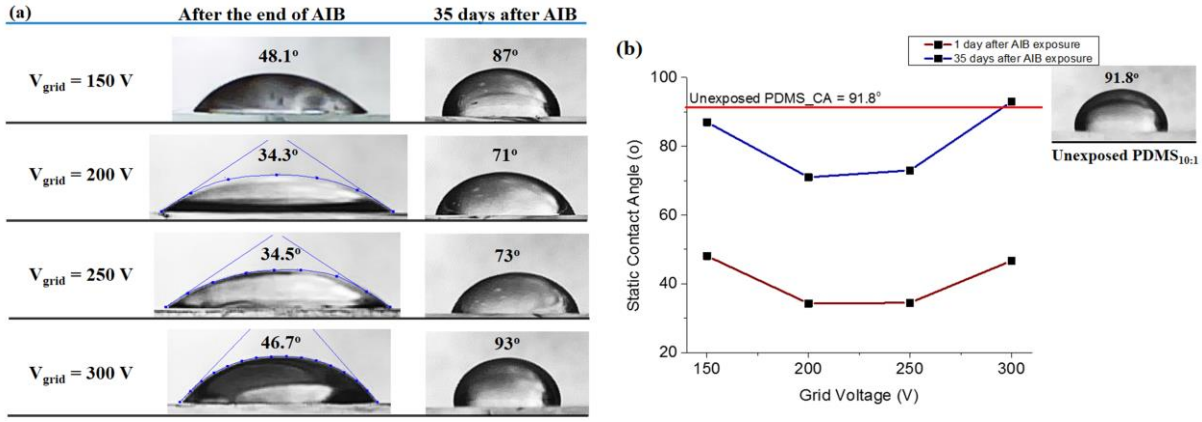

Figure 8-13: Wetting properties of PDMS exposed to different kinetic energies and measured at different times, (a) shows the CAs after AIB and 35 days after AIB, and (b) shows the plot of CAs versus grid voltage

8.4.2 Optical properties

As it was mentioned in Section 6.2.1, PDMS has good optical transparency. Figure 8-14 approves that in the visible spectrum PDMS has almost the same transparency as a glass substrate. Fortunately this property remains almost unaffected after AIB of PDMS (Figure 8-15a-b).

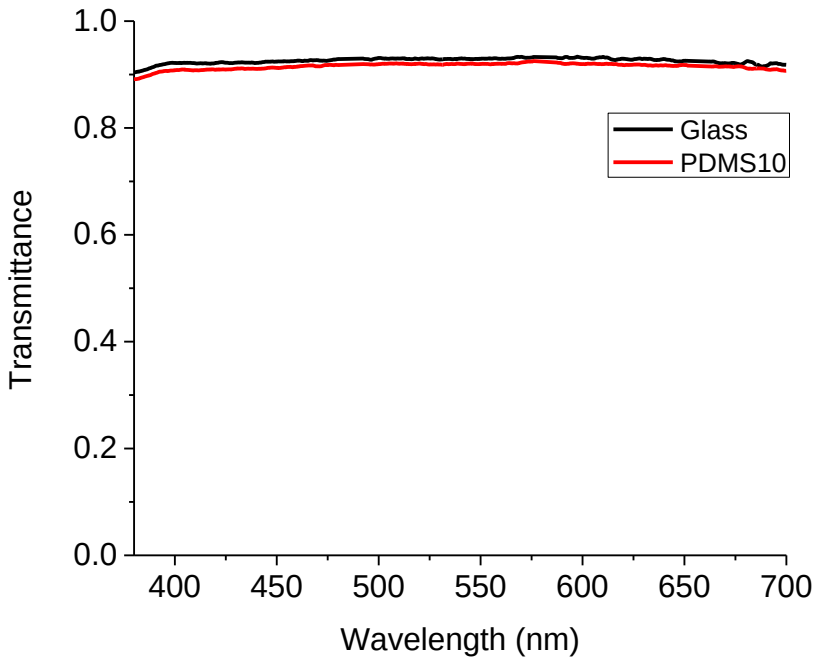

Figure 8-14: Transmittance spectrum of PDMS 10:1 vs glass substrate

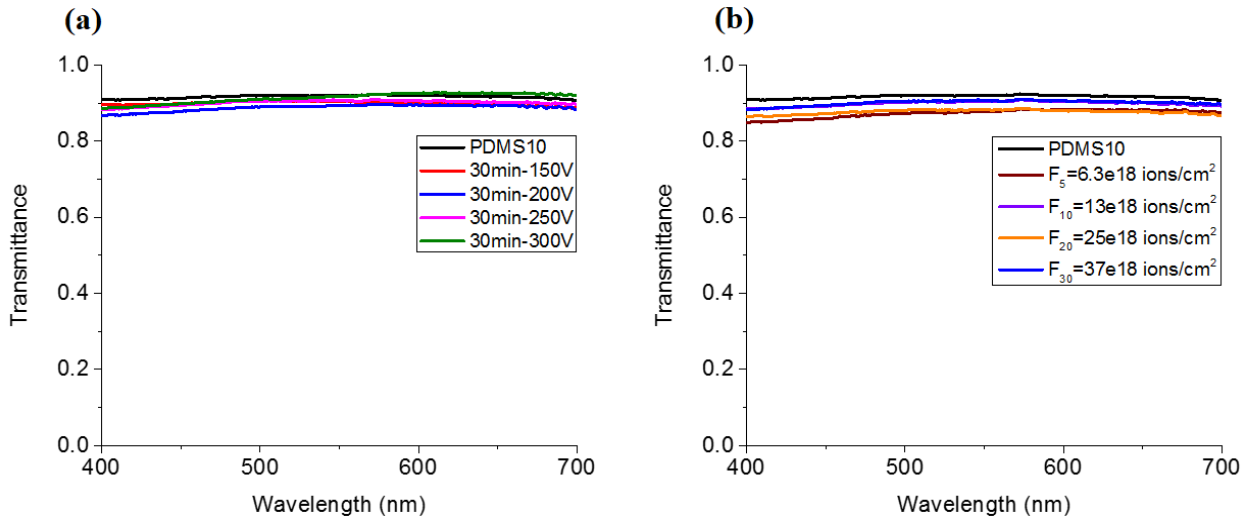

Figure 8-15: Transmittance spectrum of exposed to AIB PDMS, (a) at different grid voltages, and (b) at different fluences.

However it was decided to investigate the reflectance spectra of these materials. The results are presented in (Figure 8-16a-b) and show that the nominal reflectance of the samples is reduced. It can be assumed that these changes are due to the surface patterns which increase the diffuse reflection of the surface.

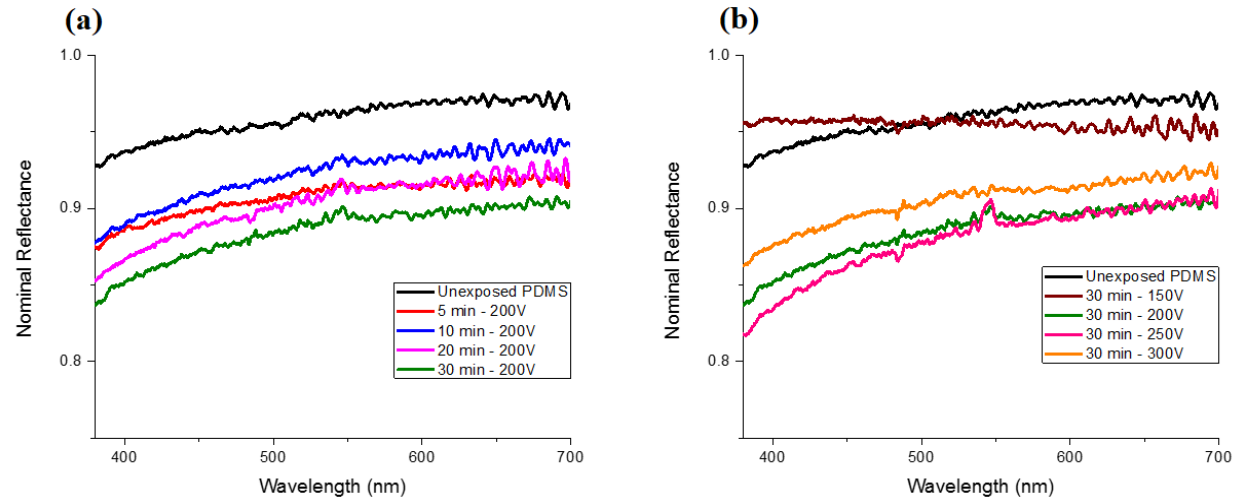

Figure 8-16: Reflectance spectrum of exposed to AIB PDMS, (a) at different grid voltages, and (b) at different fluences.

8.5 Chapter Summary

Etching rates of 0.1 – 1.5 nm/min have been achieved by exposing silicon and silicon dioxide surfaces to argon ion beam generated using an inductive coupled plasma source. The etching process revealed uniform material removal along the exposed area, while retaining atomic level smoothness. The exposure of PDMS surface to argon ion bombardment resulted to wrinkle generation. Therefore the physics of this behavior were studied together with some models that can predict the pattern parameters such as wavelength and amplitude. A detailed analysis of these patterns showed that the wavelengths' period is strongly depended on the applied grid voltage while the amplitude of the wrinkles showed a dependence on both ion fluence and grid voltage. The wetting characteristics of the wrinkled PDMS surfaces showed a significant reduction in CA which however was not stable. The optical transmittance of the specimens was retained while their reflectance was, in part, reduced owing to an increased optical diffusion led by the surface topography.

CHAPTER 9 CONCLUDING REMARKS

9.1 Summary of Results

Surface processing of silicon and silicon based materials (Silicon Dioxide and PDMS) through thermal oxidation and plasma processing has been studied in this thesis. The main results extracted from these two processing methods are separately listed below.

9.1.1 Part A: Silicon Thermal Oxidation

Thermal growth of silicon dioxide thin films was investigated with the main aim to understand the physics of thermal oxidation process and how the most important controlling parameters affect the grown material and its characteristics. In order to gain a good theoretical background the physics of thermal oxidation and the oxidation kinetics were studied in detail using the well-known Deal–Grove model. Seven set of samples were fabricated using PlanarTECH furnace system, at 1,100^{o}C and different oxidation times (0.5h, 1h, 2h, 3h, 4h, 6h and 8h). Detailed physical, topographical, geometrical and optical characterization of the fabricated samples showed the following results:

- Thin film thicknesses, as measured by WLRS and XRR techniques, varied from 50nm to 204nm and oxidation rates were approximately 40 nm/hour. Additionally, the values showed a very good correlation with the theoretical thickness values, calculated by the D-G model.
- The AFM analysis showed that, the topography underwent through porosity generation and roughness changes with respect to the oxidation time, however in all cases, atomic scale roughness was retained.
- The density of the oxide products as measured through the critical angle for total reflection in XRR measurements confirmed that the produced samples are actually amorphous silicon dioxide thin films, irrespective to the oxidation time used. Finally, different optical properties were observed on each set of samples. The physics behind this behavior attributed to thin film interference, and a color - thickness correlated map was generated in order to calculate roughly the thickness of the produced layer.

The knowledge and results gained from this work can be applied in areas of precise nanoscale material synthesis and characterization. Based on the reported results, one can use the

experimental processes to synthesize amorphous silicon dioxide layers with precise thickness and high quality for a wide variety of applications.

9.1.2 Part B: Plasma Processing of Silicon, Silicon Dioxide and PDMS

A non-reactive inductively coupled plasma (ICP) surface processing, specifically Argon Ion Bombardment (AIB), was studied in depth with the main purpose to understand how it affects hard and soft materials. Therefore commercially purchased silicon wafers, and thermally grown silicon dioxide thin films (synthesized in Part A of this thesis) were used as hard materials, while spin coated PDMS layers with base and curing agent ratio of 10:1 were used as soft polymeric films. The effect of grid voltage and exposure time on all samples were quantified through physical, topographic, geometric and optical characterizations. The results showed that:

- In the case of hard materials, uniform and high quality material ablation was achieved with etching rates of 0.1 to 1.5 nm/min.
- In contrast to Si and SiO_2 (hard materials) AIB of PDMS led to surface patterning instead of material etching. The initially smooth surface of PDMS was transformed into a wrinkled pattern with specific wavelengths and amplitudes. Detailed analysis of this behavior revealed that a stiff thin layer was generated on PDMS surface during AIB, which due to high stress and strain mismatch tends to buckle. It appears that the wavelengths' period is strongly depended to the applied grid voltage while the amplitude of the wrinkles showed a dependence on both ion fluence and grid voltage.
- The wetting characteristics of the plasma exposed PDMS surfaces showed a significant reduction in CA which was attributed to the removal of methyl groups from the exposed surface and increase of polar functionalities. However, the hydrophobic nature of PDMS was recovered after an aging time, due to the migration of polar groups to the bulk of the surface.
- The optical characterization of the PDMS surfaces revealed that although no significant changes were presented on the transmittance spectra, however optical reflectance spectroscopy showed a reduction in normal reflectance which is due to increase in diffusive reflectance that presented after surface patterning.

Very important knowledge in surface modification has been gained through the investigation of plasma processing. Hard materials such as Si and SiO_2 can be precisely etched for purposes

such as Si native oxide removal and surface micro or nano-scale modification through masking and etching processes. On the other hand, AIB of soft materials such as PDMS can lead to wrinkled geometries with several potential applications like biomedical sensors, anti-reflective surfaces and as means to calculate the Young's moduli of the deposited film.

9.2 Future Perspectives

Several ideas have been generated through the implementation of this project that will hopefully serve as the basis for future investigations. Some of those ideas have been tested and preliminary results are separately presented and discussed below

9.2.1 Thermal Processing Opportunities

Thermal processing using different gases and substrates

Due to the gained knowledge in the area of thermal processing and the equipment availability new cases can be investigated. PlanarTECH furnace has the ability to expose silicon wafers to the following gases; nitrogen, oxygen, methane and hydrogen. Therefore nitrogen can be used to synthesize silicon nitride material that can be investigated in similar fashion as the oxidation process. Moreover, the system can be used for thermal processing of different materials and structures. For instance titanium nanoparticles or thin films can be oxidized in order to create a photo catalytic titanium dioxide thin film. Finally the PlanarTECH system has the capability to operate as a thermal chemical vapor deposition (TCVD) system, therefore carbon nanotubes, amorphous carbon thin films and many more new materials can be deposited on a wide variety of substrates.

Preceramic polymers

Preceramic polymers, namely polymers that are converted into ceramics upon heat treatment, have been successfully used for almost 40 years to give advanced ceramics, especially belonging to the ternary (SiCO) and (SiCN) systems or to the quaternary SiBCN system, (Bernardo et al. 2014). One of their main advantages is the possibility of combining the shaping and synthesis of ceramics. Therefore a first approach of this research topic was done using a PDMS polymer in an orthogonal shape placed in PlanarTECH furnace under Argon gas, 1300^{o}C and 3 hours treatment. The preliminary result is shown in Figure 9-1, where it is obvious that PDMS has been transformed into a ceramic material with an incredible transformation in mechanical properties. The elastic modulus of PDMS as measured through

nanoindentation has increased by 4 orders of magnitude, from ~ 2MPa to ~81GPa. Therefore a detailed study of temperature, ambient gas and pressure, and new preceramic polymers can be applied in order to combine geometrical, mechanical and structural properties.

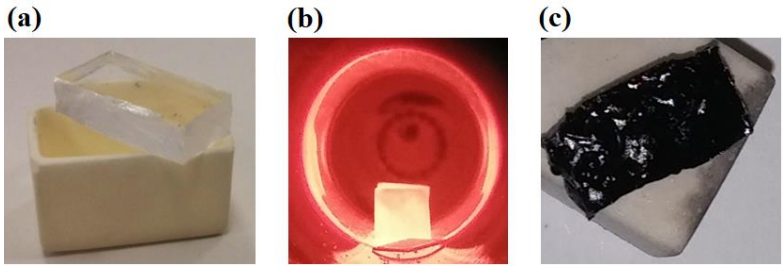

Figure 9-1: PDMS to Ceramic Transformation, (a) PDMS 10:1, (b) PDMS pyrolysis in PlanarTECH furnace under Argon atmosphere, (c) PDMS after pyrolysis, transformed to Ceramic material

9.2.2 Plasma Processing Opportunities

Hard materials plasma processing

AIB of silicon and silicon dioxide surfaces can lead to high quality material removal with rates that vary between 0.1-1.5 nm/min, depending on ion energy and fluence. Hence, this capability can lead to a series of applications and further investigations some of which are listed below:

- Further investigation of AIB parameters in order to achieve higher etching rates while maintaining the atomic surface quality.
- Masking of SiO_2 or Si surfaces, AIB etching and production of precise patterns at micro or nano scale for optical, superhydrophobic and MEMS applications.
- Precise removal of native oxide from Si wafers in order to achieve high quality and high adhesion layer for deposition purposes.

Further analysis of PDMS patterns

The generation of the patterns and their possible high technology applications was the most interesting part of this work. Therefore further investigation can increase the ability of tailoring such surfaces. Some of the parameters that were not studied in depth but can play a crucial role in pattern generation are: (a) the bias voltage which will further increase the ion kinetic energies, (b) the substrate temperature, (c) the usage of different gases, and (d) the mechanical properties of the exposed PDMS samples.

On the other hand as it was analyzed in Section 8.3.1, the patterns generated on PDMS surface depend on the thickness of the deposited/generated stiff layer and the ratio of Young's moduli between the film and the substrate. Two main studies can be investigated in order to understand the wrinkle properties: 1) change of Young's moduli ratio and 2) deposition of thicker layer upon the PDMS surface. The first case can be achieved by 2 ways, changing the substrate PDMS elastic modulus by the usage of different elastomer–curing agent ratios, or by depositing a material with different elastic modulus. A first approach of this case study was achieved using a plasma enhanced chemical vapor deposition (PECVD) technique in order to deposit hydrogenated amorphous carbon (a-C:H) film on top of a PDMS surface. Applying this process both of the above mentioned steps covered, since stiff material with different thicknesses was deposited on PDMS. Some of the preliminary morphological AFM and SEM data are shown in Figure 9-2 and Figure 9-3 respectively. The effect of different deposition time is combined with different thickness values of the stiff film. AFM images show that the surface is patterned and surface roughness increases while the deposition time–layer thickness increases.

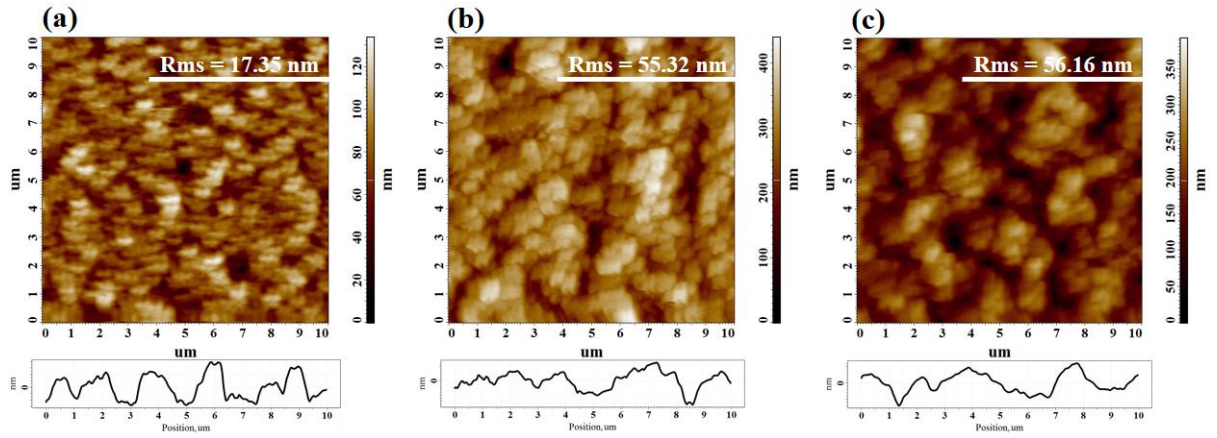

Figure 9-2: AFM images of HDLC deposited on PDMS$_{10}$ by CVD method for different deposition times, a) 10 min, b) 20 min and c) 30 min

The morphology of the patterns is more clearly presented in the SEM images presented in Figure 9-3. It is obvious that wrinkles have been generated which in contrast with the wrinkles reported and analyzed in this work, show a denser and overlapped version. Especially in the case of Figure 9-3b where the thicker layer of HDLC has been deposited, the patterns seem to be overlapped and generation of random structures occurs.

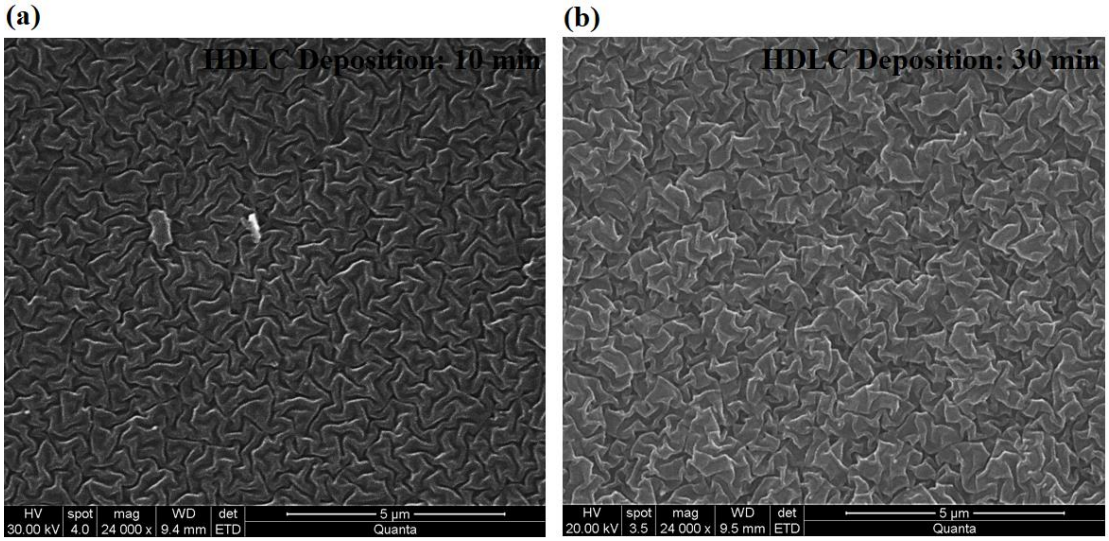

Figure 9-3: SEM images of HDLC deposited on $PDMS_{10}$ by CVD method, (a)-10 min deposition, and (b)-30 min deposition

A preliminary test of optical measurements shows that in general the optical transmittance reduces and this can be assumed due to the increase of diffusive reflectance and absorbance of the deposited layer.

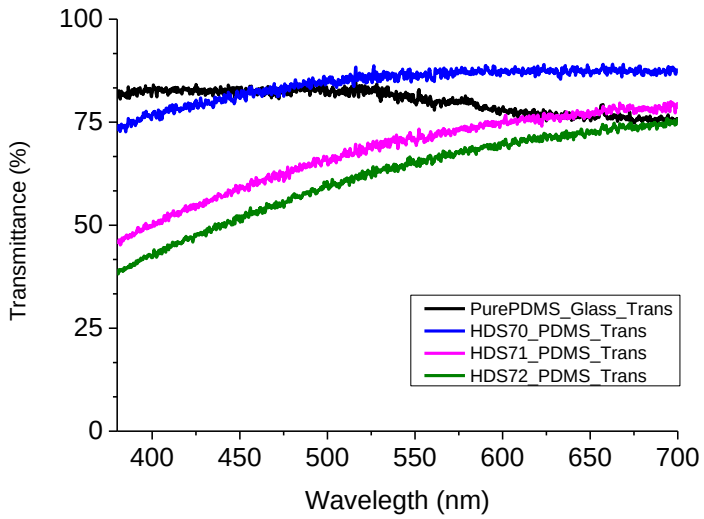

Figure 9-4: UV-VIS Transmittance spectra of HDLC deposited on $PDMS_{10}$ by CVD method at different deposition times, HDS70 = 10 min, HDS71 = 20 min and HDS72 = 30 min

Therefore further and deeper investigation can be applied using different a-C:H synthesis conditions and specific characterization techniques to understand how the patterns behave under the influence of a stiff layer.

9.3 Closing Statements

The surfaces of solids influence our everyday life and take the responsibility for how an object appears and how it could chemically or mechanically interact with other substances (solids, fluids, gases, plasmas). Therefore the properties and structures of surfaces and surface layers are of obvious importance in the general domain of materials science. New techniques have been developed within the past decade for modifying surface layers with an attempt of altering a wide range of characteristics of the surface such as: roughness, hydrophilicity or hydrophobicity, surface charge, surface energy, biocompatibility and reactivity. Nanoparticles deposition, thin film deposition by spin coating, chemical vapor deposition or physical vapor deposition, reactive and non-reactive plasma processing and thermal processing are among those techniques. Moreover due to the availability of precise characterization techniques such as optical spectroscopy, atomic force microscopy (AFM), scanning electron microscopy (SEM), x-ray reflectivity (XRR) and x-ray diffraction (XRD), nanoindentation, and profilometry the surface modification techniques can be optimized and functionalized with regards to the needed application: *surface tailoring*.

In this thesis, thermal oxidation and non-reactive plasma processing techniques were used together with AFM, XRR, CA, and UV-VIS spectroscopy characterization techniques. The results revealed that both techniques are very important in precise modification of both chemical and physical properties of the surfaces. In conclusion, it is important to mention that the knowledge gained through the elaboration of this project can be used for contribution into a further development of material science and technology.

REFERENCES

Accuratus.com, 2016. Fused Silica | SiO2 Material Properties. Available at: http://accuratus.com/fused.html [Accessed January 3, 2016].

Archive.cnx.org, 2016. Structures of Element and Compound Semiconductors. Available at: http://archive.cnx.org/contents/c119deb0-8108-4585-aa6a-e7ea6996e6bd@6/structures-of-element-and-compound-semiconductors [Accessed January 3, 2016].

Azom.com, 2015. Silica - Silicon Dioxide (SiO2). Available at: http://www.azom.com/article.aspx?ArticleID=1114 [Accessed December 8, 2015].

Bernardo, E. et al., 2014. Advanced ceramics from preceramic polymers modified at the nano-scale: A review. *Materials*, 7(3), pp.1927–1956.

Bigepfl.ch, 2016. BIG>Drop Analysis. Available at: http://bigwww.epfl.ch/demo/dropanalysis/ [Accessed January 17, 2016].

Bracco, G. & Holst, B., 2013. *Surface science techniques*,

Braga, a. F.B. et al., 2008. New processes for the production of solar-grade polycrystalline silicon: A review. *Solar Energy Materials and Solar Cells*, 92(4), pp.418–424. Available at: http://linkinghub.elsevier.com/retrieve/pii/S092702480700400X [Accessed September 24, 2015].

Bumems.ee.boun.edu.tr, 2016. BUMEMS. Available at: http://www.bumems.ee.boun.edu.tr/ [Accessed January 10, 2016].

Byun, I., Coleman, A.W. & Kim, B., 2013. Transfer of thin Au films to polydimethylsiloxane (PDMS) with reliable bonding using (3-mercaptopropyl)trimethoxysilane (MPTMS) as a molecular adhesive. *Journal of Micromechanics and Microengineering*, 23(8), p.85016. Available at: http://stacks.iop.org/0960-1317/23/i=8/a=085016.

Cadarso, V.J. et al., 2008. 3-D modulable PDMS-based microlens system. *Opt. Express*, 16(7), pp.4918–4929. Available at: http://www.opticsexpress.org/abstract.cfm?URI=oe-16-7-4918.

Campbell, S. a, 2008. *Engineering at the Micro- and Nanoscale Third Edition*,

Chemistry.beloit.edu, 2016. Welcome to the Chem Connections Homepage. Available at: http://chemistry.beloit.edu/ [Accessed January 10, 2016].

Chen, X. & Hutchinson, J.W., 2004. Herringbone Buckling Patterns of Compressed Thin Films on Compliant Substrates. *Journal of Applied Mechanics*, 71(5), p.597.

Cleanroom.byu.edu, 2015. Oxide/Nitride Color vs. Thickness Generator. Available at: http://www.cleanroom.byu.edu/color_chart.phtml [Accessed December 6, 2015].

Comfort, J.H., Garverick, L.M. & Reif, R., 1987. Silicon surface cleaning by low dose argon-ion bombardment for low-temperature (750 °C) epitaxial silicon deposition. I. Process considerations. *Journal of Applied Physics*, 62(8), p.3388. Available at: http://scitation.aip.org/content/aip/journal/jap/62/8/10.1063/1.339301.

Commons.wikimedia.org, 2016. File:Materials science tetrahedron;structure, processing, performance, and proprerties.svg - Wikimedia Commons. Available at: https://commons.wikimedia.org/wiki/File:Materials_science_tetrahedron;structure,_processing,_performance,_and_proprerties.svg [Accessed January 3, 2016].

Deal, B.E. & Grove, A.S., 1965. General Relationship for the Thermal Oxidation of Silicon. *Journal of Applied Physics*, 36(12), p.3770. Available at: http://scitation.aip.org/content/aip/journal/jap/36/12/10.1063/1.1713945.

Doctoral, T., 2014. Modified Au-based nanomaterials studied by surface plasmon resonance spectroscopy Estudio de nanomateriales modificados basados en Au mediante espectroscop ´ ıa de resonancia de plasmones de superficie ıda Serrano Rubio.

Donnelly, V.M. & Kornblit, A., 2013. Plasma etching : Yesterday , today , and tomorrow. , 77204(August), pp.1–48.

Dowcorning.com, 2016. Chemical Vapor Deposition Variants - Dow Corning. Available at: http://www.dowcorning.com/content/etronics/etronicschem/etronics_newcvd_tutorial3.asp [Accessed January 6, 2016].

Dropsnake, T., 2011. DropSnake and LB-ADSA user manual. , pp.1–8.

Dsftm.cnr.it, 2016. Dipartimento Scienze Fisiche e Tecnologie della Materia. Available at: http://www.dsftm.cnr.it/ [Accessed January 10, 2016].

Eliezer, S.E. and Y., 1989. *The Fourth State of Matter, An Introduction to Plasma Science*,

Esl.ecsdl.org, 2016. Electrochemical and Solid-State Letters. Available at: http://esl.ecsdl.org/ [Accessed January 10, 2016].

Filmetrics, I., 2015. Calculate Spectral Reflectance of Thin-Film Stacks. *Filmetrics.com*. Available at: http://www.filmetrics.com/reflectance-calculator [Accessed December 4, 2015].

Foggiato, J., 2012. Chemical Vapor Deposition of Silicon Dioxide Films. *Thin-Film Deposition Processes and Technologies*, pp.111–150.

Google.com.cy, 2016. silicon applications - Google Search. Available at: https://www.google.com.cy/search?q=silicon+applications&espv=2&biw=1366&bih=609&source=lnms&tbm=isch&sa=X&ved=0ahUKEwjB17WYoJXKAhWB0xQKHbjPDnMQ_AUIBigB [Accessed January 6, 2016].

Guldin, S., 2013. Inorganic Nanoarchitectures by Organic Self-Assembly. , 19, pp.19–33. Available at: http://link.springer.com/10.1007/978-3-319-00312-2 [Accessed December 3, 2015].

Haynes, W.M., 2014. CRC Handbook of Chemistry and Physics. , p.9 65–69.

Henrie, J. et al., 2004. Electronic color charts for dielectric films on silicon. , 12(7), pp.1464–1469.

HongKong, C.U. of, CHAPTER 4 : Oxidation.

Hopcroft, M. a., Nix, W.D. & Kenny, T.W., 2010. What is the Young's Modulus of Silicon? *Journal of Microelectromechanical Systems*, 19(2), pp.229–238. Available at: http://ieeexplore.ieee.org/lpdocs/epic03/wrapper.htm?arnumber=5430873.

Hu, Y.Z. et al., 1991. In situ spectroscopic ellipsometric investigation of argon ion bombardment of single-crystal silicon and silicon dioxide films ! I .',. , 60, pp.76–79.

Images.dailytech.com, 2016. DT Images. Available at: http://images.dailytech.com/ [Accessed January 10, 2016].

Jansen, H. et al., 1996. A survey on the reactive ion etching of silicon in microtechnology. *Journal of Micromechanics and Microengineering*, 6(1), p.14. Available at:

http://stacks.iop.org/0960-1317/6/i=1/a=002.

Jin, M. et al., 2005. Super-Hydrophobic PDMS Surface with Ultra-Low Adhesive Force. *Macromolecular Rapid Communications*, 26(22), pp.1805–1809. Available at: http://doi.wiley.com/10.1002/marc.200500458 [Accessed September 16, 2014].

Julia, B. et al., 2003. Synthesis and Characterization of Transparent PDMS - Metal-Oxo Based Organic - Inorganic Nanocomposites. *Chem. Mater.*, 15(20), pp.3026–3034.

Kilby, J.S., 1976. Invention of the integrated circuit. *Electron Devices, IEEE Transactions on*, 23(7), pp.648–654.

Koch, K., Bhushan, B. & Barthlott, W., 2008. Diversity of structure, morphology and wetting of plant surfaces. *Soft Matter*, 4(10), p.1943.

Kwon, S. et al., 2014. Nanostructured self-cleaning lyocell fabrics with asymmetric wettability and moisture absorbency (part I). *RSC Adv.*, 4(85), pp.45442–45448. Available at: http://dx.doi.org/10.1039/C4RA08039D.

Learner.org, 2016. Chemistry. Available at: https://www.learner.org/courses/chemistry/text/text.html?dis=U&num=Ym5WdElURS9OQ289&sec=YzJWaklUQS9NaW89 [Accessed January 3, 2016].

Lee, D. & Yang, S., 2012. Surface modification of PDMS by atmospheric-pressure plasma-enhanced chemical vapor deposition and analysis of long-lasting surface hydrophilicity. *Sensors and Actuators B: Chemical*, 162(1), pp.425–434. Available at: http://linkinghub.elsevier.com/retrieve/pii/S0925400511011075.

Love, B.J., 2003. Improvement in Adhesion for the Epoxy-SiC System via Plasma and Silane Surface Modification Techniques by in Materials Science and Engineering.

M. A. C. Aguila, I.B.C. and E.P.E., 2010. Sustained Hydrophilicity of Argon Plasma- Treated PDMS Surfaces. *28th SPP Physics Congress*, (October).

Malecha, K., Gancarz, I. & Tylus, W., 2010a. Argon plasma-assisted PDMS–LTCC bonding technique for microsystem applications. *Journal of Micromechanics and Microengineering*, 20(11), p.115006. Available at: http://stacks.iop.org/0960-1317/20/i=11/a=115006?key=crossref.24e2061028600efc7eafbee9f60969ff [Accessed December 16, 2015].

Malecha, K., Gancarz, I. & Tylus, W., 2010b. Argon plasma-assisted PDMS–LTCC bonding technique for microsystem applications. *Journal of Micromechanics and Microengineering*, 20, p.115006.

Mantisdeposition.de, 2016. Mantis Deposition Systems: Home. Available at: http://www.mantisdeposition.de/home.html [Accessed January 16, 2016].

McDonald, J.C. & Whitesides, G.M., 2002. Poly(dimethylsiloxane) as a material for fabricating microfluidic devices. *Accounts of Chemical Research*, 35(July), pp.491–499.

Microchemicals.com, 2016. Silicon, Quartz, Glass and Fused Silica Wafer. Available at: http://www.microchemicals.com/products/wafers/our_wafer_stock_list.html [Accessed January 14, 2016].

Mit.edu, 2015. Amorphous Silicon. Available at: http://www.mit.edu/~6.777/matprops/asi.htm [Accessed December 8, 2015].

Mit.edu, 2016. PDMS. Available at: http://www.mit.edu/~6.777/matprops/pdms.htm [Accessed January 9, 2016].

Moon, M.-W. et al., 2007. Wrinkled hard skins on polymers created by focused ion beam. *Proceedings of the National Academy of Sciences of the United States of America*, 104(4), pp.1130–3. Available at: http://www.pubmedcentral.nih.gov/articlerender.fcgi?artid=1770894&tool=pmcentrez&rendertype=abstract.

Nagashima, S. et al., 2012. Controlled formation of wrinkled diamond-like carbon (DLC) film on grooved poly(dimethylsiloxane) substrate. *Diamond and Related Materials*, 22, pp.48–51. Available at: http://linkinghub.elsevier.com/retrieve/pii/S0925963511003797 [Accessed February 1, 2015].

Nessim, G.D., 2010. Properties, synthesis, and growth mechanisms of carbon nanotubes with special focus on thermal chemical vapor deposition. *Nanoscale*, 2(8), p.1306.

Nikolaou, P. et al., 2015. Functionally graded poly(dimethylsiloxane)/silver nanocomposites with tailored broadband optical absorption. *Thin Solid Films*, 581, pp.14–19. Available at: http://www.sciencedirect.com/science/article/pii/S0040609014012188 [Accessed January 9, 2016].

Nikon.com, 2016. No Title. Available at: http://www.nikon.com/products/precision/technology/ic/img/pic_story02_01.jpg [Accessed January 3, 2016].

Oxford-instruments.com, 2016. SEM Competition Winner - Oxford Instruments. Available at: http://www.oxford-instruments.com/businesses/nanotechnology/plasma-technology/campaigns/sem-competition-winner [Accessed January 13, 2016].

Park, H.-G. et al., 2015. Control of the wrinkle structure on surface-reformed poly(dimethylsiloxane) via ion-beam bombardment. *Scientific Reports*, 5(January), p.12356. Available at: http://www.nature.com/doifinder/10.1038/srep12356.

Physicscentral.com, 2015. No Title. Available at: http://www.physicscentral.com/explore/action/color-tunable-fibers.cfm [Accessed December 3, 2015].

Powerguru.org, 2016. No Title. Available at: http://www.powerguru.org/wordpress/wp-content/uploads/2012/11/Thermal-Oxidation.jpg [Accessed January 4, 2016].

Probe, K., Overview, E. & Guide, P., 2015. E t c h O v e r v i e w f o r M i c r o s y s t e m s. , (3).

Pro-fusiononline.com, 2016. Elderfield & Hall / Pro-Fusion. Available at: http://www.pro-fusiononline.com/ [Accessed January 10, 2016].

Rack, P.D., 2015. Etching, Wet State, The Plasma Principles, Plasma Etching Systems, Advanced Plasma Ratio. *University of Tennessee*, pp.1–34.

Ray, S.K. et al., 1996. TEOS-based PECVD of Silicon Dioxide for VLSl Applications. , 6(September 1995), pp.73–82.

Saga, T., 2010. Advances in crystalline silicon solar cell technology for industrial mass production. *NPG Asia Materials*, 2(3), pp.96–102. Available at: http://www.nature.com/doifinder/10.1038/asiamat.2010.82 [Accessed January 15, 2015].

Sakhuja, M., 2014. Nanostructured Glass Covers for Photovoltaic Applications for the Degree of Doctor of Philosophy Department of Electrical and Computer Engineering.

Schneider, F. et al., 2009. Process and material properties of polydimethylsiloxane (PDMS) for Optical MEMS. *Sensors and Actuators A: Physical*, 151(2), pp.95–99. Available at:

http://linkinghub.elsevier.com/retrieve/pii/S0924424709000466.

Shirtcliffe, N.J., McHale, G. & Newton, M.I., 2011. The superhydrophobicity of polymer surfaces: Recent developments. *Journal of Polymer Science, Part B: Polymer Physics*, 49(17), pp.1203–1217.

Silicon, I., 2000. Simulation of High-Pressure Oxidation of Silicon Based on the Interfacial Silicon Emission Model. , 39(10), pp.952–954.

Sio, T. & Sio, C., Thermal Oxidation of Si Thermal SiO 2 Properties. Available at: https://www.eng.tau.ac.il/~yosish/courses/vlsi1/I-4-1-Oxidation.pdf.

Slack, G.A. et al., 1961. Thermal Conductivity of Silicon and Germanium from 3degK to the Melting Point. , 1431.

Streetman, B.G.. . S.B., 2000. *Solid State Electronic Devices* 5th ed., New Jersey: Prentice Hall.

Tf.uni-kiel.de, 2016. 6.2.1 Si Oxide. Available at: http://www.tf.uni-kiel.de/matwis/amat/elmat_en/kap_6/backbone/r6_2_1.html [Accessed January 3, 2016].

Thaimedicalnews.com, 2016. Thailand Medical Tourism Health and Fitness Travel Tour Blog. Available at: http://www.thaimedicalnews.com/ [Accessed January 10, 2016].

Thetametrisis.com, 2015. FR-Monitor. Available at: http://www.thetametrisis.com/fr-monitor [Accessed November 14, 2015].

Todorov, S. & Fossum, E., 1988. Sputtering of silicon dioxide near threshold. *Applied physics letters*, 10027(July 1987), pp.365–367. Available at: http://ieeexplore.ieee.org/xpls/abs_all.jsp?arnumber=4857304.

Toyo-seikan.co.jp, 2016. Functional Bottles : Barrier Bottles | PET Bottle | Technical Information | TOYO SEIKAN. Available at: https://www.toyo-seikan.co.jp/e/technique/petbottle/barrierbottle/ [Accessed January 6, 2016].

Vella, E. et al., 2011. Unraveling exciton dynamics in amorphous silicon dioxide: Interpretation of the optical features from 8 to 11 eV. *Physical Review B*, 83(17), p.174201. Available at: http://link.aps.org/doi/10.1103/PhysRevB.83.174201 [Accessed January 3, 2016].

Wikipedia, 2016a. Czochralski process. Available at: https://en.wikipedia.org/wiki/Czochralski_process [Accessed January 3, 2016].

Wikipedia, 2016b. Silicon. Available at: https://en.wikipedia.org/wiki/Silicon [Accessed January 3, 2016].

Wu, D. et al., 2014. Controlling the surface buckling wrinkles by patterning the material system of hard-nano-film/soft-matter-substrate. *Science China-Physics Mechanics & Astronomy*, 57(4), pp.637–643. Available at: <Go to ISI>://000332978500008.

www.creativeedge.co.uk, C., 2016. Polysilicon Production - Blog - The Quartz Corp | High Purity Quartz. *Thequartzcorp.com*. Available at: http://www.thequartzcorp.com/en/blog/2014/04/28/polysilicon-production/61 [Accessed January 3, 2016].

Xakalashe, B.S. & Tangstad, M., 2011. Silicon processing : from quartz to crystalline silicon solar cells. , (March), pp.6–9.

Yao, L. & He, J., 2014. Recent progress in antireflection and self-cleaning technology - From surface engineering to functional surfaces. *Progress in Materials Science*, 61, pp.94–143. Available at: http://dx.doi.org/10.1016/j.pmatsci.2013.12.003.

Yasaka, M., 2010. V . , 26(2), pp.1–9.

Yoon, T.O. et al., 2008. Formation of superhydrophobic poly(dimethysiloxane) by ultrafast laser-induced surface modification. *Optics express*, 16(17), pp.12715–12725.

APPENDIX A: TCVD Technical Characteristics

The Thermal Chemical Vapor Deposition (TCVD) system specifications are presented in Table below.

Table 1: Specifications of Thermal Chemical Vapor Deposition system, in RUNMS synthesis lab

Tube	• 120 cm long • diameter 2´ (50mm) • water cooled end flanges • Material: quartz, max temp 1,200 ^{o}C
SiC heater w/ Glass Wool Molding	• Max temp 1,450 ^{o}C • Max operating temp 1,400 ^{o}C
3 zones furnace	• 120x300x120mm
Available gas lines	• Acetylene (C_2H_2) • Hydrogen (H_2) • Ammonia (NH_3) • Methane (CH_4) • Argon (Ar) • Spare 1 • Spare 2
Installed and available gases	• Oxygen (O_2) • Hydrogen (H_2) • Nitrogen (N_2) • Methane (CH_4) • Argon (Ar)
Vacuum & Pressure Control	• 1 Dry Pump (300 liter/min) • Basic Pressure <0.2 Pa (2.0E-3mbar) • 1 Convection Gauge and 1 capacitance manometer • Motor-Geared Throttle Valve for working pressure adjustments

APPENDIX B: Reflectance Dependence on Surface Roughness

Another important parameter that must be studied in order to understand how the light interacts with thin films, is surface roughness. The surface roughness increases the light scattering causing uniform reduction of its reflectivity as it shown in Figure 0-1 below.

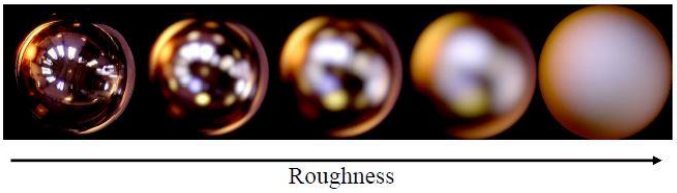

Figure 0-1: Changes in optical reflectance with the increase of light scattering by the means of surface roughness increase

As it was mentioned before, the effect of scattering was ignored during the recording of reflectance spectrum. In this section the effect of the light scattering is investigated, in order to prove that the non-inclusion of light scattering causes negligible changes to the reflectivity.

In 1991 Bennett & Porteus proposed an equation that calculates the total scattering of a rough surface. This equation takes into account the theoretical reflectance of the surface, the wavelength of the incident light, its incident angle, and the root mean square roughness of the surface:

$$\mathrm{TIS}\left(\mathrm{R_q}\right) = \mathrm{R_o}\left[1 - \mathrm{e}^{-\left(\frac{4\pi \mathrm{R_q} \cos\theta_i}{\lambda}\right)}\right] \qquad \text{(B-1)}$$

where TIS refers to the Total Integrated Scatter [%], R_q to the root mean square roughness [nm], R_o to the theoretical reflectance of the surface [%], θ_i to the incident light angle [degrees], and λ to the incident light wavelength [nm]. Using experimental rms roughness data, provided by AFM analysis of each sample, light incident angle equal to 0^o, incident light wavelength equal to 500nm and ideal theoretical reflectance, the maximum scattering of each sample is calculated using the Eq. (B-1). The results are shown in Table 1 and are plotted with respect to the surface roughness in Figure 2.

Table 1: Parameters for calculation of Total Integrated Scattering

Reflectance, Ro [%]	Experimental Roughness, rms [nm]	Incident angle, θi	Incident light, λ [nm]	Scattering, TIS [%]

		[o]		
100	0.201	0	500	0.0026
100	0.311	0	500	0.0061
100	0.489	0	500	0.0151
100	0.571	0	500	0.0206
100	0.861	0	500	0.0468
100	0.999	0	500	0.0630
100	2.318	0	500	0.3388

The results show a maximum scattering of 0.34% which confirms the assumption of negligible scattering effect.

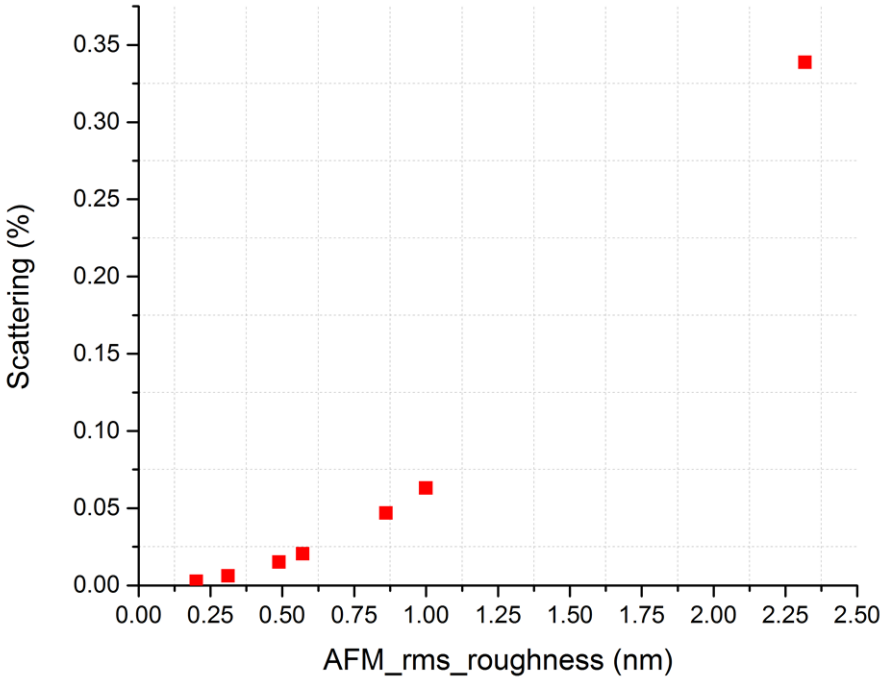

Figure 2: Scattering increase of the fabricated silicon dioxide samples

APPENDIX C: Publications and Dissemination

The results of this thesis have culminated in a series of conference and journal contributions that have been/will be submitted for review and subsequent presentation/publication. These are listed below.

Conference Participation

- S. Pozov, P. Nikolaou, M. Constantinou, G. Constantinides, 'Surface pattering of PDMS through argon ion bombardment and/or amorphous carbon deposition', E-MRS, Lille, France, 2-6 May 2016. (poster presentation, accepted)
- S. Pozov, G. Constantinides, 'Buckling-Induced Pattering of PDMS Surfaces Through Argon Ion Bombardment', 13th International Conference on Nanosciences & Nanotechnologies (NN16), 5-8 July 2016, Thessaloniki, Greece (oral presentation, accepted)

Journal Publication

- S. Pozov, P. Nikolaou, M. Constantinou, G. Constantinides, 'Wrinkling of PDMS Surfaces Through Argon Ion Bombardment: Effect of Ion Energy and Fluence', in preparation